

Podoba Yuriy

**Radio frequency heating on the WEGA  
stellarator**

**IPP 13/12  
Oktober 2008**

# **Radio frequency heating on the WEGA stellarator**

Inauguraldissertation

zur

Erlangung des akademischen Grades

doctor rerum naturalium (Dr. rer. nat.)

an der Mathematisch-Naturwissenschaftlichen Fakultät

der

Ernst-Moritz-Arndt-Universität Greifswald

vorgelegt von

Podoba Yuriy

geboren am 18.08.1979

in Kharkov, Ukraine

Greifswald 24.01.2006



Dekan:

1. Gutachter :

2. Gutachter:

Tag der Promotion:



# **CONTENTS**

<b>1.</b>	<b>INTRODUCTION .....</b>	<b>2</b>
1.1.	History & Motivation.....	2
1.2.	Overview .....	7
<b>2.</b>	<b>WEGA STELLARATOR.....</b>	<b>8</b>
2.1.	Magnetic configuration.....	8
2.2.	WEGA layout and diagnostics .....	9
2.2.1.	Interferometer .....	10
2.2.2.	Fast reciprocating Langmuir probe.....	11
2.2.3.	Bolometer .....	12
2.3.	Plasma heating system.....	13
2.3.2.	Transmission line .....	14
2.3.3.	Heating improvement by mode conversion .....	16
2.4.	Magnetic field variation experiments.....	17
<b>3.</b>	<b>OXB THEORY ON ECR HEATING .....</b>	<b>18</b>
3.1.	Ordinary and Extraordinary modes .....	18
3.2.	Electron Bernstein Wave.....	20
3.3.	Two-step conversion .....	23
3.4.	O-SX conversion.....	25
3.5.	SX-B conversion .....	29
3.5.1.	Direct SX to B conversion.....	29
3.5.2.	SX to FX tunneling effect on conversion efficiency .....	30
3.6.	Summary of theory .....	32
<b>4.</b>	<b>NUMERICAL SIMULATIONS OF THE OXB PROCESS.....</b>	<b>34</b>
4.1.	OXB in the ray tracing approximation .....	34
4.2.	OXB in full wave calculations .....	35
4.2.1.	Full wave code.....	35
4.2.2.	O-SX conversion efficiency .....	38
4.2.3.	Bernstein mode in 1D.....	39
4.2.4.	Vacuum calculations .....	41
4.2.5.	Perpendicular X-mode launch .....	41
4.2.6.	Polarization of the source in full wave calculations .....	42
4.3.	Conclusion from the preliminary full-wave calculations.....	45
<b>5.</b>	<b>ECR HEATING ANTENNA SHAPE OPTIMIZATION .....</b>	<b>46</b>
5.1.	Heating antenna development.....	46
5.1.1.	Heating antenna arrangement .....	46
5.1.2.	Antenna design .....	47
5.1.3.	Antenna emission pattern calculation.....	50

5.1.4. Antenna emission pattern measurements .....	53
<b>5.2. Plasma parameters and heating efficiency evolution .....</b>	<b>54</b>
5.2.1. Fast Langmuir probes .....	55
5.2.2. Bolometric measurements .....	56
5.2.3. Numerical efficiency calculation .....	59
<b>5.3. Conclusion from antenna optimization .....</b>	<b>Error! Bookmark not defined.</b>
<b>6. MEASUREMENTS OF WAVE ACTIVITY IN PLASMA .....</b>	<b>62</b>
<b>6.1. HF probes development .....</b>	<b>62</b>
6.1.1. Probes requirements.....	62
6.1.2. Probe testing arrangement .....	63
6.1.3. Comparison of the different probe types .....	64
<b>6.2. WEGA measurement arrangement .....</b>	<b>68</b>
6.2.1. Probes set in the WEGA .....	68
6.2.2. HF probes signals .....	71
6.2.3. Langmuir probes measurement.....	72
6.2.4. Data acquisition system .....	74
<b>6.3. Phase difference calculation .....</b>	<b>75</b>
<b>6.4. Summary of the measurement system.....</b>	<b>77</b>
<b>7. MEASUREMENTS AND CALCULATIONS RESULTS.....</b>	<b>78</b>
<b>7.1. Measured data .....</b>	<b>78</b>
7.1.1. Measured density .....	78
7.1.2. Measured amplitude and phase of HF .....	81
<b>7.2. Calculation and measurement comparison.....</b>	<b>87</b>
7.2.1. Full wave calculation results.....	87
7.2.2. Comparison of calculations and measurements .....	91
<b>7.3. Conclusions from the measurements .....</b>	<b>94</b>
<b>8. CONCLUSIONS.....</b>	<b>96</b>
<b>8.1. Calculations .....</b>	<b>96</b>
<b>8.2. Antenna design .....</b>	<b>96</b>
<b>8.3. HF measurement system.....</b>	<b>97</b>
<b>8.4. OXB existence.....</b>	<b>98</b>
<b>9. APPENDIX .....</b>	<b>100</b>
Appendix A DC brake .....	100
Appendix B Vacuum window.....	101
Appendix B1 AlN Permittivity measurement .....	102
Appendix C Code description .....	103
Appendix D HFSS code .....	108

# Abbreviations

HF	– High Frequency
EM	– Electromagnetic
ES	– Electrostatic
ECR(H)	– Electron Cyclotron Resonance (Heating)
LCFS	– Last Closed Flux Surface
O-mode	– Ordinary mode,
X-mode	– eXtraordinary-mode
SX-mode	– Slow X-mode
FX-mode	– Fast X-mode
(E)B-mode	– (Electrostatic) Bernstein mode
EB(W)	– Electron Bernstein (Wave)
OXB	– O-mode to SX-mode to B-mode conversion
BXO	– B-mode to SX-mode to O-mode conversion
O-SX	– O-mode to SX-mode conversion
SX-B	– SX to B-mode conversion
UHR	– Upper-Hybrid Resonance
WKB	– Wentzel-Kramer-Brillouin
$\vec{r}$	– radius vector
$r$	– coordinate along minor radius of torus
$R$	– coordinate along major radius of torus
$R_0$	– major radius of torus
$r_0$	– minor radius of torus
$r_{eff}$	– effective radius of magnetic surface
$t$	– time
$\iota$	– rotational transform
$k_b$	– Boltzmann constant
$m_e$	– electron mass
$\lambda$	– wavelength in vacuum
$f$	– frequency
$\omega$	– angular frequency
$\vec{k}$	– wave vector of the wave
$v_{ph}$	– phase velocity of the wave $v_{ph} = \omega/k$
$v_{gr}$	– group velocity of the wave $v_{gr} = d\omega/dk$
$f_p$	– plasma frequency
$f_{ce}$	– electron gyro-rotation frequency
$\omega_p$	– plasma angular frequency
$\omega_{ce}$	– electron gyro-rotation angular frequency
$\rho$	– Larmor radius of electron
$\rho_i$	– Larmor radius of ion
$\rho_q$	– charge density
$E$	– electric field strength



$B_0$	– external magnetic field strength at an magnetic axis of the plasma
$\vec{B}_0$	– external magnetic field vector
$\vec{E}$	– electric field vector
$X$	– dimensionless density $\omega_p^2/\omega^2$
$Y$	– dimensionless magnetic field $\omega_c/\omega$
$\Theta, \Phi$	– spherical coordinates
$\theta$	– angle between the $\vec{k}$ and $\vec{B}_0$ .
$\theta_{ins}$	– angle between the $\vec{k}$ and $\vec{B}_0$ at the HF source point.
$\theta_0$	– angle between the $\vec{k}$ and perpendicular to $\vec{B}_0$ at the HF source point. $90^\circ - \theta_{ins}$
$\theta_{opt}$	– $\theta_{ins}$ optimal for O-SX conversion
$\theta_B$	– Brillouin angle
$L_B$	– Brillouin length
$T_e$	– electron temperature [eV]
$n_e$	– electron density [ $\text{m}^{-3}$ ]
$\varphi_i$	– phase shift measured by interferometer
$n_{ei}$	– line-integrated density
$p_e$	– electron pressure $T_e n_e$
$n_{cutoff}$	– O-mode cutoff plasma density value
$n_{L-cutoff}$	– SX-mode cutoff plasma density value
$n_{R-cutoff}$	– FX-mode cutoff plasma density value
$n_{UHR}$	– density value on UHR layer
$L_n$	– characteristic density scale t length $L_n = \left  \frac{n_e}{\nabla n_e} \right $
$v_{Te}$	– electron thermal velocity $2\sqrt{\frac{K_B T_e}{m_e}}$



# **1. Introduction**

## ***1.1. History & Motivation***

The fusion plasma in toroidal confinement devices needs external heating in order to reach the Lawson criterion for fusion reaction. Many various methods of heating may be used, for example, ohmic heating in case of tokamaks, neutral beam injection, ion- or electron cyclotron heating. This work is focused on Electron Cyclotron Resonance Heating (ECRH). In this method, the magnetized plasma is heated by microwaves, whose frequency is equal (or close) to the cyclotron frequency of electrons rotating in external magnetic field. Numerous experiments were performed with ECRH heating in toroidal devices. The obtained plasma parameters vary for different installations, but one common limit has been observed: the density of the obtained plasma is limited by the cutoff values. As the heating wave must reach the resonant region where the electron cyclotron frequency is equal to the heating wave frequency, the density along the trajectory of the wave must not exceed the cutoff density value. Cutoff density is different for different modes propagating in the plasma<sup>1</sup>. However, there is a mode, which has no upper density limit. It is electrostatic<sup>2</sup> Electron Bernstein wave (EBW, EB-mode, B-mode). The EBW has no cutoff limit but its nature does not allow propagation outside of the plasma. To obtain this mode inside of the plasma the conversion from other externally launched modes is needed.

For ECR heating in toroidal devices Ordinary-mode<sup>3</sup> (O-mode) or Extraordinary-mode<sup>4</sup> (X-mode) is externally launched to the plasma from high or low field side<sup>5</sup> of the torus. Both modes have a cutoff limit for propagation. However, Slow Extraordinary

---

<sup>1</sup> It will be described in sections 3.1-3.2

<sup>2</sup> E field is directed parallel to  $k$  vector

<sup>3</sup> The E-field of this mode is directed parallel to the external magnetic field (for details see 3.1).

<sup>4</sup> The E-field component in the perpendicular direction to the external magnetic field (for details see 3.1)

<sup>5</sup> Here high field side and low field side denote the magnetic field strength at the inner side and outer side of the torus respectively. Thus low field side usually means outer side of torus, and high field side the inner one.

---

mode (SX-mode) may be converted to EB-mode if it reaches the Upper Hybrid Resonance (UHR) layer. O-mode launched from low field side may be coupled to the SX-mode in the region of the O-mode cutoff layer, and then the SX-mode is coupled to the B-mode. This process called OXB mode conversion, and was described in 1973 by Preinhaelter & Kopecký [19]. In their fundamental work, it was shown that the OXB mode conversion might be optimized in terms of O-mode insertion angle with respect to the external magnetic field direction. This optimization leads to interconnection of O- and SX-cutoff layers. Under these conditions, O-mode is completely converted into SX-mode, which then completely converts to EB-mode in the UHR layer. The OXB conversion processes are reversible. The inversed process is termed as BXO conversion.

For the first time, OXB conversion was shown experimentally in 1987 in Japan Institute of Plasma Physics Nagoya University on the TPL device [35,36]. In this experiment, a pulsed microwave source was used to investigate electron heating by OXB conversion at 9.3 GHz. The heating wave was launched obliquely via a horn antenna. The conversion existence was proved by two-dimensional high frequency (HF) probes measurements.

The OXB plasma heating and current drive with EBW in an overdense<sup>6</sup> plasma was demonstrated in W7-AS [14,32]. Additionally, in the PhD work of F.Volpe [20,21] the reversed BXO conversion process is used to access the centre of overdense plasma by the cyclotron emission diagnostic. In these works, vacuum wavelength of heating (or emitted) waves was in the range 2.1-4.3 mm that is much smaller than the typical plasma dimensions and density scale length  $L_n$ .

$$L_n = \left| \frac{n_e}{\nabla n_e} \right| \quad (1)$$

Under these conditions, Wentzel-Kramer-Brillouin (WKB) approximation was used and ray-tracing calculations were performed for simulation of wave propagation during the OXB (or BXO) mode conversion process.

Another possibility of producing an EB mode inside the plasma is the launching of an SX-mode from high field side of the torus. In this case, the SX-mode may reach the UHR layer directly if it does not encounter the L-cutoff<sup>7</sup> barrier. This scheme is called SX-B conversion. It is under investigation in Spain on TJ-II [37]; in this case the

---

<sup>6</sup> Plasma with the density exceeding the cutoff density for the given wave frequency (see 3.1).

<sup>7</sup> L-cutoff is the cutoff for the SX-mode (see 3.1).

---

---

wavelength is 5.6 mm and 10 mm. Ray tracing calculations are also applicable under these conditions.

Additionally, FX-mode, launched from low field side, may tunnel from the FX<sup>8</sup> into SX-mode through evanescent region, which is bordered by R-cutoff and UHR. SX-mode, reflected from L-cutoff, reached the UHR layer where it is converted to EBW. This process is called FX-SX-B mode conversion. To obtain desirable SX-FX tunneling efficiency the density steepness in the region of the R-cutoff and the UHR layer should be high enough to minimize the region size inaccessible for X-mode.

Recently the experiments with the FX-SX-B heating scenario were performed in Japan in Compact Helical System [6]. Here, the overdense plasma is obtained using the ECR heating on 2.45 GHz frequency. The OXB heating at 2.45 GHz frequency is currently under investigation in this device.

The experiments with SX-FX, (which is reverse of FX-SX) tunneling were performed in Princeton Plasma Physics Laboratory in CDX-U and NSTX spherical torus experiments [2,3]. In these experiments, emission of FX-mode is detected outside of the plasma on 8-18 GHz in CDX-U and 4-12 GHz in NSTX. In this experiment, the B-mode converts to the SX-mode at the UHR layer. The SX-mode tunnels through the inaccessible region to the FX wave. The desired density steepness in CDX-U was obtained using the limiter near receiving antenna. This allows a tunneling efficiency of SX to FX mode close to 100%. In NSTX the natural steepening of the edge density gradient was sufficient. However, the experiments with adjustable local limiter were also performed and good agreement with theory was found.

Additionally the optimization of the polarization of externally launched waves for optimal mode conversion to EB wave was performed in [43]. It is shown that the mode conversion efficiency may be optimized also by means of polarization adjustment of obliquely launched heating waves.

Summarising, experiments on Bernstein waves were performed in many plasma devices, including those are not listed here<sup>9</sup>, and many investigations concerned with EB waves were performed<sup>10</sup>. EBW waves are very promising for plasma heating and current drive as well as for the emission diagnostic, because of their property to penetrate overdense plasmas.

---

<sup>8</sup> FX- is the X-mode outside the R-cutoff layer SX is the X-mode beyond the UHR layer (see 3.1).

<sup>9</sup> For example Heliotron-J [33,34] and TPL [36].

<sup>10</sup> The work of F.Leuterer, where the HF probes was used to investigate EBW in a linear plasma [7].

---

The experiments may be nominally divided on two groups. The “high” frequency where the ray tracing calculations are applicable and “low” frequency where the wavelength is comparable with the characteristic density scale length, or even the plasma size. In this case, ray tracing is not applicable and simulations can only be performed using the full wave calculations.

The long wavelength OXB heating in toroidal devices was not much investigated up to recent time. More attention was paid to the high frequency experiments using the gyrotrons in millimeter wavelength range.

In this work the long wavelength ECR heating via OXB mode conversion is investigated in the WEGA stellarator.

The WEGA (Wendelstein Experiment in Greifswald für die Ausbildung) stellarator originally built in Grenoble (France). It operates since 2001 in IPP Greifswald. Its main goal is basic plasma research, educational training, and testing of new diagnostics for Wendelstein-7X.

WEGA is a classical mid-size stellarator with a toroidal vacuum chamber. It has major radius of plasma  $R \approx 0.73$  m and minor radius  $a_0 \approx 3.5$ - $12.5$  cm. The plasma in the WEGA stellarator is generated and heated by ECRH. The microwave is emitted from the low field side in the equatorial plane of the torus. The applied power is up to 26 kW (two power supplies of 20 and 6 kW) with a frequency of 2.45 GHz (vacuum wavelength  $\lambda = 12.245$  cm). Thus, the vacuum wavelength of the heating wave is comparable with the plasma size.

The overdense plasma with cutoffs located outside of the last closed flux surface (LCFS), makes direct ECRH in the WEGA stellarator inefficient in both the O-mode and X-mode regimes. This was confirmed in the first experimental campaign by perpendicular launch of the microwave with a  $TE_{11}$   $90^\circ$  cut waveguide used as an antenna [1]. Using this heating scenario, hollow profiles of  $n_e$  and  $T_e$  are observed in all discharges. The maximal values of  $n_e$  and  $T_e$  were located outside of the LCFS region.

Low heating efficiency can be explained assuming that most of the injected wave power was absorbed during multiple reflections between the cutoff layer and the metallic vessel wall. The heating wave was absorbed non resonantly in the plasma edge region. Only a small fraction of the power, which has the proper direction of  $\vec{k}$ , reached the region inside of LCFS after a two-step OXB mode conversion process.

The OXB conversion process requires an oblique launch of the O-mode into the overdense plasma with an optimal angle of  $\vec{k}$  to the external magnetic field. According to ray tracing calculations this angle is  $\approx 45^\circ$  for the  $1^{st}$  harmonic and  $\approx 36^\circ$  for the  $2^{nd}$

harmonic resonance. To obtain the optimum direction of the HF power launch the emitting antenna should be tilted for the optimum angle. Unfortunately, in the WEGA stellarator, it is impossible due to technical reasons, and antenna optimisation should be performed within the limits of technical restrictions. Chronologically this was the first step in our investigations.

As was mentioned in the WEGA stellarator, the wavelength is comparable not only with the  $L_n$  but even with the whole plasma minor radius. Therefore, WKB approximation is not applicable, and the full-wave calculations were applied to simulate the wave behaviour in the plasma. The code for full wave calculations was made by Dr. E. Holzhauser (University Stuttgart). This code solves the Maxwell's equations in the horizontal slab near the HF source. Calculations provide detailed information about waves behaviour near the resonance and cutoff layers in the magnetised plasma. The full wave calculations show the possibility of the mode conversion also in the WEGA plasma.

Additionally, the code gives the information about the efficiency of mode conversion for different insertion angles, density gradient scale lengths, frequencies the latter may be used for optimizing the heating using the 28 GHz gyrotron, which is in process of installation.

To bring the calculations closer to the heating of the WEGA plasma and to compare the calculations with the real situation in the plasma the electron density and HF wave activity should be investigated in the conversion region. This necessitates measurements with Langmuir and HF probes near heating antenna.

The performed HF measurements are focused on the measurement of the wave amplitude, as it was done on TPL [35], but also concerned with the phase behaviour of the waves in the plasma. In addition, the plasma density profiles in the region of mode conversion were measured at the same position where HF probes are located.

The measurements and calculation were performed iteratively. The first set of calculations shows the possibility of the conversion process and provides the information about the position for the measurements. Then the measurements were performed and the measured density profiles were used in the calculations instead of linear density profiles, as used in first set of calculations. This brings the calculations closer to the real situation in the WEGA plasma. In addition, the similarity of measured and calculated radial profiles of phase and amplitude are investigated. The obtained results allow to argue the mode conversion existence.

---

---

## 1.2. Overview

The thesis consists of eight main chapters and the appendix paragraph. Chapter 1 includes history, motivation, and overview. The 2<sup>nd</sup> chapter describes the experimental device. It is divided into four parts. First, the magnetic configuration, and the used diagnostics with short descriptions and typical results of measurements are presented. Then the description of the heating system and its improvements follows. At the end, the results of experiments with varied toroidal magnetic field are presented.

3<sup>rd</sup> chapter is devoted to the theory of the modes and mode conversions in the plasma. Here the modes, which take part in OXB mode conversion process, are described. The reason why two-step conversion is chosen for heating in WEGA, and the principles of O-SX and SX-B mode conversions are explained.

In the 4<sup>th</sup> chapter some examples of numerical simulations of the OXB process in the ray tracing approximation are shown. The 2D full-wave code, which solves the system of the Maxwell's equations are described here together with the applications of this code in this work. The full wave calculations are the basis for the experimental investigation of the WEGA plasma with HF and Langmuir probes as described in chapter 6.

In the 5<sup>th</sup> chapter the antenna geometry is described, methods of numerical and experimental investigations of the antenna pattern and results of these investigations are presented. Improvement of plasma parameters as a result of antenna optimization is shown. In addition, efficiency of the ECRH heating in WEGA is compared for the used antenna configurations. The data from different diagnostics are used here for the estimation of the absorbed part of the power.

Chapter 6 is dedicated to the measurement system used in the WEGA stellarator for the investigation of the wave activity in the plasma. The HF probes development and testing are described in this chapter as well as the measurement and data acquisition system.

In the chapter 7 the results of calculations and measurements are collected and compared. Here the optimal regime for the measurements defined. Data obtained from full-wave calculations are compared with measured profiles of phase and amplitude of the waves in plasma. This information allows to draw conclusions on the mode conversion process in the WEGA plasma.

The last chapter gives the conclusions about the mode conversion presence and its role in the plasma heating made from the obtained results of measurements and calculations.

---



## **2. WEGA stellarator**

WEGA is a classical mid-size stellarator, which toroidal vacuum chamber has a major radius of  $R = 0.72$  m and minor radius of  $r_0 = 0.19$  m. Hydrogen, Helium and Argon are used as working gas. The pulse duration varies from a few seconds up to a few minutes depending on the magnetic field strength and hence the dissipated energy in the field coils. Short shots are used for high magnetic field experiments, the long time shots may be performed with magnetic field strength up to 0.34 T. Thus, an operation of WEGA in steady regime is possible.

This chapter has four sections. Section 2.1 devoted to WEGA common properties like geometry and operating parameters. In section 2.2 some diagnostics installed at WEGA are described. The diagnostics which results are used in this work will be touched in this section. In section 2.3 the microwave heating system and the modification performed will be described. The last section 2.4 is devoted to experiments with a variation of the toroidal magnetic field strength.

### ***2.1. Magnetic configuration***

The magnetic field in WEGA is created by 40 planar toroidal field coils and 2 helical field coils. Additionally 2 vertical field coils are used in Helmholtz configuration<sup>11</sup>. (fig. 2.1).

The toroidal magnetic field coils were designed to operate with a magnetic field up to 2.5 T. But, the WEGA power supplies can not reach this value. For the pulse operation the magnetic field strength value may reach  $B_0 = 0.9$  T. For CW operation the half of this value may be reached  $B_0 = 0.34$  T. Actually, the value of the toroidal magnetic field was varied in different measurements between 0.04 - 0.1 T.

The 2 helical field coils have five turns around the minor radius and two around major radius, so WEGA has  $l = 2$ ,  $m = 5$  configuration. The helical field coils create the

---

<sup>11</sup> A pair of magnetic field coils in Helmholtz configuration consists of two identical circular magnetic coils that are placed symmetrically one on each side of the experimental area along a common axis, and separated by a distance equal to the radius of the coil.

---

poloidal component of magnetic field. The resulting magnetic field lines are twisted in poloidal direction of the torus. Such a magnetic field configuration is needed to compensate outward drifts of particles [22]. The measure of the magnetic field twist is the rotational transform  $\iota$  it can be defined as a ratio of poloidal and toroidal magnetic fluxes.

$$\iota(r_{eff}) = \frac{RB_{\theta}(r_{eff})}{r_{eff}B_{\phi}(r_{eff})} \quad (2)$$

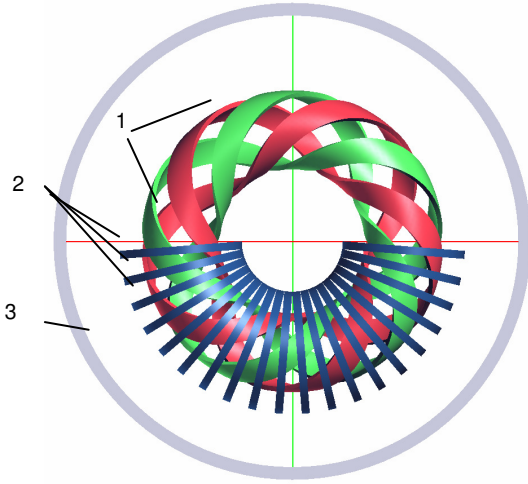


Fig.2.1. The magnetic field coils of the WEGA stellarator: 1-helical coils, 2-toroidal field coils, 3-vertical field coils

Where  $r_{eff}$  is the effective radius, it is the minor radius of a torus with cylindrical cross-section and the same major radius  $R$ , that contains the same volume as magnetic surface found in position  $r$ .  $B_{\theta}$  and  $B_{\phi}$  are the poloidal and the toroidal components of the magnetic flux respectively. Geometrically, rotational transform is the number of toroidal rotations that are necessary for one poloidal rotation.

The current in the helical coils also differs for pulsed and CW regimes of operation. In pulsed regime, current may raise up to 10 kA in CW operation  $\approx 3.5$  kA. Thus, the rotational transform  $\iota$  on the axis may vary from  $\iota/2\pi \approx 0.2$  to  $\iota/2\pi \approx 1$  in the case of low toroidal field. For a rotational transform of  $\iota/2\pi < 0.2$  the plasma size is so large, that the LCFS touches the torus wall.

## 2.2. WEGA layout and diagnostics

Various methods of plasma diagnostics are used in WEGA. The diagnostics used in this work as a reference for indication of heating regime improvement will be shortly described here.

The arrangement of the installed diagnostics is shown schematically in fig. 2.2. The orange colour marked diagnostic is the high frequency probes diagnostic that was developed for the EM waves investigation in the region of 6 kW heating antenna which position is also shown in the picture as well as the 20 kW antenna port. This diagnostic

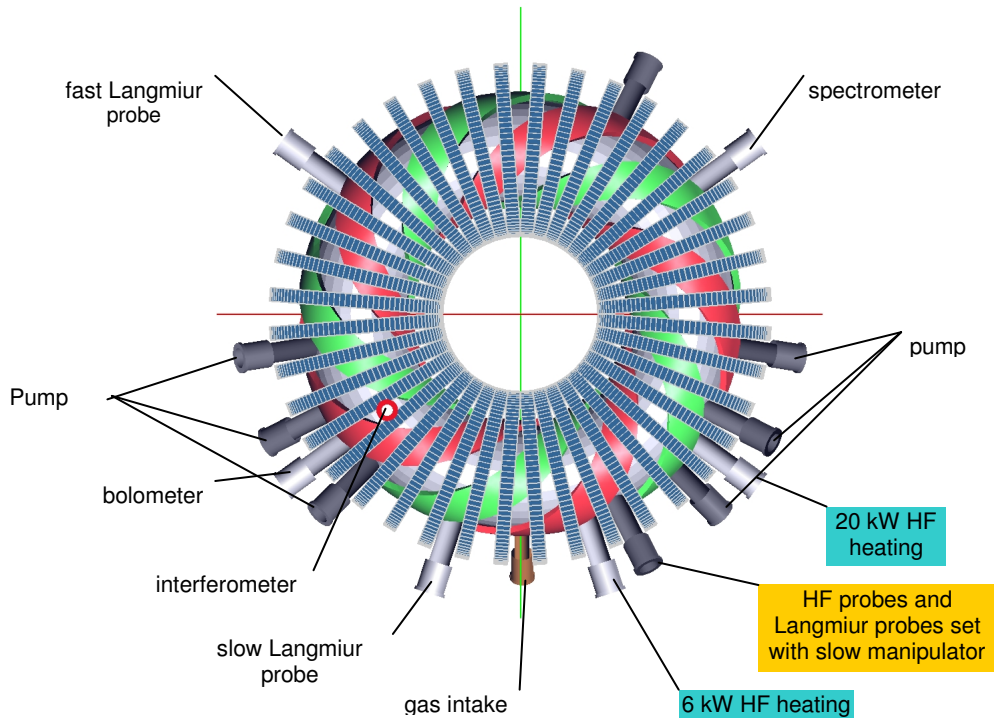


Fig.2.2. The diagnostics on the WEGA and the heating and pumping ports location. On the orange background is the port used for HF and Langmuir probes described in chapter 6.

will be described in detail in chapter 6. Additionally the gas intake and pumping ports are marked here.

### 2.2.1. Interferometer

At WEGA, a single-channel Mach-Zehnder type interferometer is installed [9]. The probing O-mode wave has a frequency of 80.605 GHz ( $\lambda = 3.72$  mm). The cutoff density of this frequency is  $n_{cutoff} = 8 \times 10^{19} \text{ m}^{-3}$ , so the density of the plasma in WEGA is always below the cutoff value for this frequency. The line of sight is vertical and points approximately through the centre of the vessel ( $R_{int} = 73$  cm). If the  $n_e/n_{cutoff} \ll 1$  the line integrated density value is given by

$$n_{ei} = \frac{\varphi_i}{2\pi} 2\lambda n_{cutoff}. \quad (3)$$

Where  $\varphi_i$  is a phase shift measured by interferometer. A common method for interferometer data evaluation is to determine the average  $n_e$  value in the magnetically confined plasma region by dividing the measured line integrated  $n_{ei}$  with the path length

of the wave inside the LCFS, because usually  $n_e$  outside LCFS is negligible. In the case of WEGA plasmas, this assumption does not hold. Hence, only the average  $n_e$  value along the minor diameter of the vessel by dividing the line-integrated  $n_{ei}$  on the diameter of the torus could be obtained.

### 2.2.2. Fast reciprocating Langmuir probe

The main information about the plasma heating efficiency is derived from the fast Langmuir probe diagnostic [10]. The Langmuir probe is installed on the fast reciprocating manipulator, which allows to measure the radial profiles of plasma density, temperature, and potential from the plasma centre to the edge of the vacuum vessel. By triggering, the manipulator rapidly inserts the probe in the plasma and moves it back. The whole movement takes approximately 1.5 s. During the movement, a sawtooth voltage is applied to the Langmuir probe in the range from -100 to 20 V with a frequency of  $\sim 100$  Hz. As a result, the current-voltage (I/U) characteristics along the way of probe obtained.

The fast movement of the Langmuir probe allows to avoid the probe tip heated by the plasma. Thus, thermal electron emission from the probe head is avoided, which may

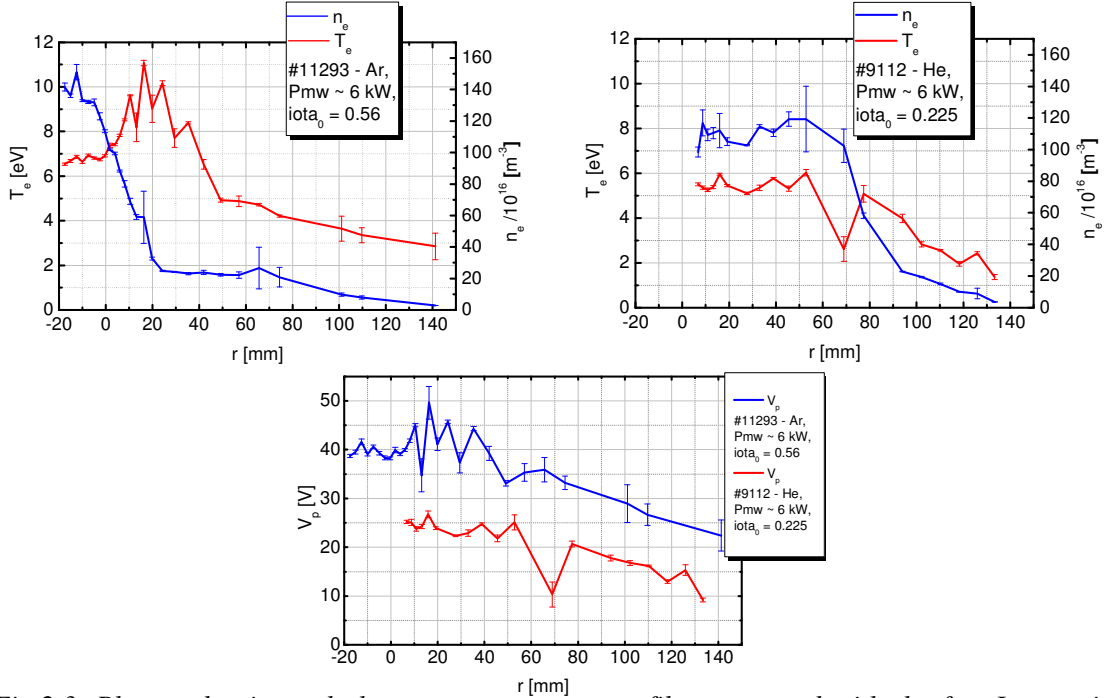


Fig.2.3. Plasma density and electron temperature profiles measured with the fast Langmuir probes. For high  $iota$  value 0.56 (upper left) and for low  $iota$  value 0.2 (upper right) plasma potential for high and low  $iota$  case (bottom)

negatively affect on the measurements precision.

The measured  $I/U$  characteristics showed a common feature: the non-saturation of the ion current. Possible cause is a two-temperature distribution of the electron energy. In order to determine the plasma parameters from the measured data the characteristics have been fitted with a formula proposed by P. Stangeby [12] assuming a two-temperature Maxwellian distribution. With a MPFIT program written on IDL the  $I/U$  characteristics have been fitted and the main plasma parameters were extracted. Program MPFIT uses the Levenberg-Marquardt technique to solve the least-squares problem [11].

The results of the fast Langmuir probe measurements are used in different parts of this work. Typical measured density and temperature profiles are shown in fig. 2.3 [10].

Typical values of parameters determined with this diagnostic are following:

Electron density:  $1 \times 10^{17} \text{ m}^{-3} < n_e < 5 \times 10^{18} \text{ m}^{-3}$ ;

Plasma potential:  $15 \text{ V} < V_p < 60 \text{ V}$ ;

Temperature of slow electrons:  $3 \text{ eV} < T_{es} < 12 \text{ eV}$ ;

Temperature of fast electrons:  $T_{ef} \sim 400 \text{ eV}$ ;

Fraction of fast electrons:  $f_n < 5 \%$ .

The obtained electron density values were compared with the interferometer and spectrometer data. The probe gives to high  $n_e$  values, but the overestimation of  $n_e$  may be explained with the possible violation of some assumptions in the probe model:  $T_i \ll T_e$ ; singly charged ions. In addition, the large ion Larmor radius compared to the probe radius can be a cause of too high  $n_e$  values. The Larmor radius for Helium in WEGA conditions ( $B_0 = 0.057 \text{ T}$ ,  $T_i = 5 \text{ eV}$ ) is  $\rho_i^{He^+} \sim 8 \text{ mm}$  while the standard Langmuir probe size is  $l = 2 \text{ mm}$  (length) and  $\varnothing = 0.9 \text{ mm}$  (diameter). The electron Larmor radius is much smaller than the probe pin  $\rho_e \sim 10 \mu\text{m}$ . Therefore, the electron density values measured by the Langmuir probe are calibrated with those from the interferometer measurements.

### 2.2.3. Bolometer

A 12-channel bolometer camera has been installed in the WEGA stellarator to measure the radiation power losses of ECR-heated plasmas [23]. Each channel has a gold foil absorber and. The absorbed power is monitored by a resistance change due to the temperature rise of the foil [13]. The camera was positioned in the mid-plane viewing the plasma from the low-field side with a spatial resolution of about 6 cm, as

---

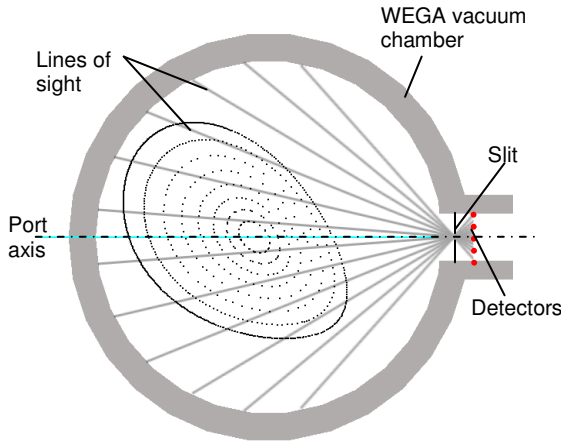


Fig.2.4. Bolometric arrangement.

*Lines of sight cover whole poloidal cross-section*

by linear extrapolation of the integrated radiation power measured in the viewing region to the whole plasma or torus volume, is generally  $\sim 30\%$  of the ECRH power and depends on the net ECRH input power and the magnetic configuration.

It has been observed that the edge radiation depends strongly on the shape and size of plasma (hence the magnetic configuration) facing the used ECRH antenna. Through radial inward shifting of the plasma or changing the polarity of the helical field as well as the toroidal position of the used ECRH antenna the edge radiation can be reduced. The non-negligible edge radiation outside the confined plasma region indicates a broad deposition profile of the input ECRH power [23]. It was found that for a given working gas and in case of high  $\iota$  the radiation power fraction decreases with increasing ECRH-heating power.

### 2.3. Plasma heating system

The plasma is ignited and heated by ECR with a maximum power of 20+6 kW coming from two separate magnetrons operating at frequency of 2.45 GHz. The microwave is launched in equatorial plane of the torus at two toroidally shifted positions using two A-ports  $36^\circ$  distance in toroidal direction as shown in fig. 2.2.

Cyclotron heating based on a resonance, which occurs in the region of plasma where the electron-cyclotron frequency  $f_{ce}$  is equal to the heating wave frequency.

$$f_{ce} = \frac{eB_0}{2\pi m_e c}, \quad (4)$$

The cyclotron frequency depends on the magnetic field strength  $B_0$ . Because of the low heating frequency, most of the experiments have been provided for  $B_0 \sim 0.0875$  T where 0.0875 T is the electron cyclotron resonant field for the 2.45 GHz heating frequency.

The transmission lines for the 6 kW and the 20 kW magnetrons are shown in fig. 2.5. Here two lines are presented for 6 and 20 kW heating power. The heating system will be described here parallel with the improvements made on the new 20 kW heating line.

### 2.3.2. Transmission line

The heating system of WEGA was been enhanced by adding a 20 kW magnetron with a separate transmission line. The 6 kW magnetron and its transmission line can be operated simultaneously with the 20 kW magnetron. Both magnetrons operate at the same frequency of 2.45 GHz. Therefore, the transmission line for 20 kW magnetron has the similar main elements as the 6 kW heating line, but with improved electrical parameters. Improved parameter means the technical characteristics of the transmission line elements, which allows to operate of a higher power of HF from the magnetron. In the following description, the “6 kW line” notation will be used for the line where the

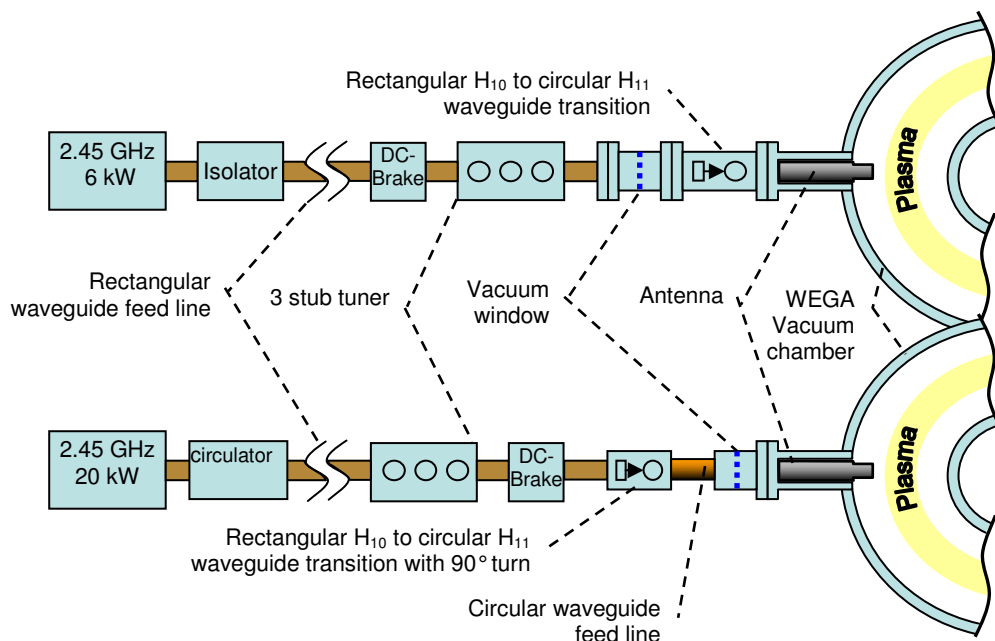


Fig.2.5. Scheme of the heating system used on the WEGA stellarator for the 6 kW magnetron (upper) and for the 20kW (lower)

---

6 kW magnetron is installed and “20 kW line” for the line where the 20 kW magnetron is used.

From the magnetrons to the antennas, HF is fed through a  $H_{10}$  flexible  $72 \times 34$  mm for 6 kW line and  $86.4 \times 43.2$  mm for the 20 kW line. For 6 kW line a flexible waveguide is used. In order to avoid the reflected power coming back to the magnetron an isolator is installed directly after the magnetron output. On the 20 kW line a water-cooled circulator is installed for this purpose.

The 3-stub tuners minimize the reflected power by matching the impedance of the line with the impedance of the antenna and plasma. It is planned to install an E-H tuner on the 20 kW line but up to now, 3-stub tuners are working on both lines. The only difference is that on the 20 kW line it the stub positions are fully automatically adjusted according to the signal measured by directional coupler for transmitted and reflected power.

A DC-brake separates the magnetrons from the WEGA vessel electrically, but does not affect the HF power transmission. The DC brake is nothing else than just a throttle waveguide connection with a thin dielectric putted between the flanges. A detailed description of this element is given in Appendix A. The same DC-brake configuration is used for both lines, but for the 20 kW line, it is optimized for larger waveguide dimensions. The design of this part for 20 kW line was developed using a HFSS code.

Then the HF wave passes through a vacuum window and a rectangular  $H_{10}$  to circular  $H_{11}$  waveguide transition. The transition is positioned after the vacuum window in the case of the 6 kW line and before vacuum window in the case of the 20 kW line. For the 20 kW line, the vacuum window installed in circular waveguide section and has larger area and less local heating. The  $H_{10}$  to  $H_{11}$  transformer in the 20 kW line has another design with the  $90^\circ$  turn on it. On the 6 kW line, it is simply a smooth rectangular to circular transition.

On the 6 kW line, a quartz vacuum window is used. The thickness of this window is not adapted to minimize the HF reflection, and size of this window is smaller than the window in the 20 kW transmission line. The not optimized vacuum window in 6 kW line operates normally because of comparatively low inserted power. However, the vacuum window for the 20 kW line has been optimized to minimize the reflected power and the heating during high power operation. This window has circular shape, half wavelength thickness and is made of AlN ceramic. It is separately described in Appendix B.

---



Also in the 6 kW transmission line a directional coupler is installed. The outputs of the directional coupler have 60 dB attenuation. It allows detecting the incoming and reflected power in the heating transmission line. In addition, the incoming wave signal from this directional coupler is used for the phase measurements described in chapter 6 as a reference signal.

A new pulsed magnetron is in preparation for installation on WEGA. The 6 kW transmission line will be used for future operation. This magnetron has also maximum 6 kW output power, but can be switched off very rapidly. Documented decaying time of the output power of this magnetron is 10  $\mu$ s. Such fast switching of the heating power allows to measure the particles confinement time.

### **2.3.3. Heating improvement by mode conversion**

The previously described improvements mostly concern to the technical part of transmission line. A second way to improve the heating is to follow the reasons of the low heating efficiency and try to solve this problem.

The main reason of the low heating efficiency in the WEGA stellarator is overdense plasma. The wave is launched with O- or X-polarization in equatorial plane from low field side of the torus. In this case, the wave can not reach the cyclotron resonance region in the center of the plasma in O-mode as well as in the X-mode. Heating wave meets cutoff barrier at the edge of the plasma where electron density reaches its critical value  $n_{cutoff}$ . It is assumed that the plasma is heated mostly by the multiple reflections of the O-mode between the cutoff layer and the vacuum chamber wall. Such heating mechanism results in the low plasma density just slightly higher than the cutoff density, but the plasma stays overdense. The profiles have been measured by the different diagnostics will be presented in the chapter 5.2.

The main candidate for improving the heating efficiency by overcoming the cutoff barrier is the electrostatic Bernstein mode (B-mode) [17]. The main advantage of this mode is that it has no upper limit of the plasma density for propagation. The Bernstein wave can penetrate the overdense plasma region and heat the center of the plasma. However, this wave can not propagate in the region outside the plasma, which is separated by the Upper Hybrid Resonance (UHR) layer<sup>12</sup>. To obtain the EBW inside the plasma a scheme with the mode conversion should be used it will be discussed in ch. 3.

---

<sup>12</sup> Layer where the frequency of heating wave equal to  $\omega_{UHR}$  (see 3.5)

## 2.4. Magnetic field variation experiments

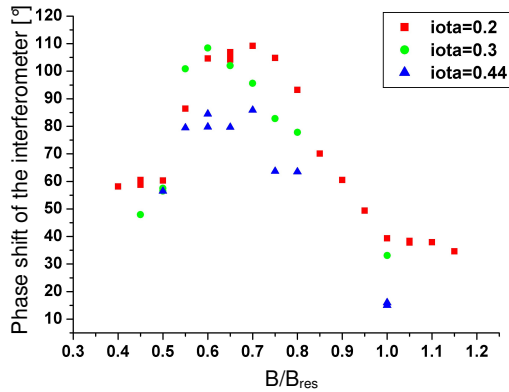


Fig.2.6. The phase shift of the interferometer, proportional to integral density, over the toroidal magnetic field normalized on the resonant magnetic field strength value.

However, an increase of the density and the electron pressure is observed [10]. Probably, the reason is improved magnetic confinement due to the higher magnetic field strength.

It is assumed that the confinement time of the particles raises, the electron density increases and gives rise to the ionization. This can be checked with the confinement time measurement using the pulsed 6 kW magnetron and will be done in future.

In addition, the experiments with magnetic field strength variation near the resonant value were performed and the maximum of linear density was found for  $B_0 = 0.65 \times B_{res}$  (fig. 2.6). The reason for it is mostly the low gradient of the magnetic field in WEGA. If the cyclotron resonance layer is in the center of the vacuum chamber, the magnetic field in front of the antenna is also close to the resonant value and the HF power is mostly absorbed near the antenna. The same happens during the operation close to the second harmonic  $0.5 \times B_{res}$ . Therefore, in both cases, the edge heating with hollow profiles is observed, and the integral density is low.

In addition, the Doppler-shifted electron absorption was discussed as possible explanation of this behaviour. However, this effect is small in the WEGA stellarator and it can not explain found optimum  $B_0 = 0.65 \times B_{res}$  [10].

Another possible reason is the OXB process. The O-mode to SX-mode conversion efficiency depends on the magnetic field it is discussed in chapter 3. Thus, the total efficiency of OXB is dependent on the magnetic field strength.

To investigate the heating efficiency experiments with varying magnetic field strength have been carried out. Such experiments have been performed for  $B_0 = 4 \times B_{res}$  where  $B_{res}$  is the resonant field strength  $B_{res} = 0.0875$  T. The heating in this case is no more resonant, because the resonant field strength is outside of the plasma vessel. In this case, it is assumed that the heating process is mostly by the collisional damping during multiple reflections between cutoff layer and the wall.

### **3. OXB theory on ECR heating**

The Ordinary to Extraordinary to Bernstein (OXB) mode conversion process proposed by Preinhaelter and Kopecký [19] consists of two steps. First an externally launched O-mode is coupled to a slow X-mode (SX) in the region of the O-mode cutoff layer ( $n_e = n_{cutoff}$ .) The SX-mode propagates to the upper-hybrid resonance (UHR) layer where it is converted to an electrostatic Electron Bernstein wave (EBW). The EBW propagates freely in the overdense plasma and is absorbed in the cyclotron resonance region. This two-step OXB process overcomes the O-mode cutoff density barrier and allows heating of the inner region of plasma, which is inaccessible to the O or X-mode.

In this chapter, a basic introduction to the O, X (section 3.1) and B-modes (section 3.2) is presented. These modes are involved in the OXB conversion process so it is important to understand their nature. In section 3.3 the reason why the mode conversion is needed for WEGA is discussed. The coupling mechanism of the O-mode to X-mode and X- to B-mode is explained in sections 3.4 and 3.5

#### **3.1. Ordinary and Extraordinary modes**

An electromagnetic wave propagating in an unmagnetized plasma with angular frequency  $\omega$

$$\omega \gg \sqrt{\frac{4\pi n_e e^2}{m_e}} \quad (5)$$

has the same velocity as an electromagnetic wave in vacuum. This is also true if the plasma density

$$n_e \ll \frac{m_e \omega^2}{4\pi e^2}. \quad (6)$$

As the density increases, the phase velocity of the wave increases, and the group velocity decreases until the cutoff frequency is reached, where the wave frequency  $\omega$  is equal to the plasma frequency.

$$\omega_{pe} = \sqrt{\frac{4\pi n_e e^2}{m_e}} \quad (7)$$

This density is known as the critical or cutoff density

---

$$n_{cutoff} = \frac{m_e \omega^2}{4\pi e^2} \quad (8)$$

Phase velocity of the wave tends to infinity and the group velocity tends to zero. Wave can not propagate in the regions where the density cutoff value is exceeded

If the critical density is exceeded, the plasma is called overdense.

In magnetized plasma, particles rotate around the magnetic field lines at the cyclotron frequencies. For electrons the cyclotron frequency is

$$\omega_{ce} = \frac{eB_0}{m_e c}. \quad (9)$$

In cold magnetized plasma, two modes can be excited. In case of a wave vector  $\vec{k}$  parallel to  $\vec{B}_0$ , they are called R and L modes. For  $\vec{k}$  perpendicular to  $\vec{B}_0$  it is O and X-mode. For all but the O wave, the cutoff relationships are more complex in magnetized plasma.

The ordinary wave (O-mode) is linearly polarized with  $\vec{k} \perp \vec{B}_0$ , and  $\vec{E} \parallel \vec{B}_0$ . It has a cutoff at the  $n_{cutoff}$  density. The dispersion relation is similar to that one at the unmagnetized plasma, because the electron motion is not affected by  $\vec{B}_0$ :

$$\frac{c^2 k^2}{\omega^2} = 1 - \frac{\omega_p^2}{\omega^2} \quad (10)$$

The extraordinary (X-mode) wave has a more complex dispersion relation.

$$\frac{c^2 k^2}{\omega^2} = 1 - \frac{\omega_p^2}{\omega^2} \frac{\omega^2 - \omega_p^2}{\omega^2 - \omega_{ce}^2} \quad (11)$$

It is partly longitudinal (with  $\vec{E} \parallel \vec{k}$ ) and partly transverse  $\vec{k} \perp \vec{B}_0$ ,  $\vec{E} \perp \vec{B}_0$ . As the density is increased, the phase velocity rises from  $c$  until the R-cutoff is reached where  $\omega = \omega_R$ . In this region, the X-mode is called fast extraordinary (FX) wave. As the density is further increased, the plasma is evanescent until the upper hybrid resonance layer (UHR) where frequency is  $\omega = \omega_{UH}$ . Then X-mode can propagate again until the L-cutoff at  $\omega_L$ . Between UHR layer and L-cutoff the X-mode called slow extraordinary (SX) wave. This notation comes from the phase velocity of X waves, which is higher for FX-mode and lower for the SX-mode. The cutoff frequencies of FX and SX modes and UH frequency  $\omega_{UH}$  are given by:

$$\omega_R = \frac{I}{2} \left[ \omega_{ce} + \sqrt{\omega_{ce}^2 + 4\omega_p^2} \right] \quad (12)$$

$$\omega_L = \frac{I}{2} \left[ -\omega_{ce} + \sqrt{\omega_{ce}^2 + 4\omega_p^2} \right] \quad (13)$$

$$\omega_{UH} = \sqrt{\omega_{pe}^2 + \omega_{ce}^2} \quad (14)$$

For oblique wave propagation the modes are also called X and O mode, the dispersion relation is given in section 3.4

The R wave and the L wave are circularly polarized  $\vec{E} \perp \vec{B}_0$ , with opposite directions of rotation. The R-wave has a right-handed circular polarization. Its dispersion relation is given by:

$$\frac{c^2 k^2}{\omega^2} = I - \frac{\omega_p^2 / \omega^2}{I - (\omega_{ce} / \omega)} \quad (15)$$

The L-wave is left-handed circular polarized.

$$\frac{c^2 k^2}{\omega^2} = I - \frac{\omega_p^2 / \omega^2}{I + (\omega_{ce} / \omega)} \quad (16)$$

The R wave has a cutoff at  $\omega_R$  and a resonance at  $\omega_c$ . The L wave has a cutoff at  $\omega_L$  and no resonance. R waves at frequencies below  $\omega_c/2$  are also known as whistler modes.

The centre of the plasma is not accessible to either O- or X-modes. To access the central resonant region requires a mode with no density limit is needed. The Electron Bernstein mode is a good candidate.

### 3.2. Electron Bernstein Wave

The Electron Bernstein Wave (EBW) is a longitudinal electrostatic wave that occurs in hot magnetized plasma. It is named after Ira B. Bernstein, who described the mode in 1958 [17]. Fig. 3.1 shows the physical mechanism for a typical EBW. The EBW propagates in plasma perpendicular to an external magnetic field for a particular arrangement of charge separation. The EBW occurs when electrons rotate in the external magnetic field with finite Larmor radius. Its phase is organized in such a way that the space charge distribution has maxima and minima, which are periodically distributed perpendicularly to external magnetic field lines. The charge separation in

---

this direction is possible only if the electrons rotate in magnetic field with finite Larmor radius  $\rho$  arising from finite electron temperature  $T_e$ , or thermal velocity, respectively.

$$\rho = \frac{c}{eB} \sqrt{k_B T_e m_e} \quad (17)$$

The electron temperature must be taken into account to explain the EB-mode existence and propagation. In a cold plasma the EBW does not occur. Electrons in cold plasma have freedom to move only along the magnetic field lines and charge separation is possible only in the direction of magnetic field except of the case of X-mode propagation. Here, the electric field of the wave is applied perpendicular to magnetic field direction and the electron is compelled to rotate around external magnetic field line. But, in this case the phase of the rotation is defined by the X-mode and can not be organized to sustain the B-mode.

Fig. 3.1 shows that the EBW mode has purely electrostatic character. The wavelength of the mode is of the order of  $\rho$ , but can differ because fast electrons can take part in the EBW propagation.

The phase organization can be explained by considering a wave that propagates in the plasma with  $\vec{k}$  perpendicular to  $\vec{B}_0$ , frequency  $\omega \approx \omega_{ce}$ , and wavelength four times the Larmor radius ( $\lambda = 4\rho$ ). An observer moving with the wave phase velocity and observing an electron in the plasma will see that, during first half period of the electron gyro rotation, the electron moves with the wave and experiences a constant force from the electric field of the wave. This is like an electron in a static E field. During the next half period, the electron moves in the opposite direction to the wave.

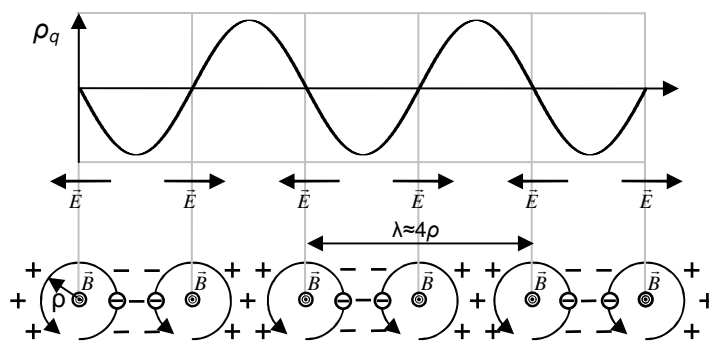


Fig.3.1. The space charge distribution  $\rho_q$  due to the phase of the electron rotation organization in an externally applied EM wave. The blue curve corresponds to a 2<sup>nd</sup> harmonic applied wave.

It moves one wavelength back in the wave coordinate system. The average force in the second half period is zero because the electron experiences the force from the positive and negative electric field of the wave equally. This is like an electron in a rapidly varying E-field (fig. 3.2).

As shown in fig. 3.2, in the first half period, the

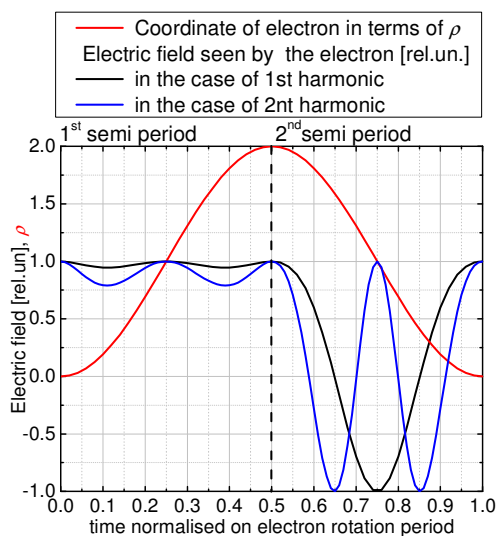


Fig.3.2. The Electric field of the applied longitudinal wave seen by an electron rotating with finite Larmor radius

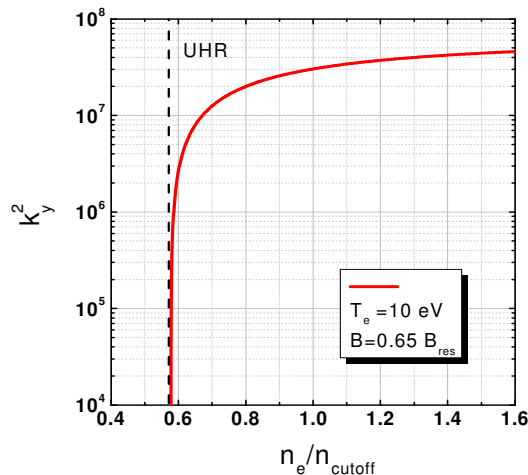


Fig.3.3. EBW dispersion relation for  $B_0 = 0.65 \times B_{res}$ ,  $T_e = 10$  eV

situation is the same as in Landau damping, where the particle velocity and wave phase velocity are comparable ( $v \approx \omega/k$ ). The electron loses energy when its velocity is slightly higher than the velocity of the wave and gains energy when its velocity is slightly lower than the wave velocity. The result of many electrons interacting is the gyro-rotation phase organization, which leads to the periodical charge separation perpendicular to the magnetic field lines, as shown in fig. 3.1.

This description is also valid for higher cyclotron harmonics  $\omega \approx n\omega_{ce}$  ( $n = 1, 2, 3, \dots$ ). The phase velocity of this electrostatic wave is equal to the electron rotation velocity so the description is restricted not on certain frequencies or wavelengths, but on integral relation of  $\omega$  to  $k$ . The phase organization is also possible for higher harmonics  $\lambda = 4\rho/n$ .

For the wave in the neighbourhood of the hybrid resonance and temperature range of the WEGA the EBW dispersion which describe the first EBW harmonic is given by Preinhaelter & Kopecký [19]

$$k_y^2 = \left(1 - \frac{\omega_p^2}{\omega^2 - \omega_{ce}^2}\right) \frac{2(\omega^2 - \omega_{ce}^2)(\omega^2 - 4\omega_{ce}^2)}{3v_{Te}^2 \omega_p^2} \quad (18)$$

In fig. 3.3 the dispersion curve is plotted as a function of density using this equation. The main advantage of the EB-mode for plasma heating is the absence of a high-density propagation limit. When the plasma frequency is higher than cyclotron frequency,  $\omega_p > \omega_{ce}$ , the Larmor gyro radius becomes larger than the Debye sphere radius. In this case, information about the space charge distribution inside the Debye sphere may be transferred outside the sphere. However, the condition  $\omega \geq \omega_{ce}$  is required to enable the phase organization of the electron gyro rotation necessary to establish the EBW.

The EBW can not propagate outside the UHR layer or outside the plasma, the wave is trapped inside the region bounded by the UHR layer. At the UHR layer, the EBW is fully converted into the SX-mode. In overdense plasma, SX-mode propagates back to the UHR layer after reflection from the L-cutoff layer and. At the UHR layer, it is converted into an EB-mode, which travels back into the plasma as shown in fig. 3.4.

The only case, when this scheme is interrupted is, when the SX-mode, after conversion, reaches the O-mode cutoff layer with its  $\vec{k}$  direction optimum for coupling with the O-mode, as described in 3.4. In this case, the O-mode propagates out of the plasma. This BXO process has been used in an overdense plasma emission diagnostic in W7-AS [20,21].

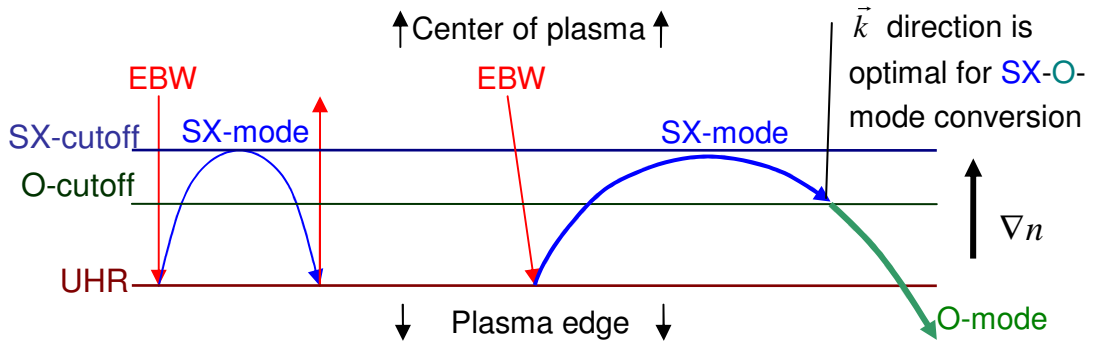


Fig.3.4. Trapping of the EBW and SX wave inside the UHR bounded region.

### 3.3. Two-step conversion

The region outside the UHR layer is evanescent for the EBW. Thus, the EBW can not be directly launched outside of the plasma. The EBW must be excited inside the region bounded by the UHR layer. Thus, mode conversion from X to EB-mode is required to generate the EBW.



In fig. 3.5 the typical situation for overdense toroidal plasma is shown. In this figure, the density and toroidal magnetic field distribution are plotted over the poloidal cross-section. Density is normalized to  $n_{cutoff}$  and magnetic field to  $B_{res}$ . The vertical lines show the positions of the cutoffs and resonances described in section 3.1.

There are two main techniques to generate EB waves in the centre of overdense plasma. The first is to launch an X-mode from the high field side of the torus. The X-mode converts to the B-mode on the UHR layer, and then the B-mode propagates into

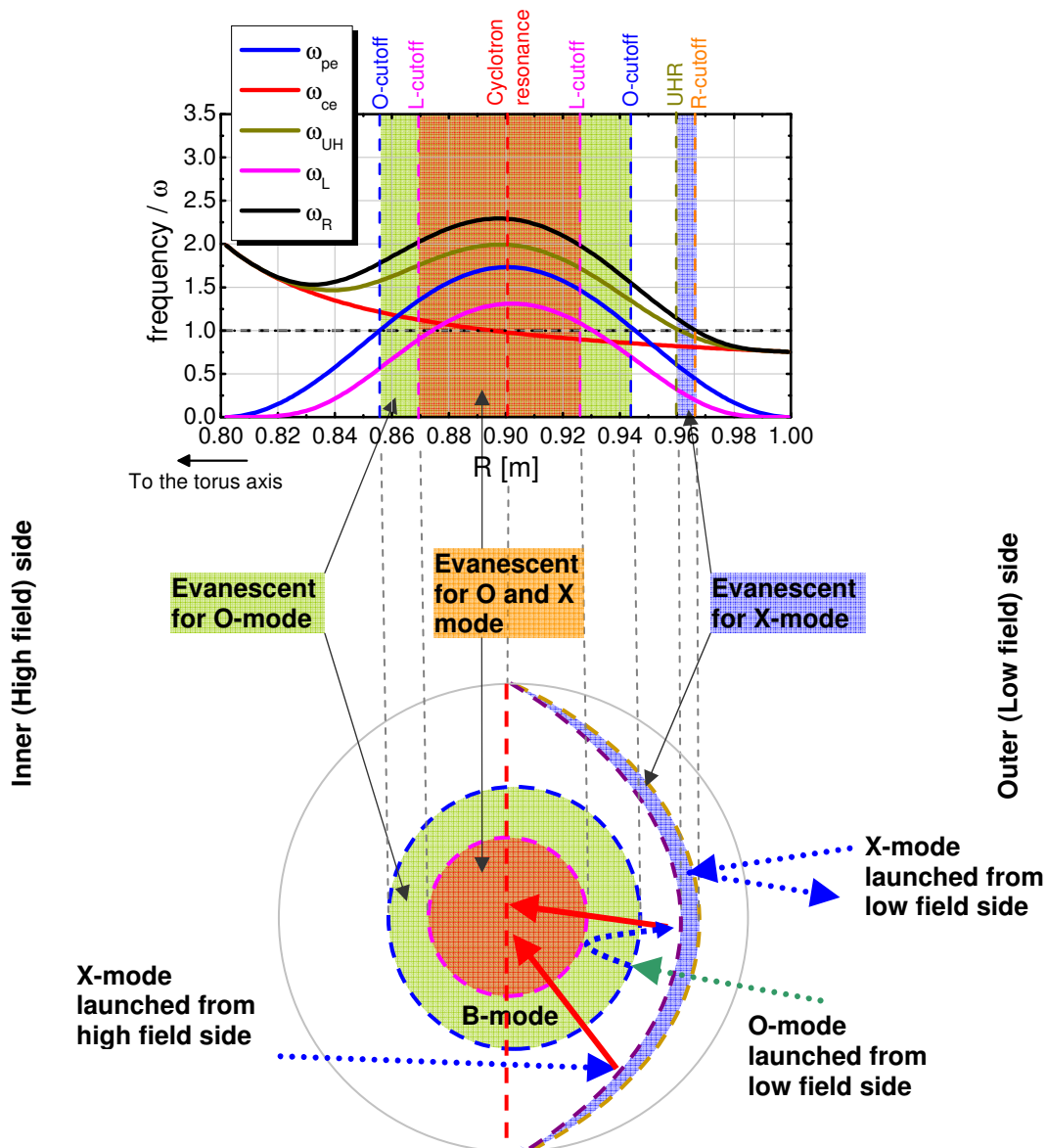


Fig.3.5. Cutoffs and resonances in toroidal plasma, frequencies on upper plot normalized to heating wave angular frequency  $\omega$

the overdense plasma region. In fig. 3.5 this corresponds to launching of the X-mode (blue dashed arrow) from the high field side.

This scheme is under investigation in TJ-II [37]. For WEGA stellarator, this is not possible because of the high steepness of density. The L-cutoff layer<sup>13</sup> in the WEGA plasma is extended almost to the O-cutoff layer position. Latter is also much closer to the outer border of plasma than it is shown in the fig. 3.5. Additionally there are no ports to access the inner side of the plasma.

If the X-mode is launched from low field side, there is strong reflection of the X-mode from the R-cutoff layer and very low heating efficiency. In fig. 3.5 this is shown by the X-mode launched from “low field” side.

The second way to obtain the B-mode is via the OXB mode conversion process. In this case, the HF power is launched from the low field side of the torus in the O-mode. The O-mode converts to the SX-mode, the SX-mode to B-mode, and the B-mode propagates inside the plasma and heats the electrons. In fig. 3.5 it corresponds to the O-mode (green dashed arrow) launched from the low field side. This two-step process may be applied in WEGA. However, it requires additional conditions to be fulfilled.

### 3.4. O-SX conversion

The O-SX conversion process is similar to the Brewster angle full transmission effect.

The phenomena of full transmission of light, which is polarized in the plane of incidence from one transparent media with refraction index  $n_1$  to another with  $n_2$ , is based on the oblique incidence of a light ray with optimum Brewster angle equal to  $\arctan(n_2/n_1)$ .

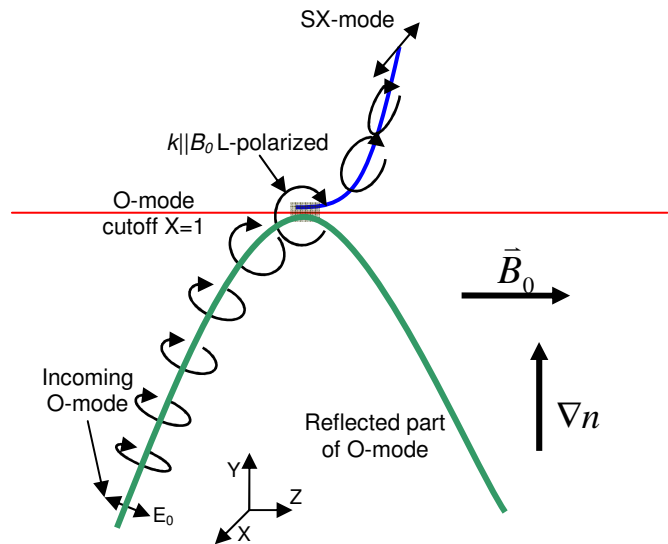


Fig.3.6. Propagation and coupling of the O-mode to the SX-mode for optimal oblique launch of the O-mode.

<sup>13</sup> In fig. 3.5. it is shown by the magenta dashed line

The effect of total internal reflection occurs when a ray of the light comes from a medium with higher refractive index to a medium with lower refractive index ( $n_1 > n_2$ ) with the incidence angle larger than the total internal reflection angle  $\arcsin(n_2/n_1)$ . This phenomenon is used, for example, in optical fiber transmission lines.

For oblique or perpendicular incidence, some of the light usually propagates in the other media, while some is reflected at the border.

Similar situations are observed in dense magnetized plasma found in stellarators and tokomaks.

Consider a cold plasma slab with homogeneous magnetic field  $\vec{B}_0$  in the  $z$ -direction, a density gradient along the  $y$ -axis and EM wave vector  $\vec{k}$  in the  $yz$ -plane as shown in fig. 3.6. If the density scale length,  $L_n$ , is much larger than the wavelength  $\lambda$ ,

$$L_n = \frac{n_e}{dn_e/dx}, L_n \gg \lambda, \quad (19)$$

the EM waves satisfy to the Appleton-Hartree dispersion relation for oblique propagation [38]

$$n_y^2 + n_z^2 = 1 - \frac{2X(I-X)}{2(I-X) - Y^2 \sin^2(\theta) \pm \Gamma}; \quad (20)$$

where

$$\vec{n} = \frac{\vec{k}c}{\omega}, \quad (21)$$

$$\Gamma = [Y^4 \sin^4(\theta) + 4(I-X)^2 Y^2 \cos^2(\theta)]^{1/2}; \quad (22)$$

Here  $n_y, n_z$  are the components of the refractive index vector,  $X = \omega_p^2/\omega^2$  is the dimensionless density,  $Y = \omega_c/\omega$  is the dimensionless magnetic field,  $\theta$  is the angle between  $\vec{k}$  and  $\vec{B}_0$ . The positive and negative sign in the denominator of eq.20 correspond to the O-mode and X-mode respectively.

The O and X-modes coincide at  $X = 0$  and  $X = 1$ . The first case,  $X = 0$ , corresponds to vacuum wave propagation. In the second case,  $X = 1$ , the O and SX branches are connected and form the O-SX curve shown in fig. 3.7.

In general, there are evanescence regions for the curve where  $n_y^2 < 0$ . This is where the O-mode is reflected at the cutoff layer. The continuation of the O-SX curve in evanescent region may be minimized if  $\Gamma \approx 0$ . In this case O-SX curve only touch the evanescent region border. This requires that  $X = 1$  and  $Y \sin(\theta) = 0$  so  $\theta = 0$ . Thus  $\vec{k}$

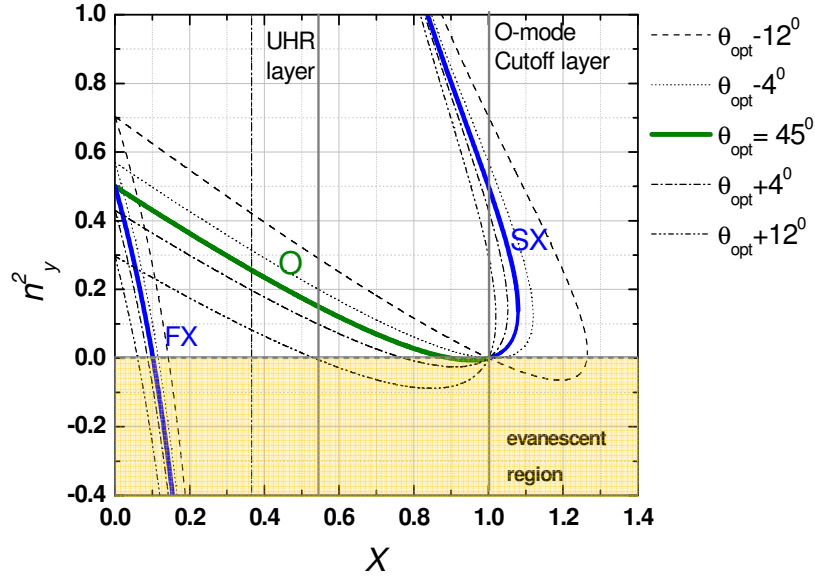


Fig.3.7. The Appleton-Hartree dispersion relation plotted in dimensionless coordinates. The optimal incident angle is shown with a solid line. The other curves show cases where the incidence angle deviates from the optimum angle for O-SX conversion

should be parallel to  $\vec{B}_0$  at the O(SX)-mode cutoff point. As  $\theta$  tends to zero the  $n_y$  component of the refractive index vector also tends to zero. In this case eq.20 gives,

$$n_z^2 = n_{z,opt}^2 = \frac{Y|_{X=1}}{Y|_{X=1} + 1}, \quad (23)$$

where the value of  $Y$  is taken at the point  $X = 1$ .

Since the  $n_z$  component in the slab is unchanged, the optimum direction of the incident O-mode wavevector is given by  $\vec{n} = (\theta, \sqrt{1 - n_{z,opt}^2}, n_{z,opt})$ . The O-SX curve shown in fig. 3.7 does not enter the evanescent region when the insertion angle  $\theta_{ins}^{14}$  is optimal.

$$\theta_{opt} = \arccos\left(\sqrt{\frac{Y|_{X=1}}{Y|_{X=1} + 1}}\right) \quad (24)$$

<sup>14</sup>  $\theta_{ins}$  is the angle between  $\vec{k}$  and  $\vec{B}_0$  at the source point outside the plasma. This should not be confused with the angle  $\theta$  at the cutoff layer, which is zero for maximum conversion.

In fig. 3.7 the solution of eq.(20) is plotted for angles  $\theta_{ins}$  near the optimum insertion angle  $\theta_{opt}$ . Here  $Y=0.9$  and  $(n_y^2, Y)$  coordinates are used. The O-mode branch is connected to the SX-mode in any case. But for the optimum incidence angle, the O-SX curve touches the  $n_y^2=0$  horizontal line and conversion from O to SX-mode is maximal. The O-mode propagates to the cutoff layer where it is completely converted into an X-mode, having the same direction  $\vec{k}$  and polarization as the incoming O-mode. At the point of conversion, both waves coincide and are indistinguishable. The polarization of both modes is left hand circular and  $\vec{k}$  is parallel to  $\vec{B}_0$ .

Waves with an angle of incidence slightly different from optimal are also partly converted into SX-modes due to tunneling through the evanescent region. The conversion efficiency is given by Mjølhus [40],

$$\tau_{O-SX} = \exp\left\{-\pi k_0 L_n \sqrt{\frac{Y}{2}} \left[2(1+Y)(n_{z_{opt}} - n_z)^2 + (n_x)^2\right]\right\}; \quad (25)$$

Here the dependence of the coupling coefficient is given as a function of the characteristic density scale length  $L_n$  at the point of conversion and the wavenumber of the incident wave in vacuum  $k_0$ . Additionally, the dependence of the efficiency on poloidally directed  $\vec{n}$  component  $n_x$  is included in this formula.

Using the Mjølhus formula a matrix can be calculated, which contain the efficiency of the O-SX coupling dependence on the  $\vec{n}$  direction. This matrix is plotted in fig. 3.8 for the spherical coordinates  $(\Theta, \Phi)$  shown in the fig. 3.9. Equation (25) may

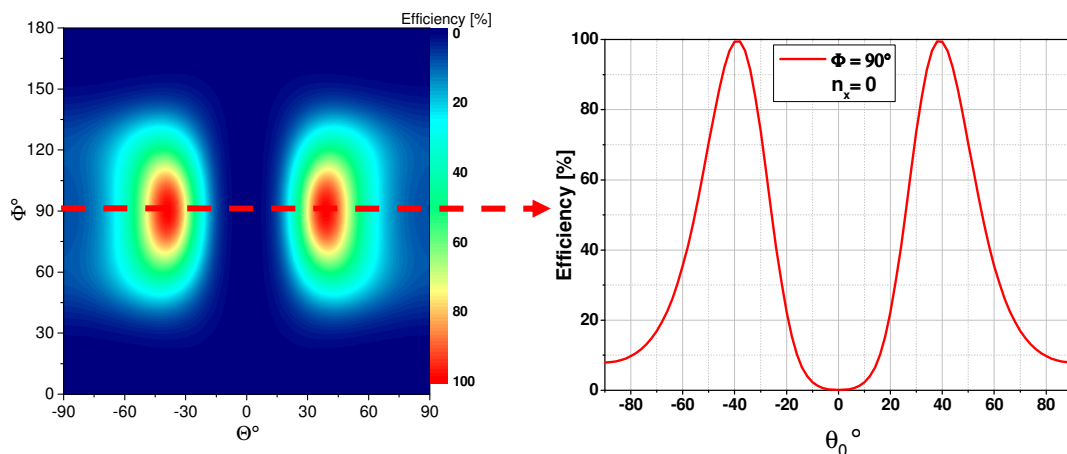


Fig.3.8. Matrix of O-SX conversion efficiency (left). Efficiency of O- SX conversion for changing insertion angle in horizontal plane of torus

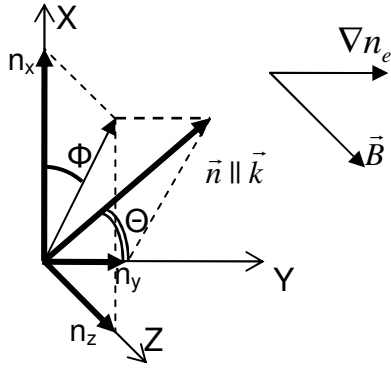


Fig.3.9. Coordinate system used for the acceptance matrix and antenna pattern plots.

be written in this coordinates if the  $n_x = \sin(\Theta)\cos(\Phi)$  and  $n_z = \sin(\Theta)\sin(\Phi)$  are applied. A calculation was made for  $Y = 0.65$ , which corresponds to typical operation regime of WEGA. The obtained matrix will be later used in section 5.2.3 for the efficiency estimates of the O-SX coupling efficiency for different antenna types.

Also in fig. 3.8 the dependence of the efficiency from  $\Theta$  plotted when  $\Phi$  equal zero or that is the same  $n_x$  equal zero. This situation corresponds to launching the wave with different angle to external magnetic field lines in the slab that is discussed before (fig. 3.6). Here it clearly seen that the angle  $\theta_0^{15}$  of wave launch optimal for O-SX conversion is  $\approx 40^\circ$ .

### 3.5. SX-B conversion

#### 3.5.1. Direct SX to B conversion

Extraordinary waves propagating obliquely to the electron density gradient always have some longitudinal component due to the motion of electrons in the electric field of the wave [42]. For a finite Larmor radius, electron movement is possible in the direction perpendicular to the external magnetic field  $\vec{B}_0$ . If the density gradient is perpendicular to the external magnetic field, a group of electrons moves to regions of higher (or lower) density due to interaction with the wave  $E$ -field. The local perturbation of electron density results in charge separation directed parallel to the density gradient. Thus, the wave does not remain purely electromagnetic and must have an electrostatic component, it can be shown that the SX-mode becomes almost completely longitudinal at the UHR [41].

An EM wave is deflected by cutoff regions with lower refractive index and deflected towards resonant regions with higher refractive index. The SX-mode is deflected by the L-cutoff to the UHR layer. Therefore, the SX-mode, initially

<sup>15</sup> Angle between the  $\vec{k}$  and the perpendicular direction to  $\vec{B}_0$  at the HF source point. ( $\theta_0 = 90^\circ - \theta_{ms}$ )

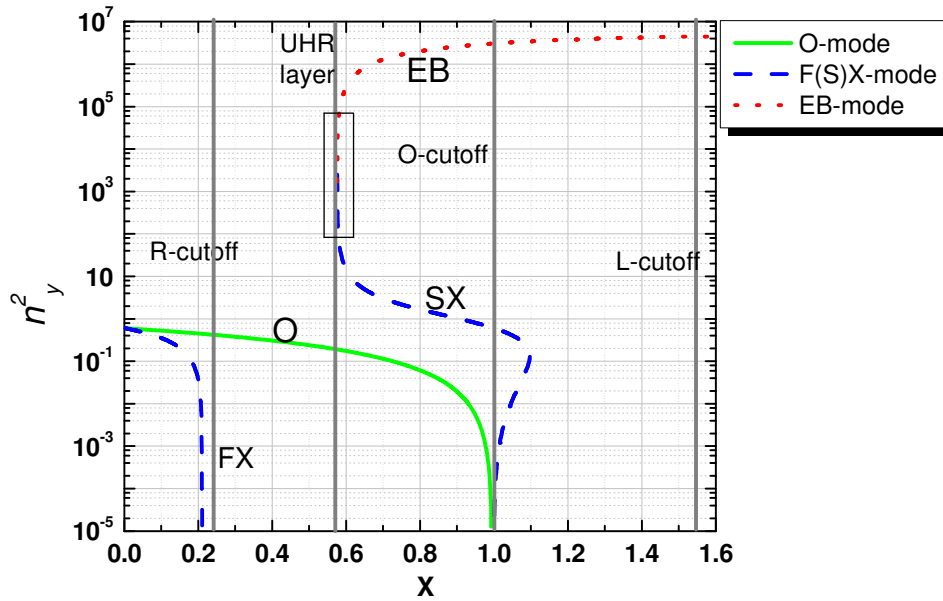


Fig.3.10. The hot plasma dispersion relation for optimal incidence angle

propagating in the direction of the L-cutoff layer turns back and reaches the Upper Hybrid Resonance (UHR) layer. Note the SX-mode is not affected by the O-cutoff.

The amplitude of the wave increases and its wavelength decreases ( $E_0 \rightarrow \infty$ ,  $k_{\perp} \rightarrow \infty$ ) when the wave propagates into the resonance region. This corresponds to the SX branch near the UHR layer shown in fig. 3.10. The EB branch shows the solution for the Electron Bernstein electrostatic mode. Near the UH resonance region marked with the rectangle the SX-mode phase velocity  $\omega/k_{\perp}$  decreases and the wavelength becomes comparable with the Larmor radius. Here the SX-mode coincides with the EB-mode, and the conversion of SX-modes to Bernstein waves takes place. The  $k_{\parallel}$  component does not take part in the wave-particle energy exchange and remains unchanged in this transition process.

### 3.5.2. SX to FX tunneling effect on conversion efficiency

A competitive process to SX-B conversion is the SX-FX conversion. It occurs if the R-cutoff layer is close to the UHR layer. The FX-mode exists only below the R-cutoff and the SX-mode exists only above the UHR. A part of the SX-mode may tunnel to the FX-mode [44] and this tunneling defines the efficiency of the SX-B conversion. The efficiency of the SX-FX conversion process is given by.

$$\tau_{SX-FX} = \exp\left\{-\pi k_0 L_n Y^2 \sqrt{(\omega_{UH}/\omega_{ce} - 1)/X}\right\} \quad (26)$$

The tunneling process is only source of losses in SX-B conversion process, if the collisions are neglected. Thus, total efficiency of OXB conversion is from eq.25 and 26,

$$\tau_{O-SX-B} = \tau_{O-SX} (1 - \tau_{SX-FX}). \quad (27)$$

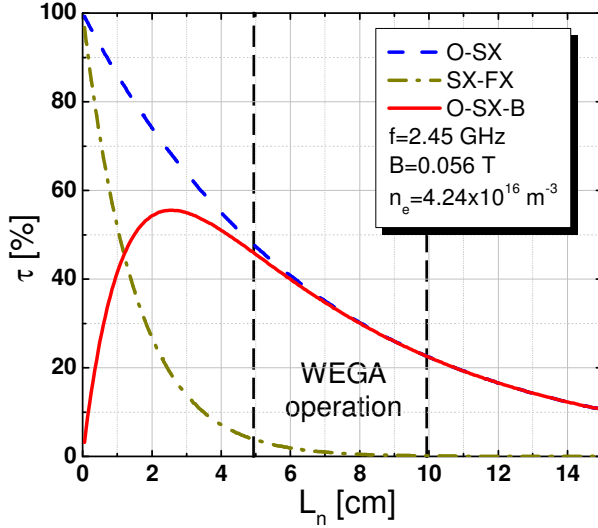


Fig.3.11. O-SX, SX-FX, total OXB efficiency calculated for standard WEGA experiment conditions

corresponds to  $\theta_0 \approx 55^\circ$ . This angle is chosen because the heating antenna pattern used for the heating in the WEGA has the maximum emission with this angle between  $\vec{k}$  and  $\vec{B}_0$ .

The values of density gradient length between 5 and 10 cm correspond to the typical experiment conditions in the WEGA plasma. In this range, the tunneling efficiency is always below 4%. The total efficiency of OXB conversion is mostly defined by the O-SX efficiency. However the collisions can not be neglected in WEGA, thus it will be an additional source of losses during the SX-B conversion. Moreover, density fluctuations at the cutoff are also not included. These deteriorate the O-SX conversion efficiency. The maximal value of O-SX-B conversion  $\tau \approx 55\%$  shown in fig.3.11 is overestimated due to this reason.

In opposite to O-SX conversion efficiency, SX-FX efficiency does not depend on the insertion angle of the wave. Only the parameter, which affects the efficiency for given magnetic field and frequency, is the characteristic density length.

The dependence of efficiency values is calculated using eq.25,26,27 for characteristic density length at the WEGA typical magnetic field and heating frequency of 2.45 GHz is shown in fig. 3.11. The  $n_z$  in eq.25 is set to 0.85 which



### **3.6. Summary of theory**

It was shown that to obtain the EB wave in the center of WEGA plasma the OXB mode conversion is needed. This process consists of two steps and total efficiency of it is defined by the efficiency on each step separately. The efficiency of O-SX conversion can be varied by changing the insertion angle of heating wave, while the SX-B process efficiency defined by density gradient length near UHR layer and, to some extent, by the edge temperature, which affects the collisional losses.

However, this result was obtained in WKB approximation. To investigate the OXB conversion process in the WEGA full wave calculations of EM waves distribution in plasma should be performed. The process of these calculations is described in section 4.2.

---



## 4. Numerical simulations of the OXB process

This chapter will discuss the numerical simulations of OXB process. First a few examples of ray tracing calculations are given in section 4.1. In section 4.2 the full wave code is described. This section is divided into several sections each dealing with different cases solved with the full wave code (sections 4.2.2-4.2.5). The last section 4.3 discusses the results obtained from the calculations for heating in the WEGA stellarator.

### 4.1. OXB in the ray tracing approximation

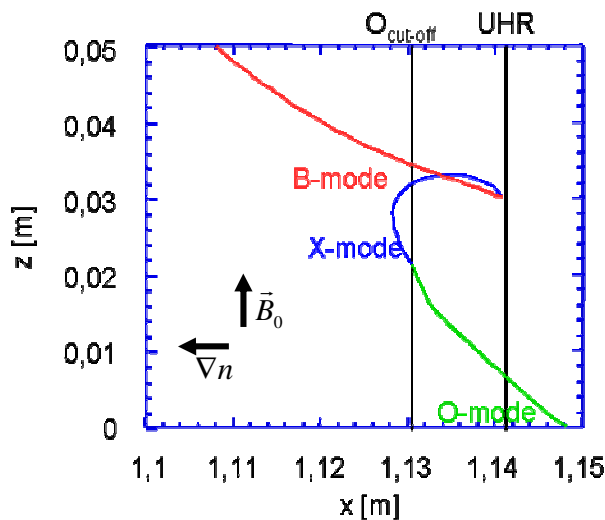


Fig.4.1. Ray tracing calculation of OXB mode conversion (bottom to top) or BXO mode conversion (top to bottom) [14].

$$L_B, L_T, L_n \gg \lambda, \quad (28)$$

where the subscripts B, T and n correspond to external magnetic field, temperature and density respectively.

Fig. 4.1 [21] shows the ray trace trajectory of a beam, which undergoes OXB mode conversion. Here the O-mode is launched from outside the plasma couples with the SX-mode at the O-cutoff layer. The SX-mode then propagates back to the UHR

In the stellarator or tokamak plasma, the time variation of plasma parameters may be neglected and Fourier-transform in time may be applied without loss of generality. For a weakly inhomogeneous plasma, the Wentzel-Kramer-Brillouin (WKB) approximation may be used to derive ray tracing equations that describe the propagation of waves inside the plasma.

The condition of weak inhomogeneity requires the characteristic gradient lengths scales to obey,

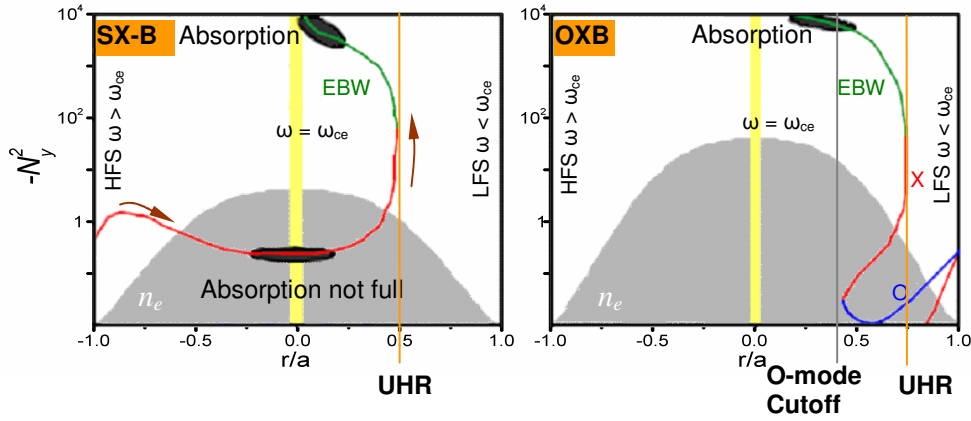


Fig.4.2. Ray tracing calculations with the TRUBA code for the TJ-II stellarator. The SX-B scheme is shown on the left, while the OXB scheme is shown on the right. (adopted from [48])

layer where it is resonantly converted into the EBW. The EBW propagates into the center of the plasma where it is absorbed at the Electron cyclotron frequency or its harmonics. Due to time reversibility, the figure also describes the BXO process [32].

Ray tracing calculations were also used to describe the heating mechanism in the TJ-II stellarator. The SX-B and OXB heating schemes are shown in fig. 4.2. The ray tracing code TRUBA was developed to study the properties of conversion, propagation and absorption of EC waves [47]. The heating frequency is 28 GHz. In fig. 4.2  $N_{\perp} \equiv n_y$  and the electron density profiles are plotted versus the radial position. The SX-B case is shown on the left side of fig. 4.2 corresponds to launching an X-mode from the high field side. It propagates to the center of the plasma where it is partly absorbed. The remaining wave reaches the UHR layer, where it converts into an EB-wave. This is finally totally absorbed in the  $\omega = \omega_{ce}$  region. The OXB case shown in the right of fig. 4.2 shows the behaviour of an O-mode launched from the low field side (LFS) with an optimum  $N_{\parallel} \equiv N_{\parallel, opt}$  or optimum launch angle. In this case, the OXB conversion process occurs totally.

## 4.2. OXB in full wave calculations

### 4.2.1. Full wave code

Ray tracing calculations are not applicable to the large wavelength used in the WEGA stellarator as eq.(28) is not fulfilled. Therefore, the full system of Maxwell's equations, including the plasma current response term must be solved [44]. A program, which does this was developed by E. Holzhauser (University Stuttgart) and adopted to

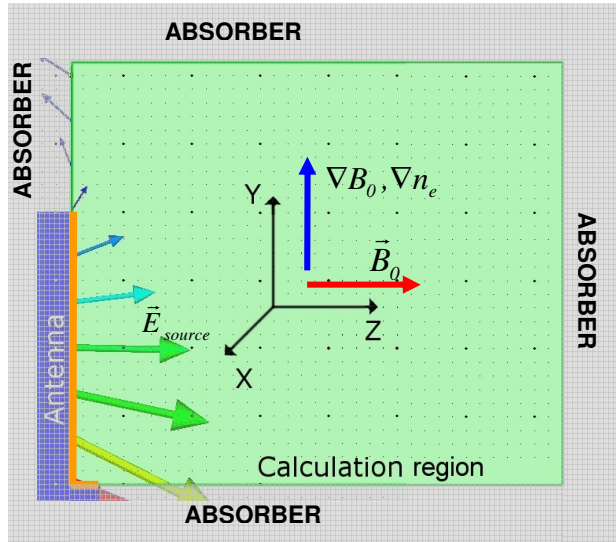


Fig.4.4. Coordinate system used in the full wave calculations.

profiles of density and magnetic field are needed for the calculations. The external magnetic field  $\vec{B}_0$  is taken as parallel to the Z-axis. The electron density and external magnetic field gradients are parallel to the Y-axis. The toroidal curvature of the magnetic field lines is not taken into account.

the WEGA situation. The code is written in the C language and is described in detail in Appendix C. It uses the cold magnetized plasma model for the time dependent calculations in a two dimensional slab. Thus, only O-SX conversion is simulated. SX-B conversion is simulated by the numerical viscosity damping.

Maxwell's equations are solved in 2D geometry in the YZ-plane. This corresponds to the horizontal plane of the WEGA torus near the heating antenna as shown in fig. 4.3. Radial

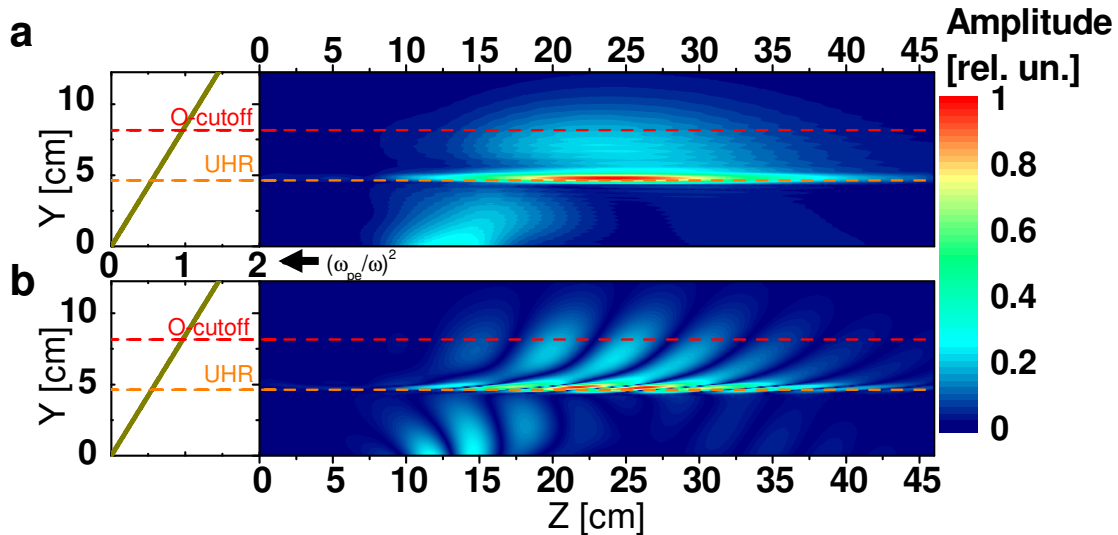


Fig. 4.3. Radial component of electric field  $E_r$ ,  $k_0 L_n \approx 2$  (low frequency case)

a) time averaged  $E_r$  b)  $E_r$  snapshot

Launched wave has its  $k$ -vector  $45^\circ$  to the external magnetic field. The density profile is linear. Zero value of the electron density is at the bottom

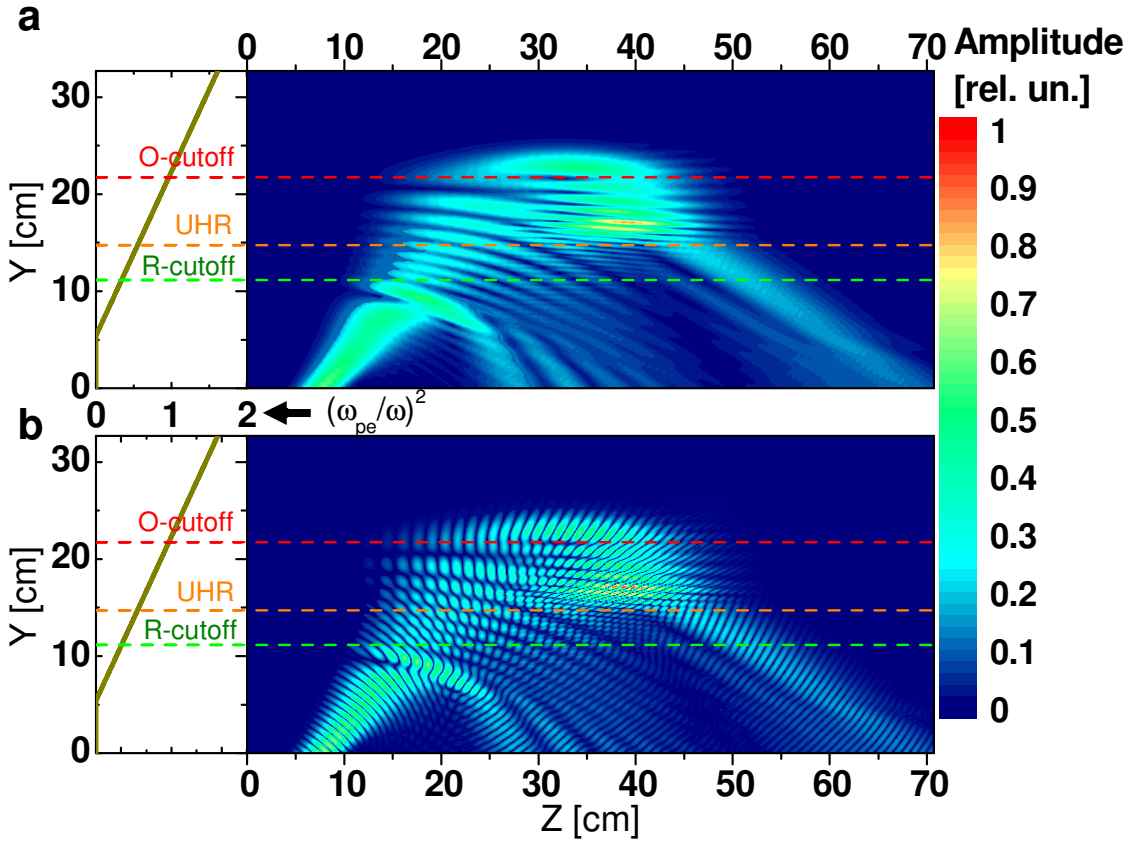


Fig. 4.5. Like fig.4.4 but with  $k_0 L_n \approx 12$  (high frequency case)

Typical results of the 2D calculations in cold plasma are presented in fig. 4.4, 4.5. The radial component of the  $E$ -field of the wave  $E_r$ , is plotted over the calculation region. Here a linear density profile is used and the results for two cases of low (fig. 4.4) and high (fig. 4.5) frequencies are plotted. The “a” plots show the averaged value over the period of oscillation while “b” plots show the  $E_r$  distribution at a fixed moment in time.

The low frequency case is closer to the situation in WEGA in terms of the heating wavelength and the characteristic density gradient length. In both cases, the source is a Gaussian beam with initial  $\vec{k}$  at an angle of  $45^\circ$  to the external magnetic field. The UHR layer and the cutoff layer are marked as horizontal lines over the density profile. On the high frequency plots, the R-cutoff position is marked. In section 4.2.5 it is shown that part of the HF power is reflected from the R-cutoff if the polarization of incident wave is not optimal.

In all the plots, the  $E_y$  amplitude rises in the UHR region. This maximum shows the existence of resonance at the UHR layer, even for low frequency heating as in WEGA. In these calculations, the temperature term is not included and the absorption of the wave near UHR layer is simulated by numerical viscosity. Therefore, all waves that are resonant on the UHR layer are absorbed there.

#### 4.2.2. O-SX conversion efficiency

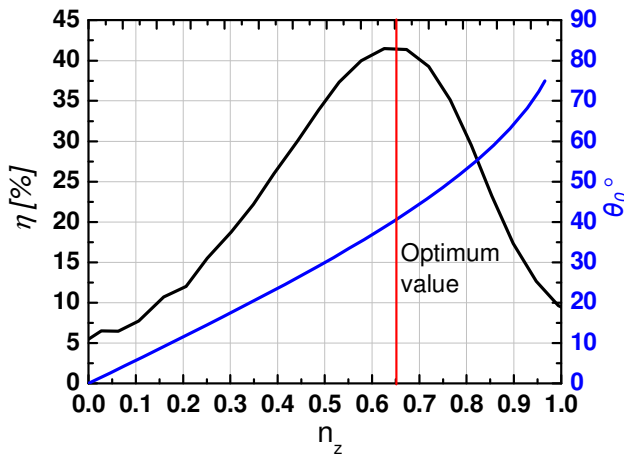


Fig.4.6. Dependence of the O-SX mode conversion efficiency on the launch angle  $\theta_0$ . The blue curve shows the dependence of  $\theta_0$  on  $n_z$  component of  $\vec{n}$ .

$P_{ref}$ . Consequently, the O-SX mode conversion efficiency can be quantified as the transmitted power fraction.

$$\eta = \frac{P_{in} - P_{ref}}{P_{in}} \quad (29)$$

More details on how this is treated in the code are given in Appendix C.

The efficiency is usually between 10 and 30%. This low efficiency is due to the polarization of the heating wave is not optimized for maximum efficiency, as it was in [43], in more details it is described in section 4.2.6. In addition, the efficiency also decreased due to the long heating radiation wavelength compared to the characteristic density gradient length  $L_n$  (see fig. 3.11). A large fraction of the power leaves the calculation region after reflection from the cutoff layer. For higher frequency and optimized elliptical polarization, the efficiency may reach 60 to 70% of the inserted power. In the real plasma, also the density fluctuations exist. On the cutoff layer it leads

to the total O-SX conversion efficiency degradation due to the non-optimal slopes at the turbulent cutoff layer [21].

The dependence of the efficiency on the launch angle was investigated with the full wave code. In fig. 4.6 the dependence of the efficiency on  $n_z$  is shown. Here the efficiency is calculated for a linear electron density profile and  $k_0 L_n \approx 2$ . This is close to the low frequency case in fig. 4.4. The external magnetic field in this calculation is  $0.65 \times B_{res}$ . This magnetic field value was chosen, because maximum  $T_e$  and  $n_e$  were obtained in the WEGA plasma for this value of the magnetic field (see. section 2.4). The polarization of the HF source is linear and in the plane of incidence.

The maximum of efficiency is obtained for  $n_z \approx 0.65$ . That corresponds to  $40^\circ$  between the  $\vec{k}$  and perpendicular to  $\vec{B}_0$ .

### 4.2.3. Bernstein mode in 1D

In order to show the EBW generation finite temperature correction must be included. In addition, the EBW require a much finer calculation mesh, which would lead to an impracticable computation time. The 2D code computation time to calculate

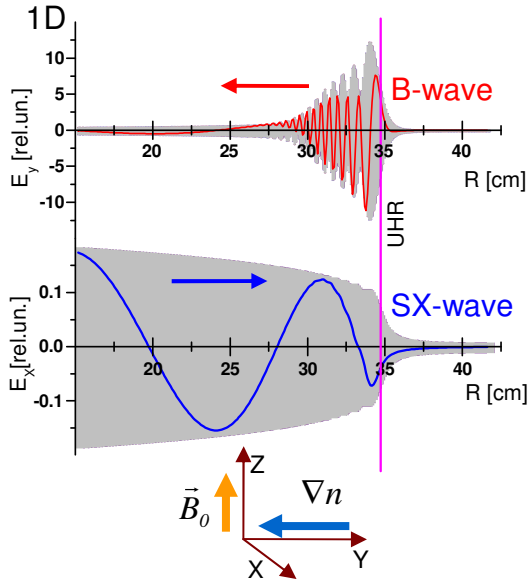


Fig.4.7. Example of an one-dimensional calculation. An SX-mode coming from the high field side (plasma side, left) to the UHR layer is coupled to the B-mode, which propagates to the plasma centre.

the rise of the B-mode is very large. Therefore, one-dimensional (1D) calculations have been used to show the SX-mode to B-mode conversion at the UHR layer.

According to the dispersion relation for the SX-mode (eq.20 fig. 3.7) and the EBW-mode near the UHR layer (eq.18 fig. 3.3) the component of  $\vec{k}$  perpendicular to magnetic field is much larger than the parallel one  $k_\perp \gg k_\parallel$ . This leads to propagation nearly perpendicular to  $\vec{B}_0$ .

This justifies, 1D calculations of SX-B conversion perpendicular to external magnetic field.

The electron temperature is taken into account in these calculations [44]. In



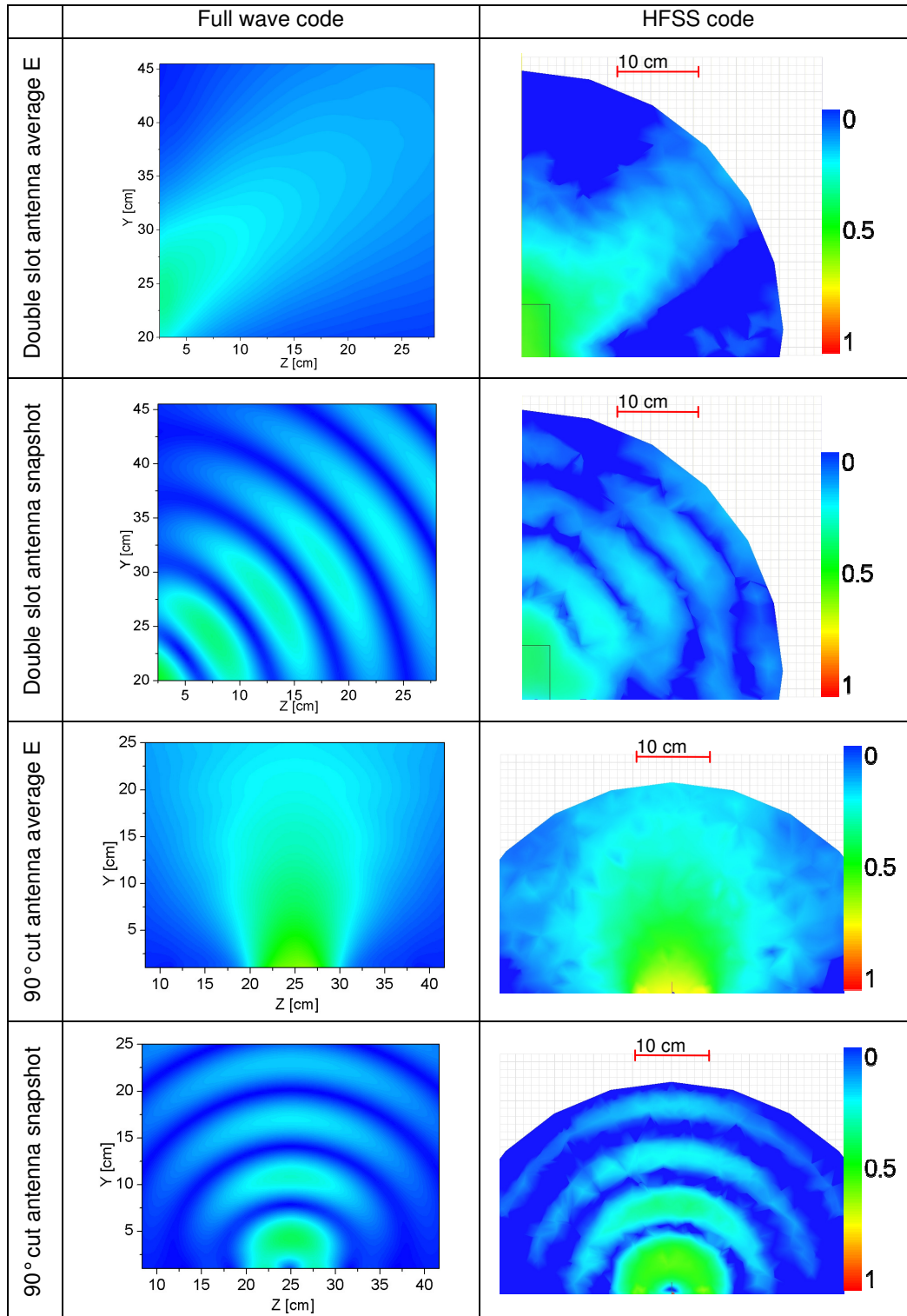


Fig.4.8. Vacuum calculations of the full-wave code compared with HFSS code for 90°cut and Double Slot antennas. The E-field value is plotted in the form of colour contours normalised to its maximum value.

the bottom of fig. 4.7, the transverse component of the electric field is plotted. It represents the SX-mode. On the top of the picture, the longitudinal component of the  $E$ -field, which represents the EB-mode, is shown.

The SX-mode is coming to the UHR layer from the plasma side, couples with the short wavelength of the B-mode. The B-mode then propagates back into the plasma. In this calculation, the B-mode is absorbed with artificial damping. In a real plasma, the B-mode propagates to the cyclotron resonance layer and is absorbed there by the electrons.

The 1D calculation was used only to demonstrate the SX-B mode conversion and was not used in the heating optimization process.

#### 4.2.4. Vacuum calculations

To choose the best HF source configuration for the calculations, the antenna pattern calculated in the vacuum by full wave code should be compared with one calculated by the HFSS code. Fig. 4.8 shows the  $E$ -field distribution calculated by the full wave code in vacuum for two cases of incidence angle (left column). These results are compared with calculations made by HFSS code for two types of antenna used in WEGA (right column). Although the different calculation methods were used by the HFSS and the full wave codes, the calculated patterns are quite similar. Therefore, sources shown in the left column could be used for the full wave calculations in plasma.

#### 4.2.5. Perpendicular X-mode launch

In section 2.3.3 it was mentioned that the heating with perpendicularly launched O- and X-mode is inefficient because of reflection from cutoff layers. This may be also checked using full wave calculations. To simulate this heating scenario numerically the HF source was chosen shown in fig. 4.8 as  $90^\circ$  antenna. This antenna configuration was used in the first WEGA experiments.

Two calculations were performed, one with the X-polarized source wave, another with O-polarized. Real WEGA density profile measured with Langmuir probes was fitted and interpolated for using in these calculations (for density measurements see chapter 7.1.1). The results of these calculations are shown in fig. 4.9.

The reason for low efficiency of heating by O-mode with perpendicular launch is high reflection from the O-mode cutoff layer. The maximum of the averaged  $E$  field distribution between the cutoff layer and bottom source plane indicate that there exists a standing wave. The standing wave is a result of incoming and reflected wave

---

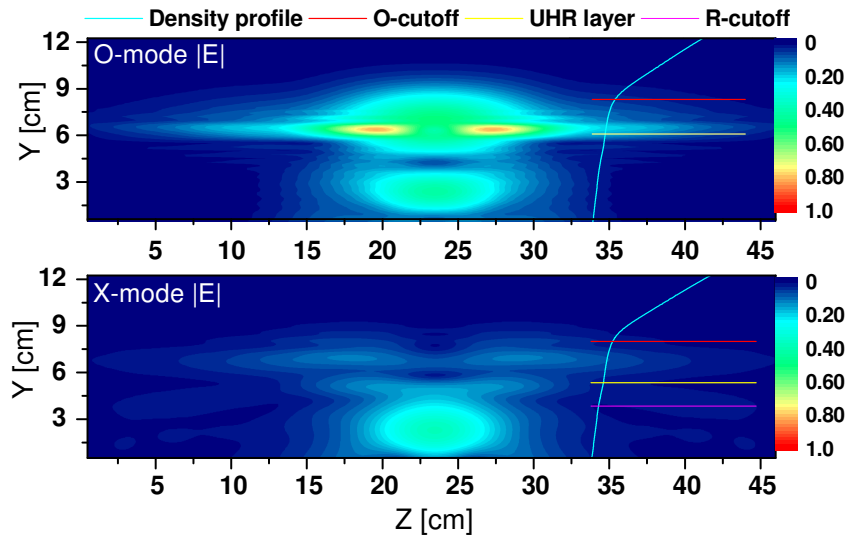


Fig.4.9. Full wave calculations results for O- and X-mode launched perpendicularly to external magnetic field. Averaged  $E$  field distribution is shown.

interference. Only a small part of the power reaches the UHR layer after conversion to SX-mode, which is indicated by two maximums localized near the UHR layer position.

In the case of X-mode perpendicular launch, the standing wave pattern is also observed. However, the reflection here is mostly from R-cutoff layer and almost no power reaches the UHR layer. The resonant maxima of the  $E$ -field amplitude on the UHR layer are absent. The calculation with X-mode polarized source also proves the correctness of the assumption made in section 3.5, about SX to FX (or FX to SX) wave tunneling: a very small portion of HF power reaches the O-cutoff layer due to tunneling for this steep density profile.

The calculated efficiency is very low for both cases. For O-mode perpendicular launch 5.2% of power is absorbed, for the X-mode only 3%.

#### 4.2.6. Polarization of the source in full wave calculations

The maximum O-SX conversion is expected in pure O-mode launch. The optimization of the source polarization is required to get pure O-mode, which is not reflected by the R-cutoff layer. In fig. 4.10 the results of the calculation for the high frequency case are shown together with the density profile used for these calculations. Here only the region of the R-cutoff layer is calculated. All power that passes through this region is absorbed at the top plane. Fig. 4.11 shows the efficiency of the transition

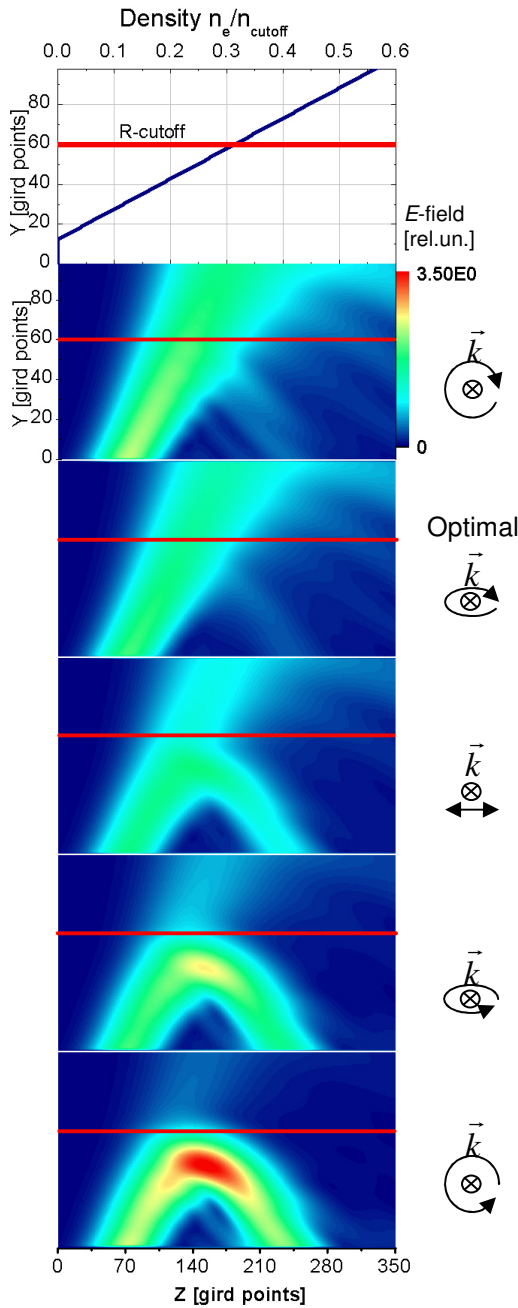


Fig.4.10. Transmission of the HF beam through the R-cutoff layer calculated for various source polarizations. In the plot marked as “Optimal” the polarization is such that:

$$\frac{E_x}{\sqrt{E_y^2 + E_z^2}} = 0.33$$

through the R-cutoff as a function of source polarization. For optimal elliptical polarization of the source, the transition through the R-cutoff layer is maximal and amounts to about 87%.

The transmission efficiency can not reach 100% because the antenna emits a wide  $\vec{k}$  spectrum. The optimal polarization value depends on the inclination of  $\vec{k}$  to  $\vec{B}_0$ . Polarization is optimized for the central  $\vec{k}$  direction in which maximum power is emitted. Directions of  $\vec{k}$  that deviate from the optimal one have non-optimal conditions for transition through the R-cutoff layer. Thus, the transition efficiency integrated over the whole beam width can not reach 100%.

The result close to the full wave calculations for O-mode polarization with the same angle of incidence was obtained analytically. In this calculation the results obtained by H.Igami, M.Ushida [43] are used. In their work, the optimal polarization of injected wave was found analytically by using the scattering matrix between vacuum TEM waves and EB waves. The injected wave was discussed there as the sum of the O- and X-mode launched with the same angle. The total conversion efficiency was found as a sum of efficiencies of two modes. Also in this work, the analytical expression for pure O-mode for oblique

launch is obtained by taking the vacuum limit of  $\omega_p/\omega \rightarrow 0$  in the wave equation for homogeneous plasma.

$$\vec{E}_o = \left[ \left( 2N_{\parallel} \right) \vec{e}_1 + i \left( \left( 1 - N_{\parallel}^2 \right) \left( \frac{\omega_{ec}}{\omega} \right) - \sqrt{\left( 1 - N_{\parallel}^2 \right)^2 \left( \frac{\omega_{ec}}{\omega} \right)^2 + 4N_{\parallel}^2} \right) \vec{e}_2 \right] \quad (30)$$

$$\times \left[ 8N_{\parallel}^2 + 2 \left( 1 - N_{\parallel}^2 \right)^2 \left( \frac{\omega_{ec}}{\omega} \right)^2 - 2 \left( 1 - N_{\parallel}^2 \right) \left( \frac{\omega_{ec}}{\omega} \right) \sqrt{\left( 1 - N_{\parallel}^2 \right)^2 \left( \frac{\omega_{ec}}{\omega} \right)^2 + 4N_{\parallel}^2} \right]^{-1/2}$$

Where  $N_{\parallel}$  is the component of refractive index parallel to the external magnetic field  $\vec{B}_0$ . The  $\vec{e}_1$  and the  $\vec{e}_2$  components represent the part of wave electric field polarized in the plane of incidence and perpendicular to the plane of incidence respectively.

By substituting in eq.30 the same value of  $N_{\parallel}$  used in the full wave calculations, the vertical mark in fig. 4.11 is obtained. It is in a good agreement with the transmission efficiency calculated numerically.

The power reflected from the R-cutoff layer can not take part in the O-SX conversion process. Therefore, not optimal polarization decreases the total efficiency of the OXB conversion.

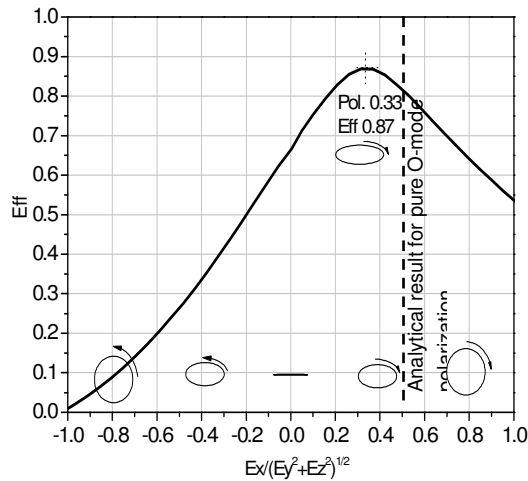


Fig.4.11. Efficiency of transmission through the R-cutoff layer as a function of source polarization.

Although this effect was shown for the high frequency case, the same effect occurs at low frequency. In this case, the distance between the R-cutoff and O-cutoff layers is much shorter compared to the heating wavelength. Reflected from the R-cutoff wave can not be easily observed on the background of the wave reflected from O-cutoff.

The optimization of the heating wave polarization was not performed in this work due to technical limitation, as the circular polarization can not be adjusted for both antenna pattern lobes of the double slot antenna (see chapter 5).

---

### **4.3. Conclusion from the preliminary full-wave calculations**

The theory described above suggests that mode conversion can be used on WEGA to improve the efficiency of ECR heating. The main outcome of the preliminary full wave calculations is the determination of the optimal direction of  $\vec{k}$  for a wave inserted for maximal O-SX conversion efficiency.

The optimal angle between  $\vec{k}$  and the perpendicular to external magnetic field  $\vec{B}_0$  for the O-SX conversion process is near  $40^\circ$ . The antenna shape should be designed to launch as much power as possible with this  $\vec{k}$  direction. The process of antenna optimization in terms of incidence angle and the results of this optimization are described in chapter 5. The possibility of antenna polarization optimization is also shown using the full wave calculations. However, it was not done in the WEGA because of technical restrictions.

Another important application of the full wave calculations is to simulate the HF wave processes in the WEGA plasma. The distribution of electromagnetic fields calculated with this code can be compared with the HF wave distribution in WEGA plasma. For such comparisons, information about the EM field amplitude and phase distribution in the vicinity of the heating antenna is required. In addition, the density profiles in this region should also be known, to allow realistic modelling and interpretation of the full wave processes in WEGA. Thus, simultaneous measurements with high frequency and Langmuir probes near the heating antenna are required. In chapter 6 such a measurement system is described. Chapter 7 presents the results of the measurements.

---

## 5. ECR Heating antenna shape optimization

This chapter is devoted to the ECR heating antenna development and to results of its testing in the WEGA. In section 5.1 the antenna shape evolution steps are presented (section 5.1.2). The results of the calculations are presented in section 5.1.3 and compared with the results of emission pattern measurement in section 5.1.4.

In section 5.2 the plasma parameters obtained from various diagnostics are compared for different heating antenna types. Here the results of fast Langmuir probes (section 5.2.1), bolometric measurements, and colorimetric measurements (section 5.2.2) are presented. Results of numerical estimates of O-SX conversion efficiency using Mjølhus formula compared are with full wave calculations in section 5.2.3.

### 5.1. Heating antenna development

#### 5.1.1. Heating antenna arrangement

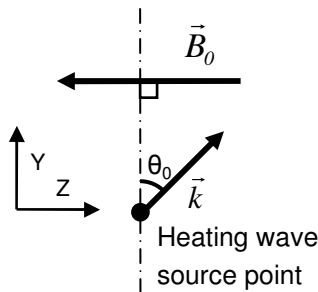


Fig.5.1. Direction of  $\vec{k}$  relative to the magnetic field

The heating wave is an O-mode wave launched in equatorial plane of torus from low field side. As launching antennas, specially shaped end of cylindrical  $H_{11}$  waveguide is used.

As mentioned in section 4.3, the heating antenna should be optimized in order to emit the heating power with optimal  $\vec{k}$  inclination with respect to the external magnetic field  $\vec{B}_0$ . This angle  $\theta_0$  is between the perpendicular line to the magnetic field line and the  $\vec{k}$  as shown in fig. 5.1

The ray tracing calculations [21] show that the optimal for O-SX conversion  $\theta_0$  is  $\approx 45^\circ$  for the 1<sup>st</sup> harmonic heating and  $\approx 35^\circ$  for the 2<sup>nd</sup> harmonic. The full wave calculations also show the value  $\approx 40^\circ$  for the first harmonic. Therefore, the heating antenna should have the  $\vec{k}$  inclination of emitted wave  $\theta_0 \approx 40^\circ$ .

In general, the entire heating antenna arrangement should be tilted to launch the HF beam in proper direction. However, this is impossible in the WEGA particular case.

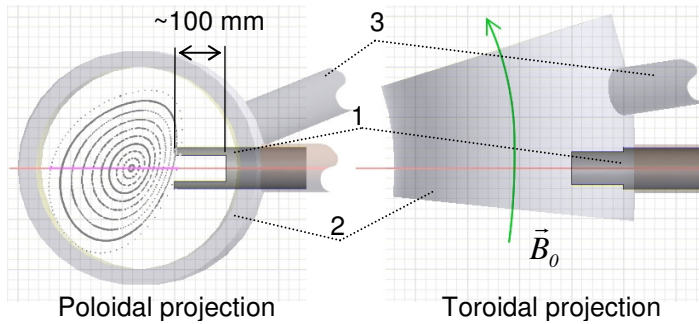


Fig.5.2. Slot antenna (see 5.1.2) arrangement in WEGA:  
 1 - slot antenna, 2 – vacuum chamber, 3 – Port used for HF  
 measurements (see 6.2)

The antenna should not touch the plasma because it may be damaged during the long time high power experiments. The distance from the antenna port to the LCFS is determined by the plasma size and hence from the rotational transform  $l$ , 100 mm is valid for  $l/2\pi \sim 0.2$ . Therefore, the length of the antenna should not be more than  $\sim 100$  mm as shown in fig. 5.2

Taking into account these restrictions the special shaping of the antenna end was proposed.

### 5.1.2. Antenna design

Initially, a cylindrical  $TE_{11}$  waveguide was used as an antenna for the heating of WEGA plasma as shown in fig. 5.3a. However, a low heating efficiency was observed in these experiments. The electron density and the temperature profiles measured with the fast reciprocating Langmuir probes were hollow with the maximum located outside of the LCFS region. Maximum density value was  $n_e \approx 1.33 \times n_{ecutoff}$ , electron temperature  $T_e \approx 6$  eV, only the edge heating observed. The heating is assumed to be due to the multiple reflections of the heating wave between the cutoff layer and the metallic chamber wall.

As a first step of antenna shape modification the waveguide was cut under an angle of  $45^\circ$  to launch power oblique to the external magnetic field vector. The  $45^\circ$  cut antenna is shown in fig. 5.3b In the experiments with this antenna configuration, the density profile hollowness decreased. Profiles become even flat. The density value increased up to  $n_e \approx 10 \times n_{ecutoff}$ . The temperature profile stays hollow with the maximum

The antenna is fixed inside the vacuum camera port and the port axis direction is fixed. Additionally, the maximum inner diameter of the antenna is limited to 83 mm. by the port diameter. The length of the antenna is limited by the distance between the chamber wall and the LCFS position. The end of the



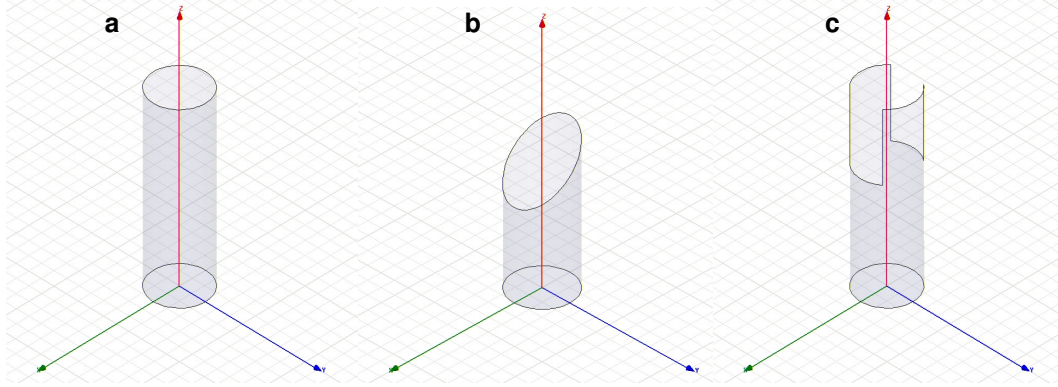


Fig. 5.3. Antenna evolution steps:

a) The  $TE_{11}$  cylindrical waveguide  $90^\circ$  cut. b)  $45^\circ$  cut antenna c) Double slot antenna.

Polarization of the  $E$  field parallel to the  $X$ -axis (green)

at the LCFS. It is assumed that part of the emitted power is absorbed inside of the plasma via the OXB mode conversion process (see chapter 3).

In a second step in the antenna modification process, a special double slot antenna shape was developed (fig. 5.3c).

The double slot antenna design is based on the geometrical-optic approximation [26]. In this approximation, any wave in cylindrical waveguide may be represented as superposition of the plane waves propagation at the Brillouin angle to the waveguide axis.

WEGA heating system has only  $H_{11}$  ( $TE_{11}$ ) mode in the waveguide. This is the only existing mode for 2.45 GHz frequency in waveguide with radius  $R_{wg} = 41.5$  mm. All other modes have the critical radius of the waveguide larger than our waveguide radius. For example, the next mode in the sense of critical wavelength is  $E_{01}$  it has the critical waveguide radius  $\approx 46.8$  mm. This mode can not propagate in the waveguide as well as all other modes different from  $H_{11}$ .

According to a quasi-optical representation in order to emit all HF power through the slot in the cylindrical waveguide, the length of this slot for should be longer than Brillouin length  $L_B$ . For  $H_{11}$  mode this length is given by,

$$L_B = 2 \frac{R_{wg}^2}{R_{cr}} \sqrt{1 - \left(\frac{\lambda}{2\pi R_{cr}}\right)^2} \sqrt{1 - \left(\frac{R_{cr}}{R_{wg}}\right)^2} \frac{\pi}{\arccos\left(\frac{\lambda}{2\pi R_{cr}}\right)}, \quad (31)$$

$$R_{cr} = \frac{1.84\lambda}{2\pi}, \quad (32)$$

where  $R_{cr}$  is a radius of a cylindrical waveguide, which is critical for  $H_{11}$  mode with given wavelength  $\lambda$  [24].

In the case of the 2.45 GHz frequency this radius equal to  $R_{cr} = 35.9$  mm, the Brillouin length is  $L_B \approx 14.3$  cm.

The angular width of the slot is defined by the propagating mode type, for  $H_{11}$  mode  $\Delta \approx 114^\circ$ . The Brillouin angle is defined by,

$$\theta_B = \arcsin(R_{cr}/R_{wg}), \quad (33)$$

for the used waveguide radius and frequency is  $\theta_B = 57.5^\circ$ .

This result shows that if the slot has the length  $L_B = 14.3$  cm and  $\Delta = 114^\circ$  angular width, then all the power will be emitted through this slot with an angle between the  $\vec{k}$  and waveguide axis  $\approx 57.5^\circ$ .

As was mentioned in previous chapter, in WEGA the total length of antenna, and thus the slot length, is limited by the distance between vacuum chamber wall and plasma edge, to approximately 10 cm length. If the slot length is shorter than  $L_B$  then the angular width  $\Delta$  of the slot should be increased. It is necessary to avoid the emission of HF from the end of the waveguide with  $\vec{k}$  perpendicular to external magnetic field

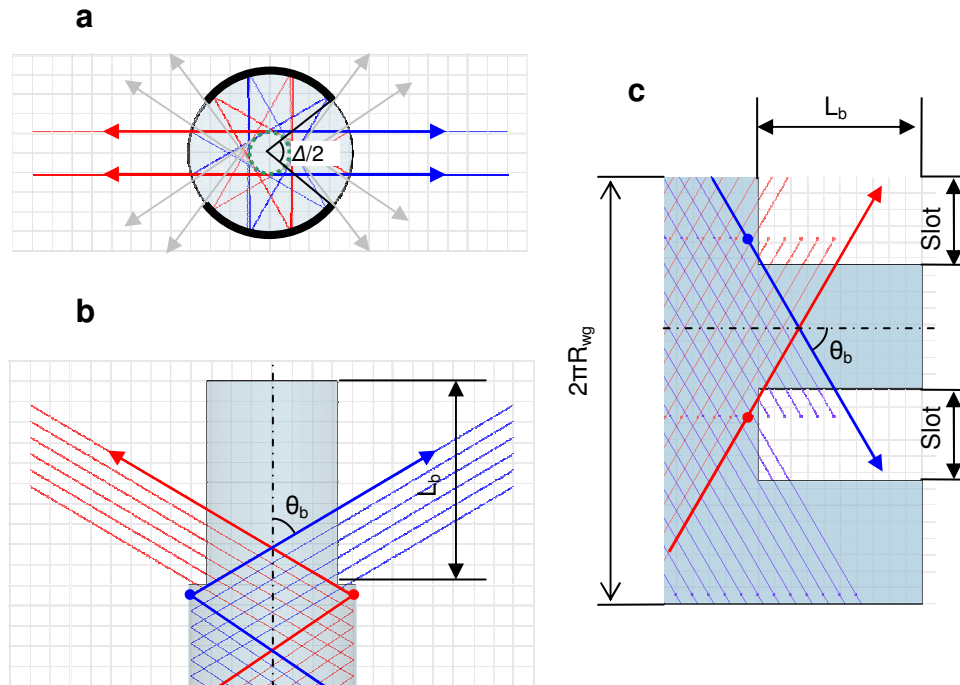


Fig.5.4. Quasi-optical representation of the double slot antenna.

a) top view b) side view c) unwrapped view

vector because the wave will not be accepted for O-SX conversion process. However, increasing the angular width leads to undesirable effect of increasing the HF beam width in poloidal direction, hence much power will be emitted not in equatorial plane of torus<sup>16</sup>.

To solve this problem the slot was divided in two equal slots of half angular width  $\Delta/2 \approx 57^\circ$  positioned opposite to each other as shown in fig. 5.3c. The result of this modification is HF emission pattern with two lobes of with  $\theta_0 \approx 57.5^\circ$ .

In fig. 5.4 the quasi-optical representation of the double slot antenna is shown in two projections, top (a) and side (b) view. The lines plotted in these pictures correspond to direction of plane waves propagation, which are a components of the  $H_{11}$  mode. The blue and red rays correspond to the components with different rotation direction around the waveguide axis. The points on these lines correspond to the places where the plane wave is reflected from the metallic waveguide wall.

In fig. 5.4c the antenna waveguide is shown unwrapped. Here the two slots of equal angular width are visible. The wave, in the points of reflections, which do not hit the waveguide wall, is emitted through the slots.

As a result, profile of electron density becomes flat or even peaked, maximum density value increased up to  $n_e \approx 20 \times n_{ecutoff}$ . The temperature of electrons is also increased up to  $T_e \approx 12$  eV.

The full wave calculations shows that angle  $\theta_0$  should be  $\approx 40^\circ$  so the launching angle for the double slot antenna is not optimal. However, the calculated efficiency of O-SX conversion by the full wave code is noticeable higher for this entrance angle. In order to bring the angle closer to optimal entrance the Brillouin angle should be changed. This requires a change of the antenna radius. For obtaining the Brillouin angle  $40^\circ$  the radius of the antenna waveguide should be equal 52.5 mm. Unfortunately, it is not possible in WEGA because of the inner antenna diameter limit of 83 mm.

### 5.1.3. Antenna emission pattern calculation

At first, the antenna design was investigated numerically, and then the antenna pattern was investigated in the lab. The obtained results were compared, and the conclusions about the antenna applicability were made.

---

<sup>16</sup> In fig.3.8 large poloidal angle corresponds to large deviation from  $\varphi=0$  line where maximal values of conversion efficiency are located.

---

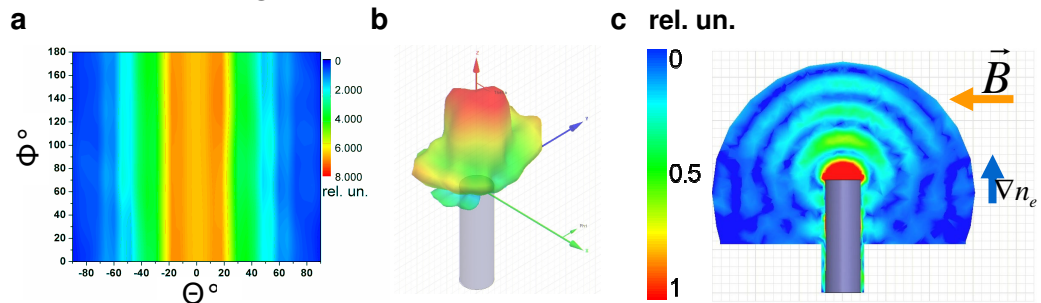
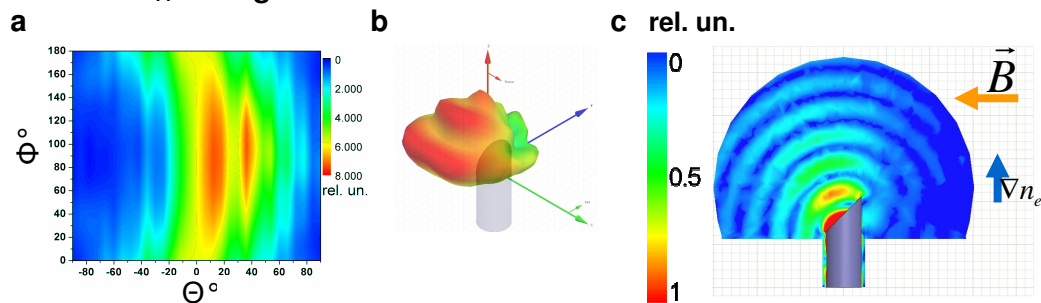
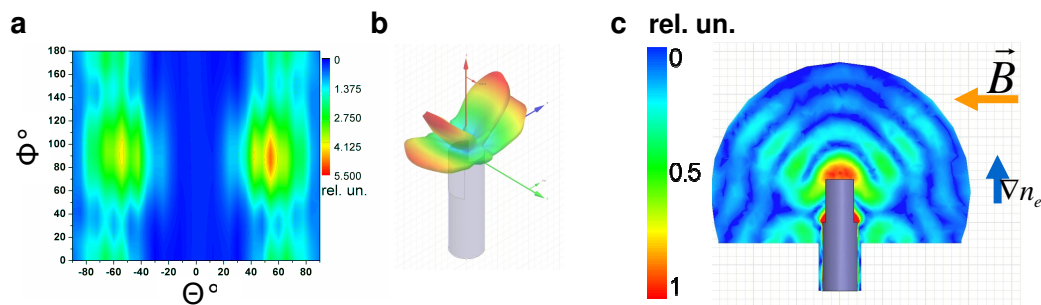
**90° cut TE<sub>11</sub> waveguide**

**45° cut TE<sub>11</sub> waveguide**

**Double slot antenna**


Fig.5.5. Emission patterns calculated using the HFSS code:

- a) The directional pattern in  $(\Theta, \Phi)$  coordinates 10 cm from antenna end
- b) The 3D directional pattern,
- c) E-field distribution in the near field region

The High Frequency Structure Simulation (HFSS)<sup>17</sup> code was used for the antenna characteristics investigation. This code allows simulation of the far and near field emission patterns of arbitrary antenna shapes in a vacuum. The  $\vec{k}$  direction for different antenna types can be calculated as well. In addition, the information about the coupling efficiency of the antenna to the vacuum may be obtained. However, this efficiency may

<sup>17</sup> see Appendix D

changes in the presence of the plasma, and an impedance matching of the antenna to the plasma is needed anyway<sup>18</sup>.

For Many various antenna geometries the far and near field antenna emission patterns have been calculated. Here the results of the calculations for three antennas, which were used in WEGA for the heating, will be shown.

In fig. 5.5 the calculated patterns are presented for the three antenna variants described in section 5.1.2. In this picture column (a) contains the antennas directivity patterns plotted in  $(\Theta, \Phi)$  coordinates (fig. 3.9). The coordinate system used for these calculations is shown in fig. 3.9. The same patterns are plotted in 3D relative to the antenna geometry are shown in column (b). In column (c), the electric field distribution in the region near the antenna is shown. The external magnetic field vector and the density gradient direction are additionally plotted.

The  $90^\circ$  cut  $TE_{11}$  waveguide has a pattern, which is mostly directed along the axis of the waveguide. It means that the HF wave is emitted into the plasma perpendicularly to the external magnetic field vector. The angle  $\theta_0$  of the main lobe is near zero. In this case, the O-mode is almost completely reflected from the O-cutoff layer. The efficiency of this antenna calculated with numerical methods<sup>19</sup> is very low comparing to the next modifications.

The  $45^\circ$  cut antenna pattern shows a maximum of emitted power for  $\theta_0 \approx 13^\circ$ . This is still far from optimal direction. However, more power is launched with the optimum  $40^\circ$  angle. The plasma heating with this antenna configuration is more efficient than with the previous variant, but still rather poor.

The last in this picture is the double slot antenna. This antenna emission pattern has two lobes with  $\theta_0 \approx 57^\circ$ . As mentioned in the previous section it is still not in the optimal direction, however the efficiency of O-SX conversion is higher than in the two previous cases.

The polarisation of the wave in all cases is linear in the  $YZ$ <sup>20</sup> plane. In the 2D field distribution plots  $YZ$  plain is the plain of the picture. For the  $90^\circ$  cut antenna the emitted wave has is almost completely polarized parallel to  $\vec{B}_0$ . For the other two antenna configurations, the  $E_y$  component perpendicular to  $\vec{B}_0$  is present.

---

<sup>18</sup>It is done by a 3-stub tuners or EH-tuner installed in the HF heating transmission line (see section 2.3.2).

<sup>19</sup> See sections 3.4 eq.25 and 4.2.2

<sup>20</sup> On the 3D pictures,  $YZ$  plane correspond to red and blue axes, and (fig.5.5).

---

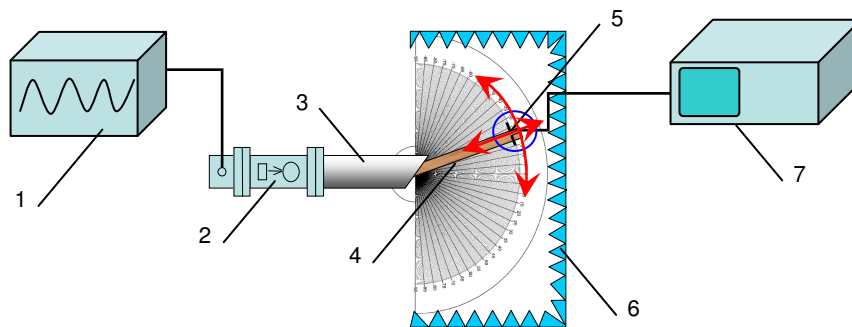


Fig.5.6 Scheme of antenna mission pattern measurement:

1- Anritsu MG3633A generator, 2 - rectangular to circular waveguide transition, 3 - emitting antenna, 4 - angular-radial positioning system, 5 - receiving antenna, 6 - box covered with absorbing material, 7 - Rohde&Schwarz ESPI3 test receiver

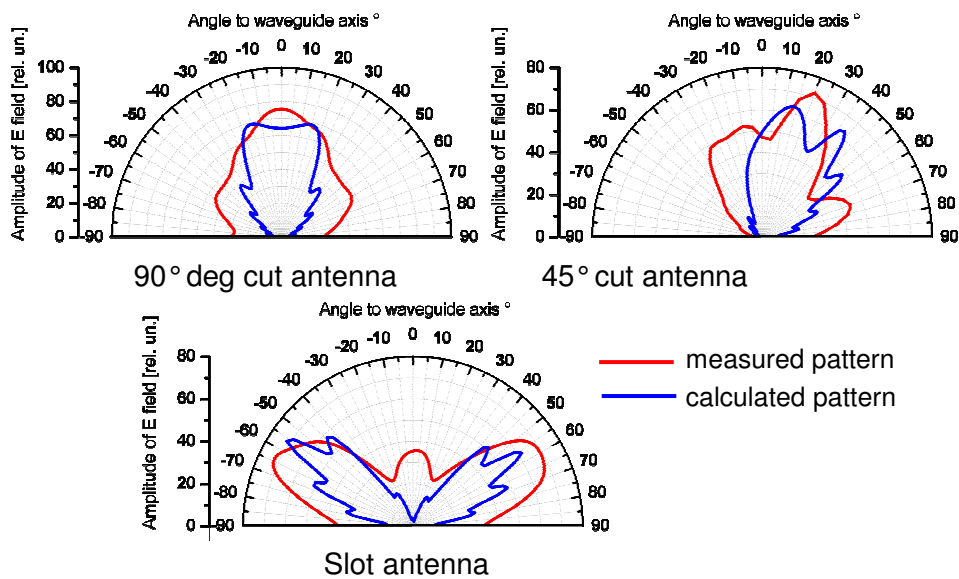


Fig.5.7. Comparison of the measured and calculated antenna emission patterns.

#### 5.1.4. Antenna emission pattern measurements

The emission pattern of the antennas was also investigated with the arrangement shown in fig. 5.6. This system allows to measure the EM field amplitude distribution along the arcs of the different radius, with the centre of the arcs at the antenna end.

The Anritsu MG3633A 10 kHz – 2.7 GHz synthesized signal generator was attached to the antenna through a coaxial-to-waveguide transition. The microwave power was always below 1 mW at 2.45 GHz frequency. The antenna emits the HF in

free space and a small HF probe measures the EM field amplitude in the region near the antenna. A loop antenna with a diameter of 1 cm was used as a probe. The amplitude signal from the loop is picked up by Rohde&Schwarz ESPI3 test receiver. In order to avoid reflections from surrounding objects like walls and metallic constructions in the laboratory, the end of the antenna and the positioning system with the receiving antenna was mounted in a wooden box covered with HF absorbing materials.

In fig. 5.7 the results of the measurements are plotted for three tested types of antenna in comparison to the similar emission patterns calculated with HFSS code. The patterns shown in the picture were measured and calculated along the arc of 15 cm distance from the antenna end. The measured and calculated results are in agreement.

## 5.2. Plasma parameters and heating efficiency evolution

The microwave emitted in the plasma shared between two main processes: the increase of the electron temperature  $T_e$ , and the ionization of particles and thus increasing of the density  $n_e$ . It should be mentioned that density increases only if the plasma is not fully ionized, which is the case for typical WEGA operation. Hence, the electron pressure  $p_e = T_e n_e$  is a good parameter to judge about the heating efficiency.

The efficiency of the heating process is defined by the power absorbed by the plasma relative to the inserted power. This value may be estimated using results from different diagnostics. The efficiency estimated using the fast Langmuir probes measurements and bolometric measurements will be shown. In addition, the results of the numerical simulations will be compared for different antenna types.

Parameter	90° cut 1 <sup>st</sup> harmonic	90° cut 2 <sup>nd</sup> harmonic	45° cut	Slot antenna
$\langle n_e \rangle [n_{e \text{ cutoff}}]$	0.73	1,33	10	12.1
$T_{e \text{ max}} [\text{eV}]$	5	7	6	12
$\alpha [\%]$	2.5	4	70	70(up to 90)
$\beta$	$2 \times 10^{-5}$	$2 \times 10^{-4}$	$6 \times 10^{-4}$	$1 \times 10^{-3}$
$W [\text{mJ}]$	16	38	100	200
$W_{\text{out}}/W (\%)$	240	90	80	10

Table 1. Typical plasma parameters for different heating scenarios:  $\langle n_e \rangle$  average density expressed in terms of cutoff density,  $T_{e \text{ max}}$  – maximal reached electron density,  $\alpha$  – ionization degree,  $\beta$  – ratio of plasma pressure to magnetic pressure,  $W$  – confined energy;  $W_{\text{out}}$  – energy localized outside of the LCFS. (The data is taken from [10])

### 5.2.1. Fast Langmuir probes

The efficiency for different heating scenarios was analyzed in the PhD thesis of K. Horvath [1,10]. Information about the typical plasma parameters for different scenarios is gathered in the table 1. For different antennas described in the previous sections, average density  $\langle n_e \rangle$ , ionization degree  $\alpha$ , ratio of plasma pressure to magnetic pressure  $\beta$ , confined energy  $W$ , and energy localized outside of the LCFS  $W_{out}$  are presented in this table.

A good confirmation of the improvement of the heating efficiency is found in the  $W_{out}/W$  value. It is the ratio of the energy inside and outside of LCFS, which represents the confined and free energy respectively. The decreasing of this value shows increasing of the power deposition in the plasma center.

For the  $90^\circ$  cut antenna the experiments with the 1<sup>st</sup> and 2<sup>nd</sup> harmonic heating are

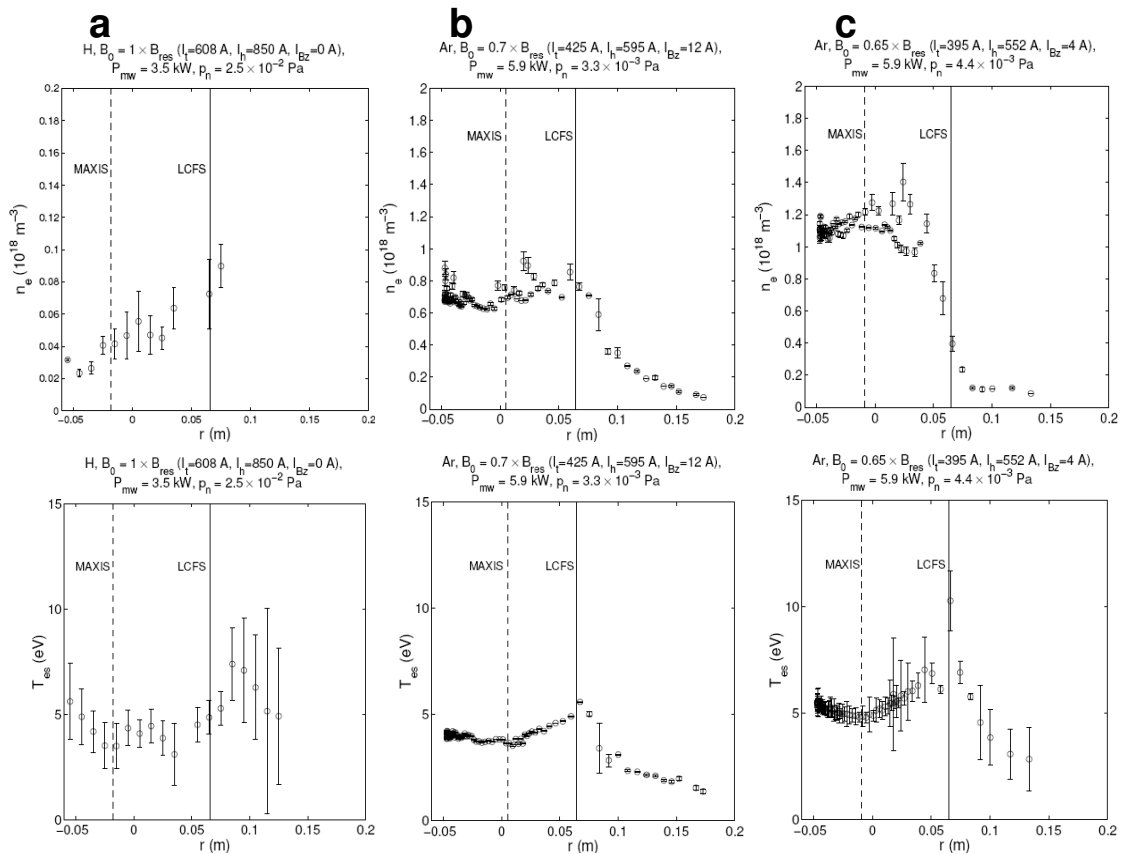


Fig.5.8. Density and temperature profiles measured with the fast Langmuir probes: a - For straight cut waveguide 1<sup>st</sup> harmonic heating b - 45-degree cut c - slot antenna (Profiles are taken from [10])



provided. Toroidal magnetic field in the case of 2<sup>nd</sup> harmonic heating was decreased to half of resonant magnetic field strength  $0.5 \times B_{res} = 0.0438$  T. From the table1, it can be seen that for the 2<sup>nd</sup> harmonic an increase of parameters of all values obtained. It can be assumed that the reason for this is the dependence of the optimal for O-SX conversion  $n_{z\_opt}$  (and thus the  $\theta_{opt}$ ) value on the magnetic field strength. (see eq.23,24). For the second harmonic, the optimal for O-SX conversion  $\theta_0$  angle is  $\approx 36$ . The 90° cut antenna emits more HF power in this direction as shown in fig. 5.5c. Thus, the efficiency of the O-SX conversion is better for the 2<sup>nd</sup> harmonic.

In fig. 5.8 the radial profiles of electron temperature  $T_e$ , and the electron plasma density  $n_e$  measured for each of antenna configurations are presented.

It can clearly be seen that the  $n_e$  profile shape evolving from a hollow profile for the 90° cut antenna to a less hollow of flat profile in case of the 45° cut antenna, and finally peaked profile for the double slot antenna. It can be concluded that the efficiency of the heating is best in the case of the double slot antenna and the power content is closer to the centre of the plasma in this case.

The  $T_e$  profiles are in most cases hollow, but its hollowness is also decreased and the absolute value of the temperature increased for the case of the double slot antenna. The reason for the hollow temperature profile may be that the conversion efficiency even in the best case of the double slot antenna is estimated near 20% of inserted power. Most HF power is absorbed by the plasma edge by multiple reflections as it was for the 90° cut antenna case.

### 5.2.2. Bolometric measurements

Bolometric measurements also can give the information about heating efficiency [23]. The bolometer covers the whole cross-section, as shown in fig. 2.4 (see section 2.2.3). The radiation along one line of sight in Ar plasma is given by

$$P_{rad} = n_e n_i R_{Ar}(T_e), \quad (34)$$

here  $n_e$  and  $n_i$  are the electron and ion density respectively,  $R_{Ar}(T_e)$  is a radiation loss function for Ar plasma which depends on  $T_e$ . This function is presented for Ar in fig. 5.9a. The electron temperature range between zero and dashed vertical line corresponds to the typical operation temperature in WEGA.

The radiation loss function for Ar increases monotonously with increasing  $T_e$  in the low  $T_e$ -range (<10 eV) [28,29] and can be good fitted by a second order polynom fig. 5.9b. So, for the  $1 < T_e < 10$ , eq.34 is monotone ascending. Therefore, in the case of

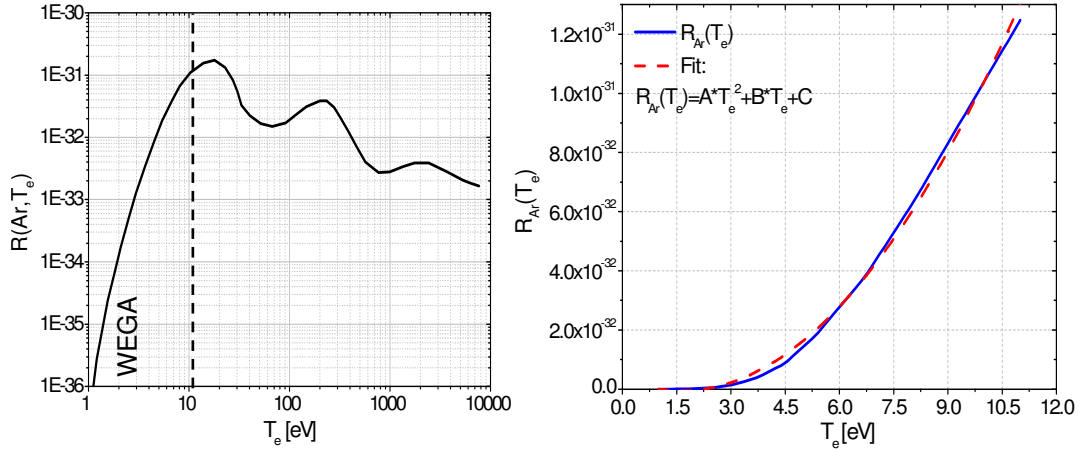


Fig 5.9. a) Radiation loss function

b) Fit of radiation loss function

a rather low impurity concentration in WEGA<sup>21</sup>, the angular radiation profile measured by the bolometer reflects the profile of the plasma pressure  $n_e T_e$ . Angular profiles of radiation intensity are derived from the measured line-integrated signals by considering the optical geometry.

In fig. 5.10 results of the bolometric measurements are shown for three variants of the heating antenna. The time behaviour of radiation intensity measured by 14 channels with different view angle is presented here for three tested antenna geometries. Zero view angle corresponds to the horizontal direction in fig. 2.4. For the 90° cut antenna the emission mostly comes from the edges of the plasma column, the situation is better for the 45° cut antenna, and strong emission from the plasma centre is observed in the case of double slot antenna.

The total radiation loss can be obtained by a linear extrapolating of the calculated power in the viewing range of the whole torus volume.

$$P_{loss} = \frac{\sum_i V_i \cdot I_i}{\sum_i V_i} \cdot V_{torus}, \quad (35)$$

where  $P_{loss}$  is the total radiation loss  $V_i$  is the volume of the plasma seen by the channel with number  $i$ ,  $I_i$  is the average intensity measured by channel  $i$ ,  $V_{torus}$  is the volume of the whole torus. The result of this interpolation shows that ~30% of inserted heating

---

<sup>21</sup> It is indicated by spectroscopic measurements

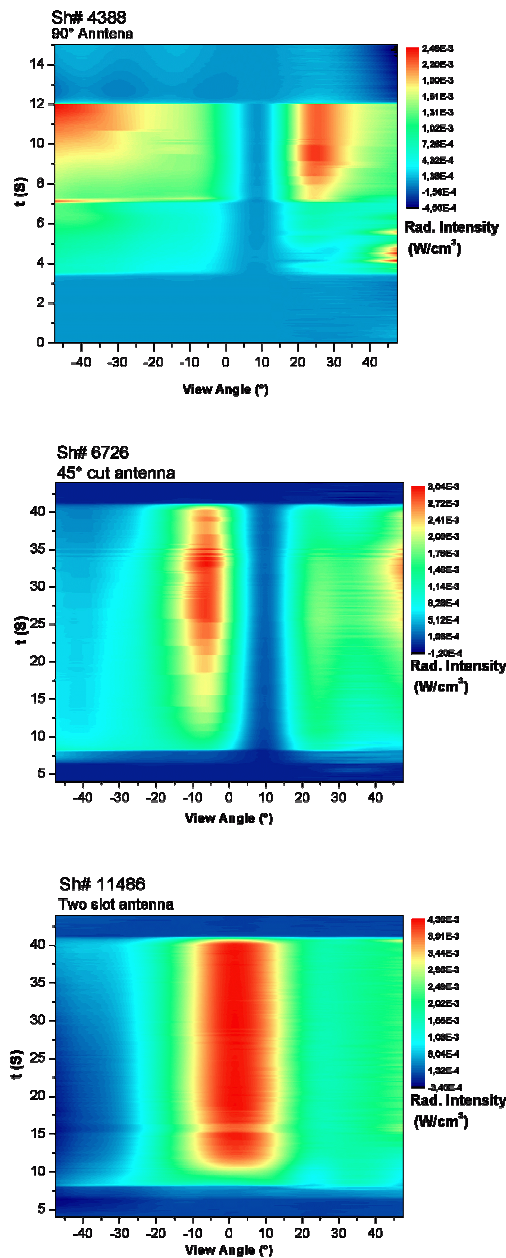


Fig.5.10. The bolometric measurement results for different antenna types.

power is radiated from plasma in the case of  $i/2\pi=0.2$  and power from 1 to 6 kW. The plasma in this measurement was heated using the double slot antenna.

In order to estimate the part of the power lost due to the particle losses (convective loss) experiments with colorimetric measurements were provided. Here a water cooled pipe ( $\varnothing 10$  mm) was used as a limiter. The pipe was bended in a shape that it touched the LCFS tangentially. Limiter touches the plasma and collects the plasma particles from approximately 1/6 of the magnetic surface perimeter near LCFS. The measurements were performed under the similar experiment conditions as for bolometric measurements.

The calorimeter measurement gives approximately 3 to 5% of the inserted power is lost due to convection. The measured value of the convection losses depends on the relation of parallel to perpendicular transport<sup>22</sup>. If parallel transport is much higher than perpendicular, than the value measured by colorimeter is close to the total losses in opposite case it is only part of the total losses and the value measured by colorimeter is

<sup>22</sup> Parallel and perpendicular with respect to the magnetic field line direction.

underestimated. Nevertheless, the obtained value may be used as a lower limit of the power loss due to particle diffusion outside of LCFS.

The total power absorbed by the plasma may be estimated summing the radiation and convection losses. Under described conditions, it is ~35%. This is the lower limit of the total losses, the real value can be appreciably larger. Unfortunately, these measurements were performed for the double slot antenna design only, and it can not be compared with other antenna configurations.

### 5.2.3. Numerical efficiency calculation

The efficiency of the O-SX conversion was estimated using numerical methods. The full wave calculation method described in section 4.2.2 and the Mjøllhus formula (eq.25) was used for this purpose.

The dependence of the efficiency on wave incidence angle calculated with full wave code is shown in fig. 4.6. In fig. 5.11 this result is plotted with marks, which correspond to three tested antennas  $n_z$  values. The double slot antenna has a maximum value of conversion efficiency  $\eta$  from all evaluated configurations.

For the calculation of the O-SX conversion efficiency the acceptance matrix calculated the Mjøllhus formula eq.25 was used.

In fig. 5.12 the acceptance matrix, antennas patterns and the result of the convolution of the acceptance matrix with each of the antennas patterns is plotted in the  $(\Theta, \Phi)$  spherical coordinates (fig. 3.9). The patterns of the antennas were calculated

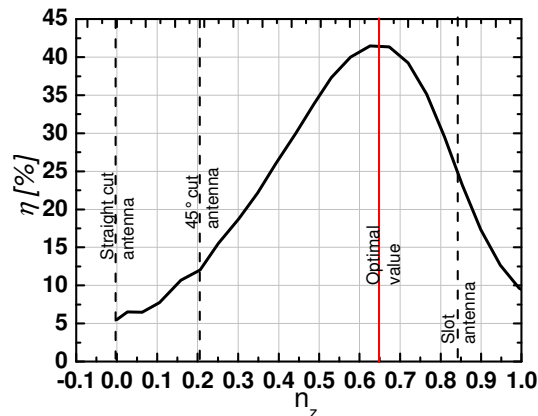


Fig.5.11. Dependence of efficiency calculated with full wave code on parallel to external magnetic field component of  $\vec{n}$

Antenna type	90° cut	45° cut	Slot
accepted power			
Mjøllhus formula [%]	6.7	9	20
Full wave [%]	5.2	12.5	25

Table 2. Efficiency estimated using the full wave calculations with the efficiency of Mjøllhus formula.

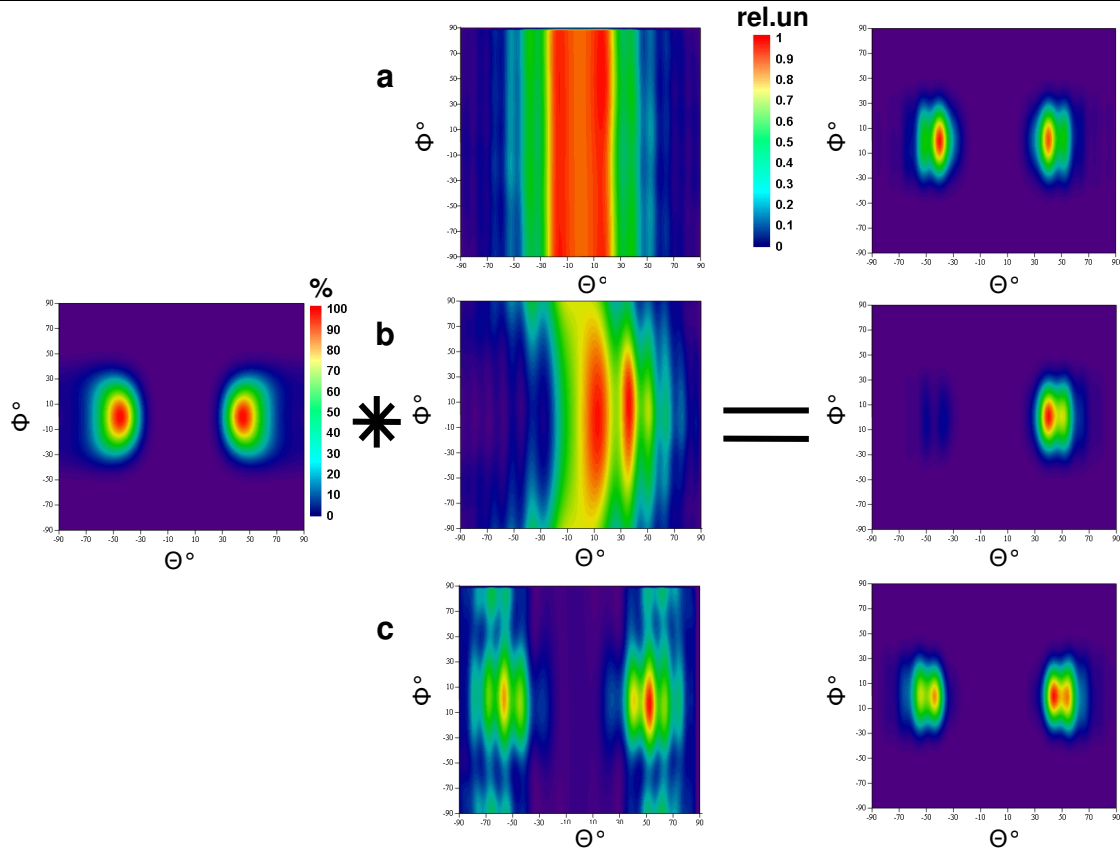


Fig.5.12. Convolution of the matrix calculated with eq.25 and antenna patterns results in the O-SX conversion accepted power: 90° cut antenna (a), for 45° cut antenna (b), for double slot antenna (c).

using the HFSS code. The convolution process was performed using the MathCAD software.

Integration of the antenna pattern matrix and the matrix of the accepted power over all directions and then comparison of the integrated values, gives the part of the power accepted for the O-SX conversion process for antenna configuration under investigation. In WEGA case this calculations give only a rough estimation of the conversion efficiency, because the assumptions of a ray tracing approximation is not fulfilled in the WEGA. Nevertheless, it helps to found an antenna configuration that is more suitable for the O-SX conversion.

The latest full wave efficiency calculations (see section 4.2.2) show the similar results for the conversion efficiency. In the table 2, calculations performed by the full wave code are compared with the results obtained with Mjølhus formula (eq.25).

### ***5.3. Conclusion from antenna optimization***

Improvement of the plasma heating and increase of central power deposition were confirmed with the fast Langmuir and bolometric diagnostics. In accordance with the measurements, the double slot antenna shows the best results. Assumed reason for this improvement is the OXB mode conversion process. The existence of the mode conversion should be proved with the direct measurements of the wave activity in the WEGA plasma. The description and results of measurements are the topics of the next chapters. A double slot type antenna is used now for the heating in the WEGA stellarator for both the 6 kW and the 20 kW magnetron. The HF measurements described in chapters 6 and 7 are made using this antenna type.

---

## **6. Measurements of wave activity in plasma**

Measurements of wave activity in plasma are needed to compare the calculation results with the real situation in the WEGA plasma. To achieve this movable HF probes were used in WEGA together with Langmuir probes.

This chapter describes the measurement system developed to investigate the HF wave field distribution near the heating antenna. The requirements for the probes are discussed in section 6.1.1. A description of the probe testing procedure is given in section 6.1.2. Results of the tests are presented in section 6.1.3.

Section 6.2 describes the measurement system in the WEGA stellarator. Section 6.2.1 describes the probe arrangement. The HF signal route is described in section 6.2.2. In sections 6.2.3 and 6.2.4, the saturation current measurements and acquisition system are described. Section 6.3 describes the method of phase difference calculation, used in the measurements.

### ***6.1. HF probes development***

#### ***6.1.1. Probes requirements***

To measure the field amplitude in the UH resonance region, HF probes should be sensitive to the short wavelength of the SX-mode that propagates toward UHR layer. Also, probes should filter the long wavelength that comes from O-mode propagating from heating antenna in the O to SX mode conversion region. In addition, other modes should be measured to compare the probe behaviour with calculations. This requires further polarization and wavelength selectivity. So, the HF probes for measurements near the UHR layer should be:

- √ sensitive to the short wavelength of longitudinal waves near the resonance layer
- √ insensitive to the long wavelength that comes directly from the heating antenna
- √ polarization sensitive, the electrostatic radial component of electric field should be separated from other modes,
- √ small enough to have the desired spatial resolution.

A special probe shape have been developed meeting all these requirements.

---

The probes act as antennas operating in the non-resonant regime for 2.45 GHz, so the probe design is similar to antenna design. The main difference is that probes operate in plasma with large variety of existing wave modes in particular the electrostatic modes. Thus, at first the probes must be tested in the plasma where electrostatic short wavelength modes can be observed. Probe testing in WEGA is difficult, so the probes were tested on a compact Penning discharge.

### 6.1.2. Probe testing arrangement

In fig. 6.1 the HF probe test device is shown. The vacuum chamber has diameter 37 mm, distance between cathodes is  $\sim 47$  cm, and the cathode diameter is 30 mm. One of the cathodes is emissive. It is made from the Lanthanhexaborid ( $\text{LaB}_6$ ) and heated with a glowing filament (heating current 22.8 A voltage 20.8 V). The voltage between the cathodes and the anode varies from 100 to 2000 V. The discharge current range from 5 to 30 mA.

The system is in a longitudinal magnetic field produced by sixteen planar coils. The current in the coils is up to 105 A. The magnetic field on axis at 105 mA is  $\sim 55$  mT. The working gas is helium at  $10^{-2}$ - $10^{-3}$  mbar.

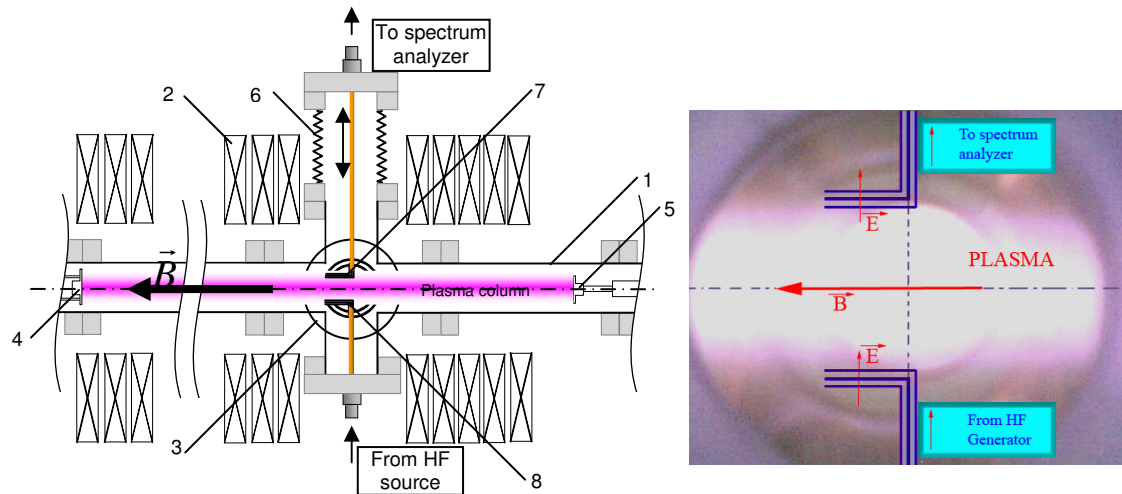


Fig.6.1. (left) Scheme of the measurements in the Penning plasma device.

1 – vacuum chamber (also working as anode), 2 – magnetic field coils, 3 – quartz window, 4 - heated cathode, 5 – opposite cathode, 6 – bellow for probe radial positioning, 7 - receiving probe, 8 – emitting probe

(right) Plasma observed through the quartz window at the position of the measurements, with the probes positions shown schematically.



Probes under investigation were inserted in the plasma from both sides of the plasma column at the same longitudinal direction. One of probes was used as an emitting antenna at a fixed position on one side of the plasma column. The other was used as a receiving antenna. Its radial position was varied during the measurements. The signal from the receiving probe is put into a spectrum analyzer and the dependence of the received signal amplitude on the magnetic field strength and frequency of the input signal is investigated.

Better probe characteristics are obtained at the cyclotron oscillations excited by emitting probe. The maximal magnetic field of 55 mT is below the 1<sup>st</sup> harmonic cyclotron resonance for 2.45 GHz but the 2<sup>nd</sup> harmonic resonance field is reached. All measurements are made at the 2<sup>nd</sup> harmonic resonant field for 2.45 GHz of ~ 43,75 mT, which corresponds to ~ 82 A current in the magnetic field coils.

### 6.1.3. Comparison of the different probe types

Two probe types were tested: 2-pin, and 3-pin probes as shown in fig. 6.2. The 2-pin probe has one pin grounded and another connected to the inner wire of a coaxial transmission line. The length of both pins is 5 mm. This enables measurement of the potential difference in the radial direction and the  $E$ -field component perpendicular to the pins as shown in fig. 6.2.

The 3-pin probe has an additional grounded pin. This allows measurement of short wavelengths comparable with the distance between the pins. Long wavelengths are shielded by the grounded pins.

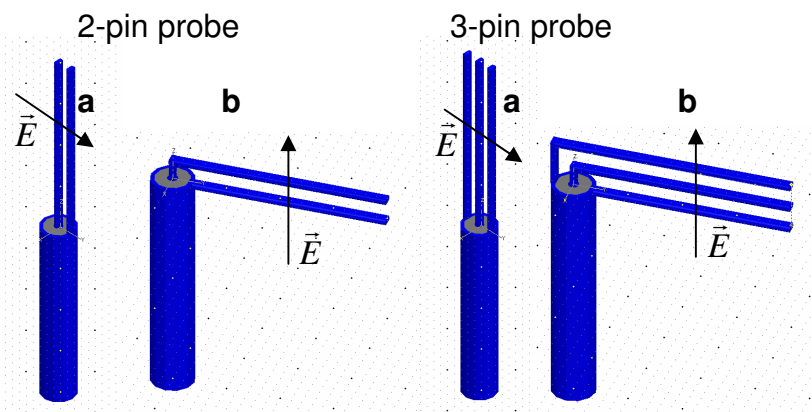


Fig.6.2. Two variants of the probes:

a) Probe used for measurements in WEGA,

b) Bent probes used for measurements in the Penning discharge plasma.

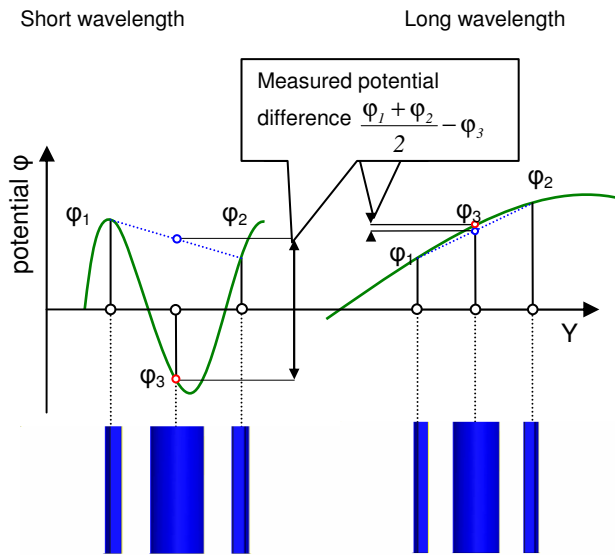


Fig.6.3. Principle of the 3-pin probe operation.

For long wave potentials, the grounded pins compensate the potential on the central pin. For short wavelength potentials, the signal amplitude may be many times greater. These two cases illustrated in fig. 6.3.

However, for shorter wavelengths comparable with the electron Larmor radius in the WEGA plasma  $\sim 0.01\text{ mm}$ , the probe sensitivity decreases because the wavelength is comparable with the pin size.

Each probe type has two different geometries as shown in fig. 6.2. The bent geometry is used in the small linear Penning plasma device. The straight geometry is used for measurements in WEGA. Bent test probes are needed to measure the radial  $E$ -field component of the HF wave. In the Penning device, there is insufficient space to tilt a straight probe in the device.

During measurements, the frequency of the emitted wave is swept in the range from 1 to 2.5 GHz and the magnetic field from 35 to 55 mT. The radial position of the probe ranges from 0 to 1.5 cm from the chamber wall. In fig. 6.4 the amplitude of the HF signal received from the 3-pin probe is plotted as a function of frequency and

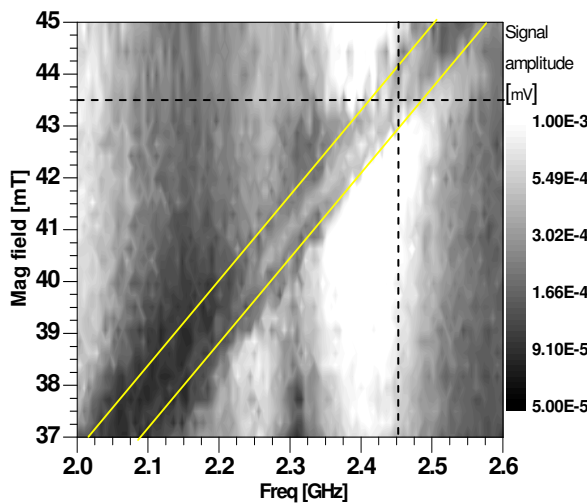


Fig.6.4. The amplitude of the HF signal received with the 3-pin probe as a function of the frequency of the emitted wave and the magnetic field in the center of the Penning discharge.

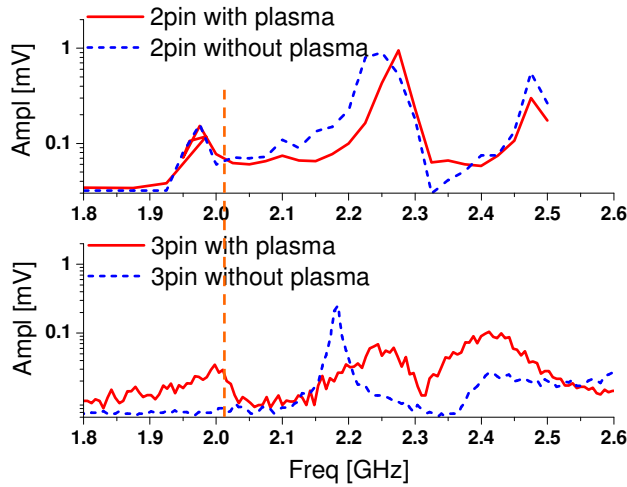


Fig.6.5. Comparison of the two probes (2-pin & 3-pin) with and without plasma

Plasma parameters are the same in both cases. The magnetic field is  $\sim 36$  mT. The resonance frequency is 2.01 GHz

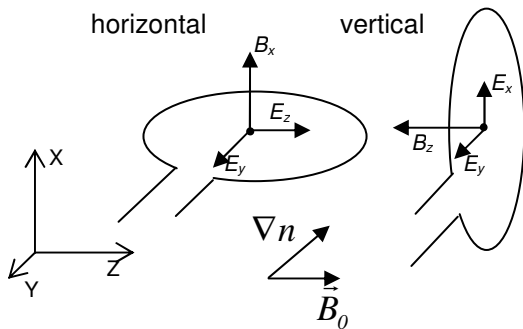


Fig.6.6. Two loop probe orientations relative to the external magnetic field.

A loop probe was also used for the measurements in WEGA. The loop probe is sensitive to the magnetic component of the wave. Using this probe the electromagnetic waves behaviour can be investigated while ignoring the electrostatic waves near the resonance layer. The plane of the loop may be parallel or perpendicular to the external magnetic field as shown in fig. 6.6. When it is parallel to the magnetic field, it is sensitive to the wave polarized in the horizontal plane, in which the magnetic field vector lies. When the loop plane is perpendicular to the external magnetic field, it is

longitudinal magnetic field strength. The radial position in this case is  $\sim 11$  mm from the axis of the plasma column (7.5 mm from the chamber wall). This is where the 2<sup>nd</sup> harmonic resonance is most pronounced. The lines show the region where the probes respond to the 2<sup>nd</sup> harmonic cyclotron frequency is found. The cross-point of the dotted lines is the position of the 2.45 GHz resonance.

As shown in fig. 6.5. Around the 2<sup>nd</sup> harmonic frequency, the 2-pin probe has little difference between the signal in plasma and in vacuum. Therefore, for the 2-pin probe, direct or capacitive coupling to the emitting antenna is prevalent, and the plasma resonance effects can not be easily observed. In contrast, the 3-pin probe shows an increase in the signal in plasma, particularly at the position of cyclotron resonance and damping of the intrinsic antenna resonance.

The 3-pin probe is more sensitive to the 2<sup>nd</sup> harmonic

cyclotron mode and was therefore chosen for measurements in WEGA.

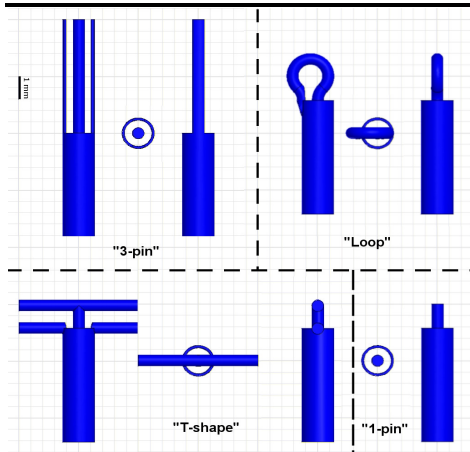


Fig.6.7. The designs of the probe that were used for the measurements in the WEGA plasma. All probes have coaxial feeding and are made of stainless steel.

sensitive to the magnetic field of the X-mode. In these measurements, the loop probes are used in both configurations simultaneously.

Another probe type tested in the WEGA is a simple 1-pin probe. It is 1 mm length and directed along the line of measurements, to measure the radial  $E$ -field along the minor radius. However, it has no wavelength selectivity and the interpretation of the signal from this probe is difficult.

Thus, the 3-pin probe was used for measurements in WEGA. The pin probe and the T-shape probe, shown in fig. 6.7 were tested directly in the WEGA plasma.

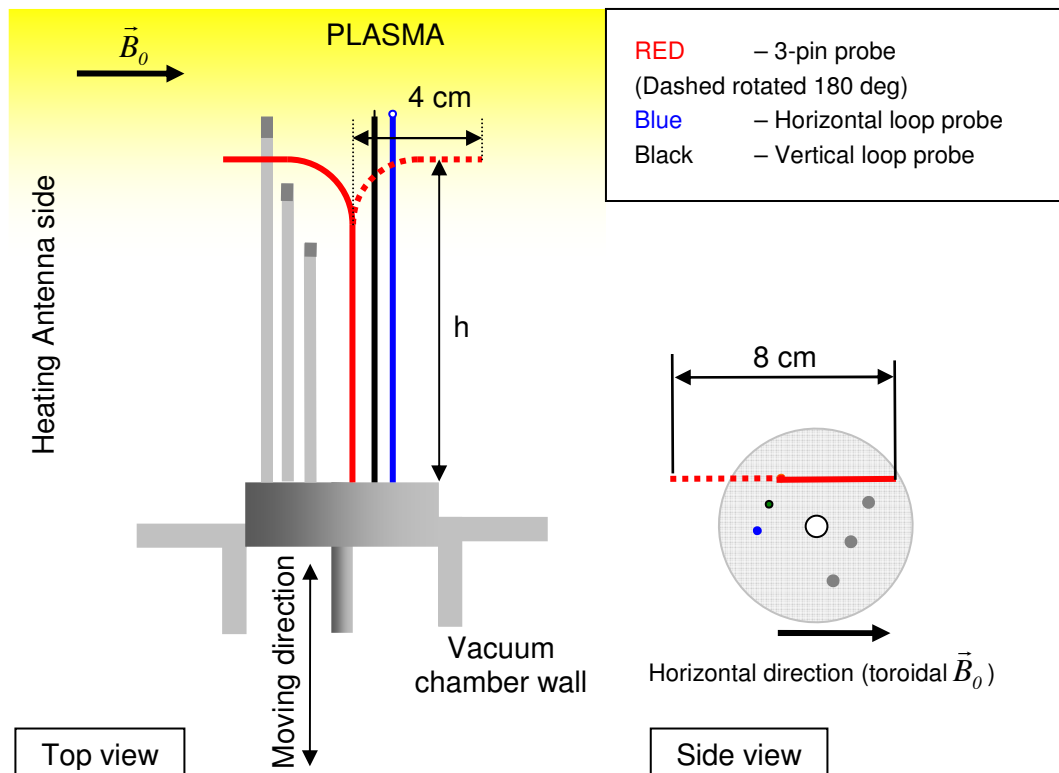


Fig.6.8. The probe array in WEGA

## 6.2. WEGA measurement arrangement

### 6.2.1. Probes set in the WEGA

In WEGA, three probes are used simultaneously for HF measurements. The 3-pin probe is always used while the other two probes are selected from the probes shown in fig. 6.7. Three Langmuir probes are also used in the region of the HF measurements to obtain information about the ion saturation current and thus the plasma density near the antenna. The density radial profile  $n_e(r)$  gives information about the radial position of the UHR layer. This is used in the full wave calculations.

In fig. 6.8 top and side views of the probe set used in WEGA are shown. The 3-pin probe is bent  $90^\circ$  to have polarization sensitivity in the direction of the radial component of the  $E$ -field. In addition, the bend allows variation of the probing position 8 cm in the toroidal direction by rotating the probe around its axis, as shown in fig. 6.8 by the dashed red line. The figure also shows two loop probes. The most important measurements were made with this configuration of probes, but other configurations were also used.

Different probe types were used for measurements and the length of the probes was varied, (shown as  $h$  in the figure). Measurements were made over the whole region between the vacuum chamber and the LCFS.

In fig. 6.9 the position of the measurements is shown relative to the heating antenna port. The measurements were performed in the heating antenna region. This position is marked on the figure with a blue line. The line is inclined at  $9^\circ$  in toroidal angle to the heating antenna axis, and  $22.5^\circ$  in the poloidal angle. Unfortunately, the measurements in the heating antenna horizontal plane are not possible because the

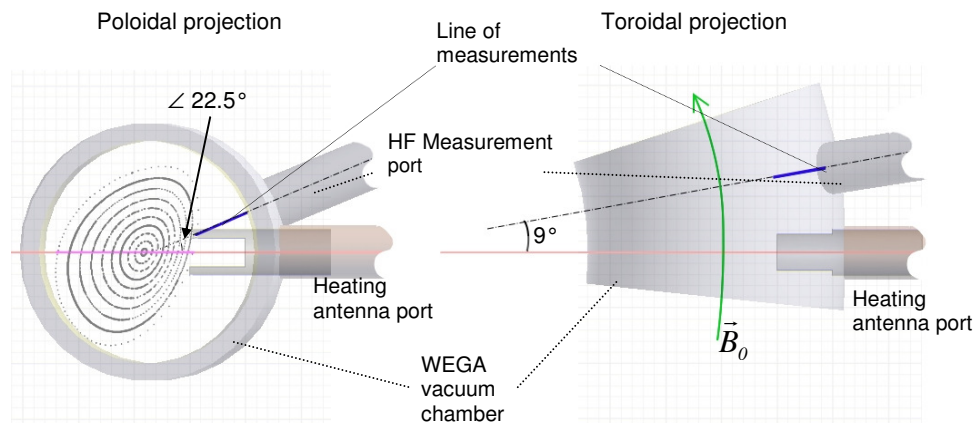


Fig.6.9. Geometrical position of the measurements. The red horizontal line is the axis of the heating antenna port. Measurements were performed along the blue line.

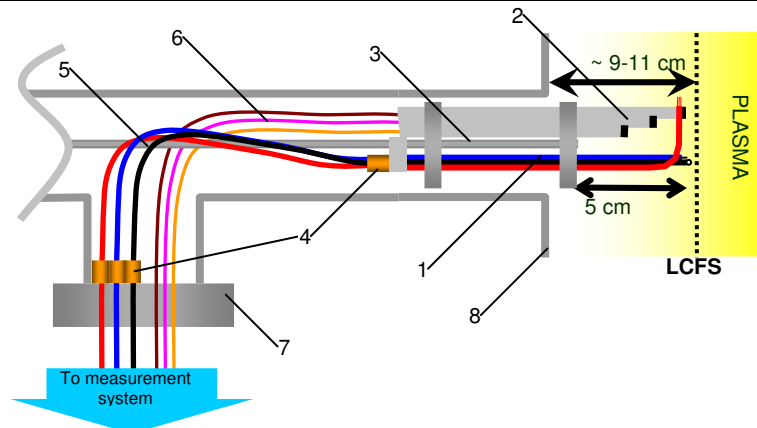


Fig.6.10. The arrangement of the measurement system (vacuum part):

1 - HF probes, 2 - Langmuir probes, 3 - guide bar with fitting elements, 4 - SMA connectors, 5 - HF coaxial flexible vacuum cables, 6 - vacuum cables, 7 - CF-100 vacuum flange with 3 HF and 3 electrical feedthrough, 8 - WEGA vacuum chamber wall.

nearest port with the horizontal orientation positioned  $36^\circ$  in the toroidal direction it is  $\sim 56$  cm. The measurements must be near the antenna because the full wave calculations show that the conversion region, is  $1 \div 2$  vacuum wavelengths of the heating wave, i.e. 12-25 cm in the toroidal direction.

Nevertheless, because the antenna pattern is rather wide in the poloidal direction, the measurements in the poloidally shifted position also should show the resonant effect.

In fig. 6.10 the vacuum part of the measurement system is presented. The set of HF and Langmuir probes were placed on the guide bar with the fitting structure movable in the radial direction over a 5 cm range. The computer controlled step motor provides the 0.1 mm precision positioning of the probe set. The size of the probes is much larger than the precision of the positioning, so the measurements were usually performed with a 0.5-1.5 mm step size.

The probes tips are connected to SMA plugs using a coaxial line. The inner wire diameter is 0.5 mm, the inner diameter of the outer conductor is 1.15 mm, which corresponds to  $50\Omega$  impedance in vacuum. Ceramic spacing washers are used between the outer and the inner conductors of the coaxial line to fix the distance between them. These have no significant effect on the total line impedance.

The HF probes are connected to vacuum feedthrough that was mounted on a CF-100 flange, by a flexible vacuum compatible  $50\Omega$  coaxial cables with a SMA type connector on both ends. The Langmuir probes are also connected to the feedthrough with the vacuum cables.

The distance between the WEGA chamber wall and the LCFS position varies and depends on the magnetic field configuration. However, it can not be closer than  $\sim 10$  cm because position of the LCFS in WEGA plasma is defined by the heating antenna, which works as a limiter in this case and have the length of 11 cm from the outer wall. Measurements are taken in this region as the plasma reaches its critical density for the 2.45 GHz frequency outside of the LCFS and all conversion processes should take place there. The probes also can not penetrate in the dense plasma as it would risk to damage to the probes from the hot plasma flux.

Measurements are performed as follows: the initial position of the probes set is outside of the vessel corresponding to the left edge position of the probes in fig. 6.10. After starting the magnetic field and HF heating, the measurement system waits for 3-5 seconds for the plasma to stabilise then starts the oscilloscopes. The oscilloscopes are triggered by a common pulse generator. The signals from all eight channels are acquired simultaneously. After that the data acquired by the oscilloscopes is transferred to

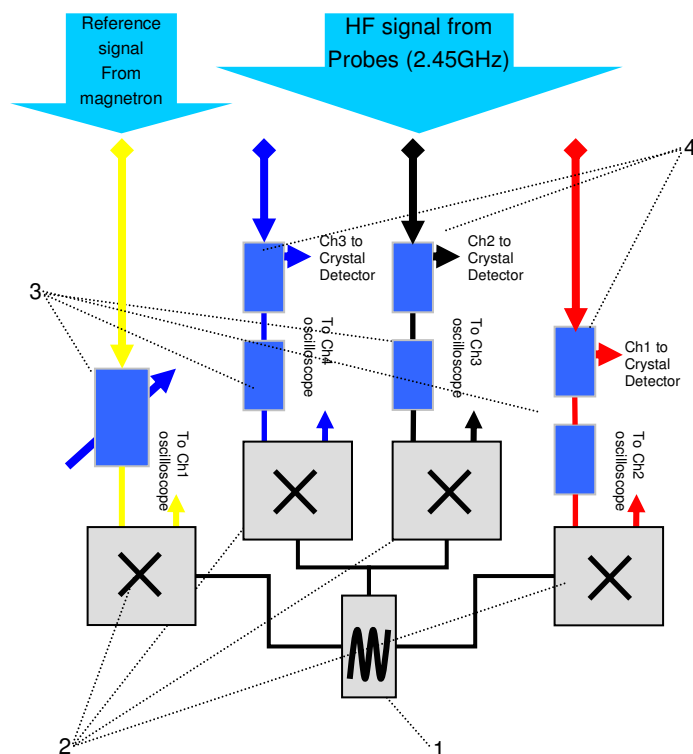


Fig.6.11. The high frequency measurement system:  
1- Common local oscillator 128.4 MHz, 2- Mixers, 3- Attenuators, 4- Power splitters

computer memory, the single point measurement is finished. The probe set is moved further into the plasma for one 0.5-1.5 mm step, and the oscilloscopes are started again. This process continues up to 2-3 seconds before the heating is switched off. Thus, during the discharge, the probes set travel some part of the distance to the end position in stable plasma. The length of travelled path depends on the step size, discharge duration, and quantity of points that the oscilloscope acquires for each point. Usually three to five discharges are needed to measure complete set of profiles.

### 6.2.2. HF probes signals

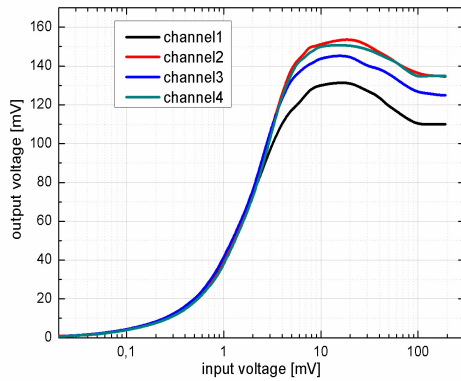


Fig.6.12. Down sampling mixers output signal level depending on the input signal level (calibration for 2.45 GHz)

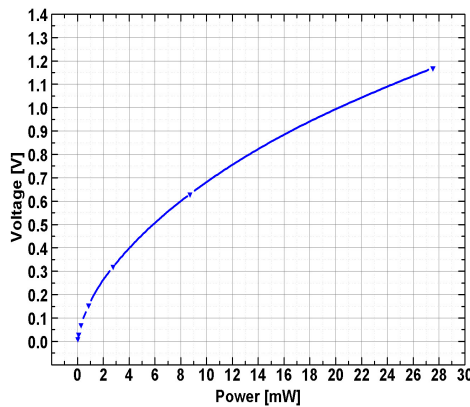


Fig.6.13. Calibration curve of the crystal diode: output voltage versus input power.

phase difference for the signals from the probes. An amplitude measurement for this channel is not needed so the signal from the directional coupler comes to this mixer only through the step attenuator. The other three mixers are used for the signals from HF probes. The output of all four mixers is connected to oscilloscope-1 shown in fig. 6.17.

The HF probe signals come out of the vacuum vessel via low-loss high frequency cables as shown in fig. 6.11. First, power splitters send part of the probe power to crystal diodes for amplitude measurements. The rest of the power is sent to down sampling mixers for phase measurements.

All the mixers use a common local oscillator to reduce the frequency and preserve the phase difference information between the signals. The frequency reduction is needed because the oscilloscope maximum sampling rate of 1 GHz. is not high enough to resolve the 2.45 GHz HF signal. Low-noise KU2425 converters are used for signal mixing. These mixers are certified to the frequency band from 2.425 GHz to 2.475 GHz on the input and 100 MHz to 150 MHz on the output. Thus, the initial 2.45 GHz frequency is in the center of the operating band is reduced to 125 MHz, which is then sampled at 1 GHz.

There are four mixing channels. One is always connected to the output of the directional coupler installed on the heating transmission line. This signal is used as a reference channel for the calculation of the



The amplitude of the signals may be also extracted from the mixers signals, but only in the low power region because the mixer output signals saturate above  $\sim 10$  mV of input signal and are nonlinear up to 225 mV (see fig. 6.12). 225 mV is operational limit of the converters and signal of higher level may damage the devices. Thus, attenuators of  $\sim 40$  dB are used for probes channels and a 0-60 dB step attenuator is used for the reference channel.

Usually the signals from the probes are in the saturated region of the mixers above 10 mV, so the amplitude of the signals is measured separately using crystal diodes. The HP420A crystal detectors are installed on the power splitter before the attenuators so the signal amplitude on them is much higher than on the mixers input. The voltage on the crystal detectors is proportional to the square root of the power, (see fig. 6.13) and thus proportional to the amplitude of the  $E$ -field of the detected wave. The outputs of the crystal diodes are connected to the inputs of oscilloscope-2 as shown in fig. 6.17.

### 6.2.3. Langmuir probes measurement

In fig. 6.14 the density profile measured with fast Langmuir probe is shown, here the shadowed region is not accessible with the HF probes because of reasons described in section 6.2.1.

The results of these measurements can not be used because of two reasons. First, the fast Langmuir probe position is shifted in toroidal direction from the heating antenna position.

Thus, it may not give proper information about density profile in the region of heating antenna. The second reason comes from the fig. 6.14. In the region accessible by HF probes, information about the density profile is very poor, only a few points are measured there.

Langmuir probes, used have a cylindrical pin oh 5 mm height and 3 mm diameter. Such large pins are required because the measurement is in the edge region. Here the plasma density is comparatively low and a large probe area

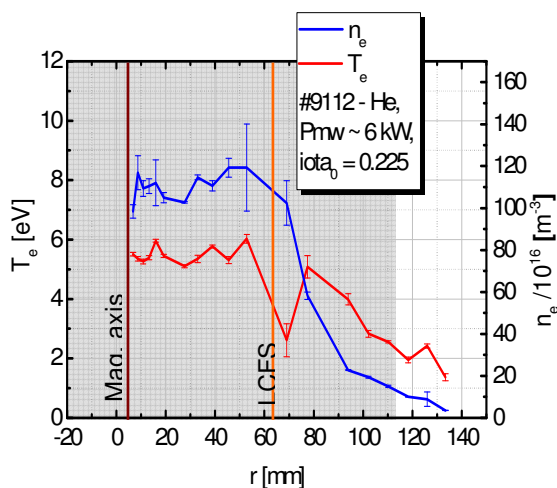


Fig.6.14. Density profile measured with fast Langmuir probe. Shadowed region is not accessible by HF measurements.

is required to obtain sufficient signal to noise ratio.

Oscilloscope-2 measures the voltage on a 2 kΩ resistor when a -90 V is applied to the Langmuir probe as shown in fig. 6.15. The measured voltage is proportional to the ion saturation current, which is calculated from Ohm's law  $I_{sat} = U_{measured}/2 \text{ k}\Omega$ .

To estimate the plasma density, information about the electron temperature and gas nature is required. The saturation current is proportional to  $\sqrt{T_e}$ .

$$I_{sat} \sim \frac{en_e S}{4} \sqrt{\frac{kT_e}{M_i}} \quad (36)$$

so that,

$$n_e \sim \frac{4I_{sat}}{eS} \sqrt{\frac{M_i}{kT_e}} \quad (37)$$

In the experiments, *He* or *Ar* is the working gas, so the ion mass  $M_i$  is 4 or 40 atomic mass units respectively. The temperature  $T_e$  is determined from the fast Langmuir probe measurements [10] where the whole  $U/I$  characteristic is measured. The temperature of the electrons at the edge is estimated to be  $\sim 5 \text{ eV}$ . Using this data, allows estimation of the density in the measurement region. Density is calculated for Maxwellian temperature distribution. However, the plasma in WEGA assumed to have a two-temperature distribution. Therefore, the ion current is not fully saturated in the WEGA plasma. Presence of a high temperature electron component is described in K. Horvath PhD thesis [10]. The measurement was performed in the point marked in fig. 6.16, which corresponds to -90 V of applied voltage. Further investigations show

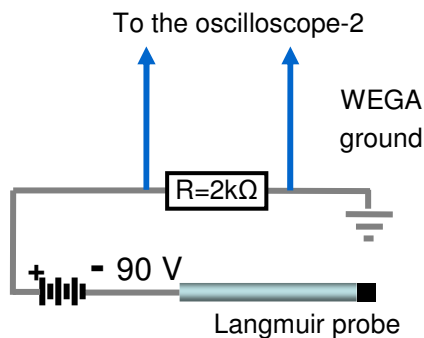


Fig.6.15. The ion saturation current measurement arrangement

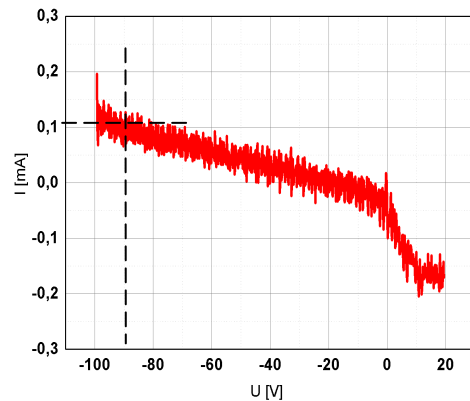
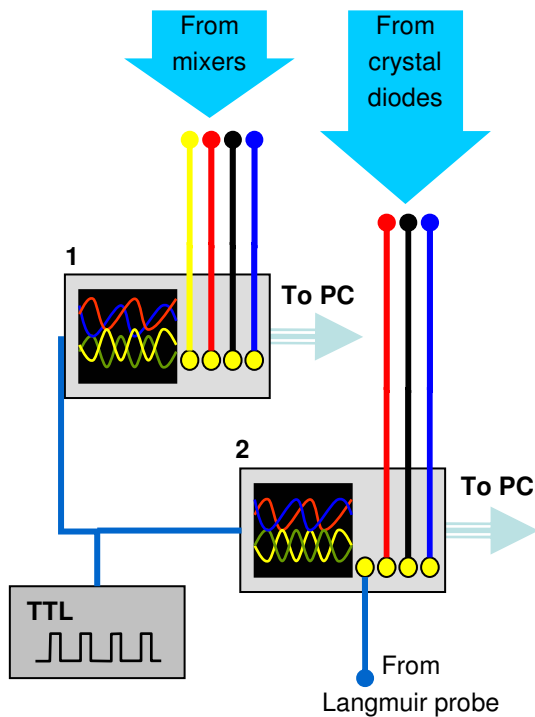


Fig.6.16. The typical Langmuir probe  $U/I$  characteristic obtained in the WEGA plasma.

that the measured with the Langmuir probes density is usually overestimated, and it should be recalibrated using the results of HF measurements.

#### 6.2.4. Data acquisition system



*Fig.6.17. Oscilloscopes arrangement:  
1 – the oscilloscope used for the phase measurements  
2 – the oscilloscope used for the amplitude and the saturation current measurements*

the oscilloscope-computer connection is made using an optic fibre line to isolate electrically the oscilloscopes from the computer.

The signals acquired by the oscilloscopes are transferred to a computer using control interface written in National Instruments LabView6 software. This interface controls the position of the probes, the timing of the measurements, the oscilloscopes operating regimes, reading data from oscilloscopes, some data post-processing and saving of data in ASCII files.

Two oscilloscopes are used for signal acquisition. One is used for the phase measurements and record the signals from all four mixers, the other records the signals from the crystal diodes and the Langmuir probes. The scheme is shown in fig.6.17. The channels of the second oscilloscope are used in different combinations. The figure shows the combination where one channel is used for the Langmuir probe and three channels are used for the signals from the crystal diodes. For the density measurements of two or three probes, some of the HF amplitude signals are replaced by saturation current signals. Both oscilloscopes use a common external triggering to provide simultaneous measurements of the phase and amplitude.

The oscilloscopes grounds are connected to the WEGA ground. The

The interface has a module for phase difference calculation for the mixer signals. In addition, the saturation current is converted to density immediately after the measurements.

All the measured data is saved for further processing and plotting.

### 6.3. Phase difference calculation

The signals from the output of the mixers have frequency  $\approx 125$  MHz. To calculate the phase difference between the HF probe signal and the reference signal from the HF heating transmission line, the sampling rate should be at the Nyquist frequency or higher.

The oscilloscope is set to acquire 500 points per one measurement using a 1 GHz sampling rate giving a 500 ns record.

The phase of the signals from the mixers is not stable and fluctuates over the range  $\pm 30$ - $60^\circ$  on a time scale of  $\sim 100$   $\mu$ s. If the phase is measured for period of time 500 ns or even 10  $\mu$ s then multiple measurements in one radial position should be averaged. It will again increase the time of measurements and data processing dramatically.

Assuming the signal amplitude stays constant<sup>23</sup> during the one measurement, the signals are read from mixers for a much longer time of 0.5 ms. The sampling rate of the oscilloscope in this case is much lower (1 MHz) and the time step between points is 1  $\mu$ s. Thus, one

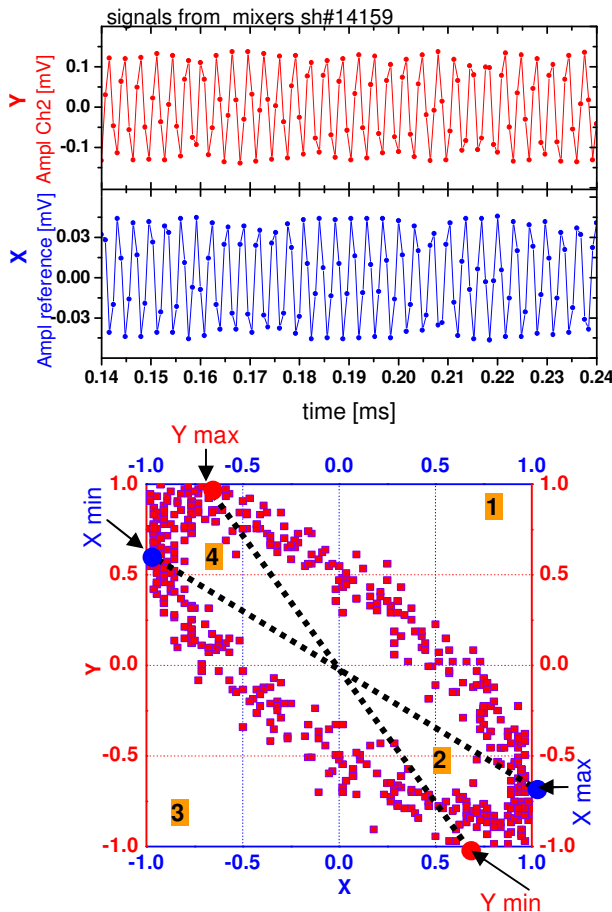


Fig.6.18. Example of the measured signals from the mixers (top) and Lissajou figure derived from these signals (bottom)

<sup>23</sup> This is because all the mixers work in saturation mode fig.6.12

1)	$\arccos(X(t))$	$+ \arccos(Y(t))$
2)	$-\arccos(X(t))$	$+ \arccos(Y(t))$
3)	$\pi - \arccos(X(t))$	$+ \pi - \arccos(Y(t))$
4)	$\arccos(X(t))$	$- \arccos(Y(t))$

Table 3

point is read per  $\sim 125$  periods of the mixer signal oscillation. 500 points are acquired of each coordinate point.

Fig. 6.18(top) shows examples of measured signals using this technique. Here only the part of the measured data is shown. The long time of measurements, allows coverage of the time of the signal phase fluctuations. It is no longer a purely sinusoidal signal, but it is still possible to extract the phase difference information. Plotting a ratio of the data measured by the HF probe to the reference signal from the heating transmission line gives a Lissajou figure shown in fig. 6.18(bottom). The Lissajou figure shows, that the phase shift fluctuates near about a constant value. If the amplitude of the signal were not stable during one measurement, a clear Lissajou figure would not be obtained and the phase calculation will give incorrect results. However, this very seldom happens in these measurements.

The phase shift between the reference signal  $X(t)$  and signal from one of the probes  $Y(t)$  is calculated as a combination of  $\arccos(X(t))$  and  $\arccos(Y(t))$ . In different parts of the Lissajou figure different combinations of these terms are used as shown in table 3. These parts are marked in fig. 6.18(bottom) with numbers from 1 to 4. These regions are defined by the positions of the extreme points of  $X(t)$  and  $Y(t)$ . All the signals should be centered and normalized on maximum values to obtain the variation of values between -1 and 1 where the  $\arccos$  function is defined.

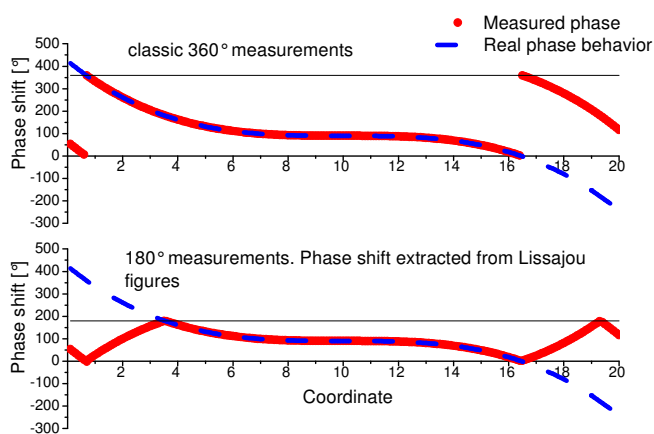


Fig.6.19. Comparison of the phase shift calculation methods.

Thus, the phase information is extracted for each time point  $t$  of the single spatial point measurement. Finally, this gives 500 values of the phase difference for each coordinate point are obtained. Usually there is 30 to 60 measurement points for one radial profile, which gives 150000 to 300000 values of phase shift for each HF channel.

On all the phase difference

---

profiles shown in chapter 7 the values of the phase difference for all 500 points is plotted in each coordinate point where it was measured.

When the phase shift is extracted from the Lissajou figure in described way, the information about the direction of “rotation” is lost. Therefore, the positive and the negative phase shift can not be distinguished, the obtained values are in the range 0-180° instead of 0-360°. When the phase reaches the border (0 or 180°) it does not jumps to the other side of the plot like in 360° measurements, but just “reflected” from the border as shown in (fig. 6.19). Consequently it is impossible to distinguish the direction of wave propagation.

The measured phase shift gives information about the phase behaviour near the resonant region and the  $k_{\perp}$  (or wavelength) value in the region of measurements.

#### **6.4. Summary of the measurement system**

The measurement system consisting of movable HF and Langmuir probes was successfully developed and installed. The 3-pin HF probe was designed for the measurements of  $E$ -field radial component of electrostatic waves with wavelength in the order of 1 cm. Additionally, the loop probes manufactured which allows to observe the electromagnetic waves with different polarizations. The Langmuir probes are used in the HF measurement region as well.

The waves in plasma were investigated for different regimes of WEGA operation. The result of the measurements will be described in the next chapter 7 for 3-pin probe and loop probe in two variants of orientation.

---

## **7. Measurements and calculations results**

In this chapter, the results of the measurements made by the measuring system described in previous chapter are presented and compared with the calculation results.

The aim of the measurements is to find signatures of the OXB conversion process. The main feature of the wave in this process is that the amplitude of the radial  $E$ -field rises near the UHR layer due to the resonance. It is also important to mention that amplitudes of all wave components vanish beyond the L-cutoff layer. Such behaviour is predicted by the full wave calculations. Although, calculations performed with a linear density profile capture the main features described above, it is necessary to incorporate in the calculations the real density profile as measured by Langmuir probes in order to reproduce the experimental results accurately. Full wave calculations based on the measured  $n_e$  profile allow not only to compare the common behaviour of the waves near the UHR layer, but also to predict more accurately the  $E$ -field distribution over the region of the measurements. For this reason, special care was taken in measuring the  $n_e$  profile in a variety of WEGA regimes.

The chapter is divided in two sections. In section 7.1 Langmuir and HF probes measurements are described and analysed. In particular, subsection 7.1.1 is dedicated to Langmuir probe measurements and 7.1.2 to results of HF amplitude and phase investigations for 3-pin probe and loop probes in two orientation variants.

Section 7.2 is dedicated to the results of the calculations and their comparison with the measured data.

### **7.1. Measured data**

#### **7.1.1. Measured density**

The density profiles in the vicinity of the antenna are important because of many reasons. The main reason is that these profiles are used in the full wave calculations to bring it closer to the situation in WEGA plasma. The second reason is that it is important to know the  $L_n$  value in the conversion region to estimate the conversion efficiency with eqs.25,27. In addition, it gives the location of the UHR-layer position.

---

In general, the UHR location also depends on the magnetic field, but this was kept constant in our measurements ( $B_o = 0.65 \times B_{res}$ <sup>24</sup>). Hence, the UHR layer position was mainly defined by the electron density value (eq.14). In most of the investigated plasma regimes it may be assumed that the UHR layer was at the point where density reaches  $n_e = 0.57 \times n_{cutoff}$ . Since  $n_{cutoff} = 7.5 \times 10^{16} \text{ m}^{-3}$  for 2.45 GHz this corresponds to  $4.3 \times 10^{16} \text{ m}^{-3}$ .

The density profiles were measured under different discharge conditions. The input power, vertical magnetic field, and iota, were varied. All measurements were made with the Ar as a working gas, because He yields too low density values.

The density measurements also help to choose the optimum regime for the measurements with HF probes. The regime of plasma operation should be chosen in such way so that the UHR layer is in the region of our measurements. As it was already mentioned in describing the measurement system, the probes can not penetrate too deeply into the plasma. Apart from technical difficulties, there is another reason for this: if the probes touch the dense plasma core, they could be damaged by overheating. Therefore, a regime where the UHR layer stays out of the “dangerous” region should be found. This task is simplified because of the low heating frequency. The cutoff layer and UHR layer are positioned near the plasma edge, and outside of the LCFS as shown in fig. 7.2. It allows to find the regime where both these layers may be accessed by the HF probes.

In fig. 7.1 density profiles measured with the Langmuir probes at the edge of the WEGA plasma are shown for the different iota (a) and vertical field values (c,d). The changing of these parameters strongly affects the density profiles shape and thus the UHR and Cutoff layer position. The horizontal lines show the values of  $n_{cutoff}$  and  $n_{UHR}$ . The UHR layer position is calculated for  $B_o = 0.65 \times B_{res}$ . Radial dependence of the  $B_o$  is not taken into account because it changes a negligible amount in the region of measurements, and almost does not affect the UHR position.

According to these measurements, it is seen that the cutoff layer enters the region of measurements for low iota values  $i/2\pi = 0.2$ . The reason for this is that the plasma cord in this case is wider as it is also visible in fig. 2.3,7.2. Another possibility to tailor the cutoff and UHR layer position is by varying of the current in the vertical field coils. The changing vertical magnetic field leads to a plasma in the horizontal direction toward or outward the torus centre. Thus, the density profile in the measurement region

---

<sup>24</sup> For the 2.45 GHz frequency it is  $B_o = 0.0875 \times 0.65 \approx 0.057 \text{ T}$ .



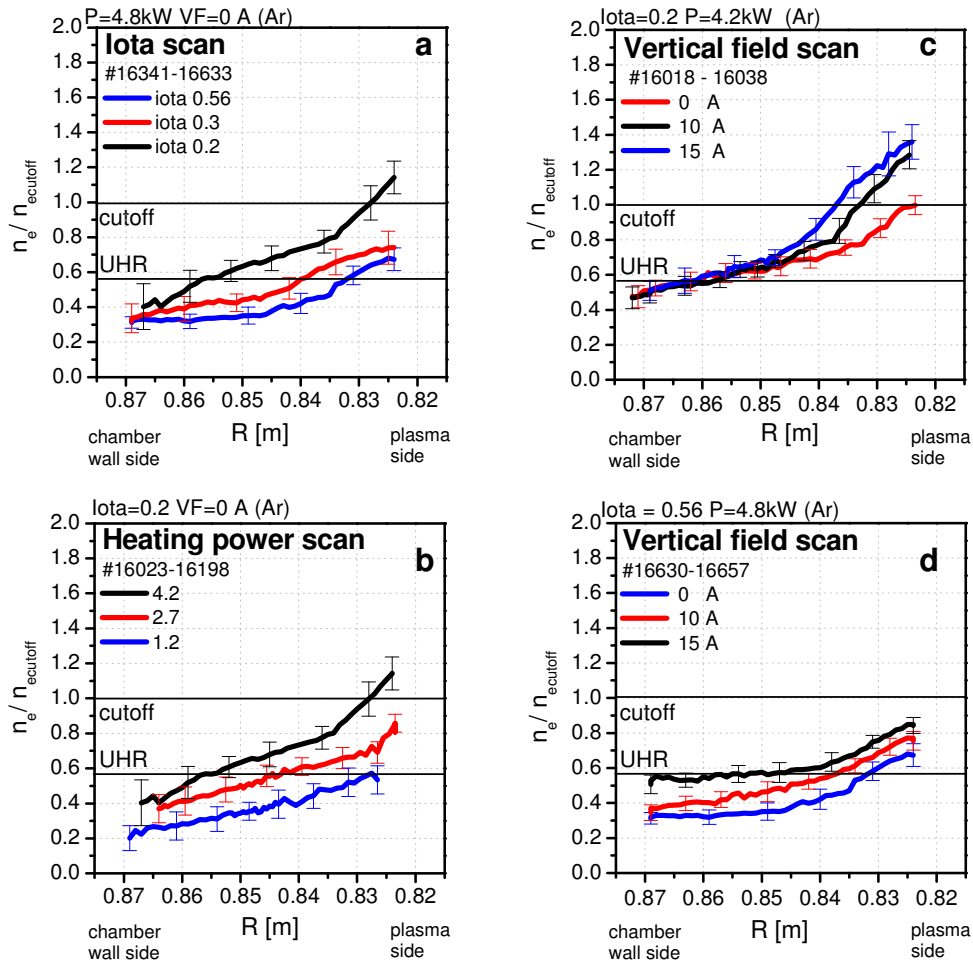


Fig.7.1. Density profile for various plasma configurations.

a - iota scan, b - heating power scan at  $i/2\pi = 0.2$ , c - vertical field scan at  $i/2\pi = 0.2$ , d - vertical field scan at  $i/2\pi = 0.56$

is also changed and the UHR layer changes its position. This change is not linear with respect to the vertical field because the coupling efficiency of the heating wave to the plasma also depends on the density profile. In addition, the density magnitude near the vacuum chamber wall should be close to zero, while on the plasma side it is varied according to discharge conditions.

Further, power sweep measurements were performed for the fixed magnetic configuration. Results of these measurements are shown in fig. 7.1(b). Here the profile with the 4.2 kW input power reaches the value of the cutoff density. However, good results of the HF measurements obtained in the range 2.4-4.8 kW.

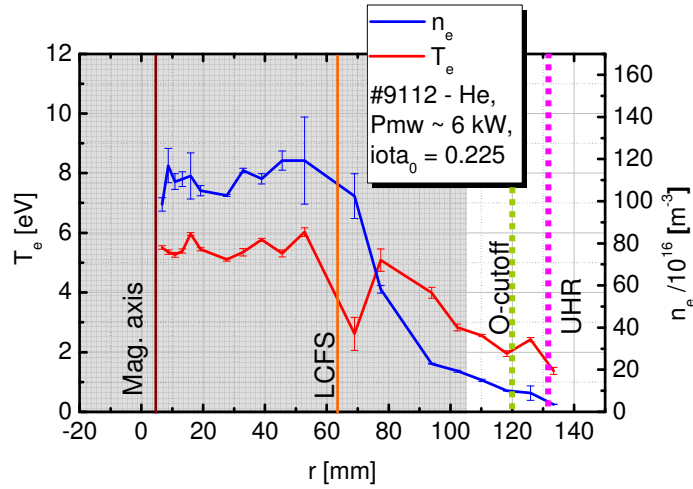


Fig.7.2. Typical density profile measured with fast Langmuir probe. The shadowed region is not accessible for HF probe measurements. Note that the O-cutoff and the UHR layer is far outside the separatrix

Thus, discharges with Ar as working gas, with  $i/2\pi = 0.2$ , power in the range 3.6-4.8 kW and current in the vertical field coils in the range 0-15 A are chosen for the HF measurements. All results presented in the following chapters are obtained in discharges with these parameters.

A typical density profile measured in conditions optimal for HF measurements is shown in fig. 7.11

### 7.1.2. Measured amplitude and phase of HF

Amplitude of different components of the wave  $E$  or  $B$ -field may be measured with different probe types, which was discussed in chapter 6.1. The best results were obtained using the 3-pin probe and two loop probes.

The main goal of the 3-pin probes is to measure the radial component of the SX-mode in the region where it tends to be electrostatic, i.e. between the cutoff and UHR layer, as described in section 3.5. The 3-pin probe is sensitive to the radial  $E$ -field ( $E_y$  in fig. 4.3,5.1). Additionally, it is wavelength-selective (chapter 6.1). Thus, this probe feels the radial short wavelength component of the  $E$ -field that occurs when X-mode propagates to the UHR layer.

The results of the amplitude measurements with 3-pin probe are shown for different heating power in fig. 7.3, and results of measurements for varied vertical field

are shown in fig. 7.4. The measurements were carried out under the discharge conditions described in the previous chapter.

There is no maximum in the first two plots in fig. 7.3 ( $P = 1.2, 1.8$  kW). This supports the correctness of our measurement regime selection made in previous chapter.

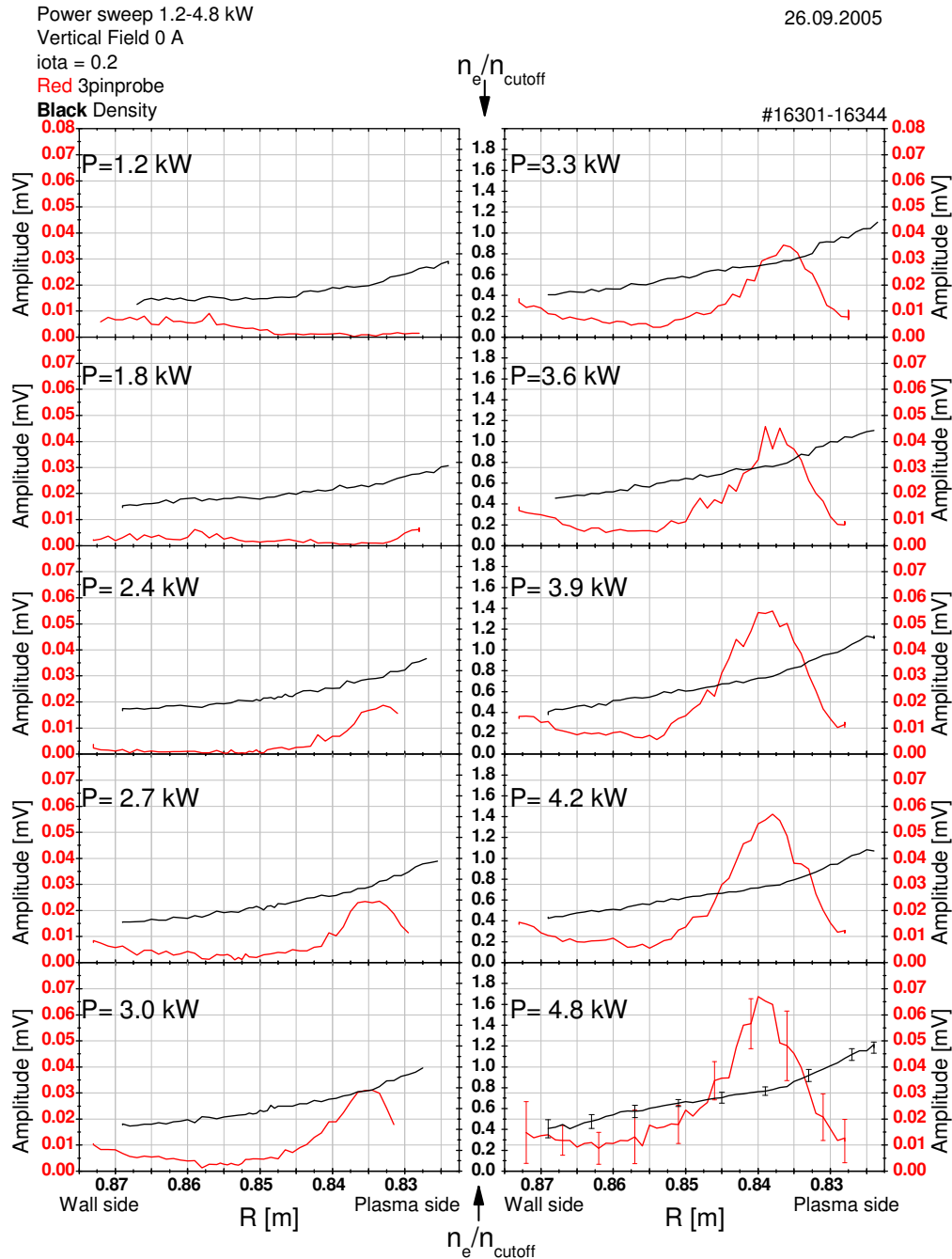


Fig.7.3. Amplitude measured by 3-pin probe (red) for different values of heating power (1.2-4.8 kW). The corresponding density profiles are also plotted, in black.

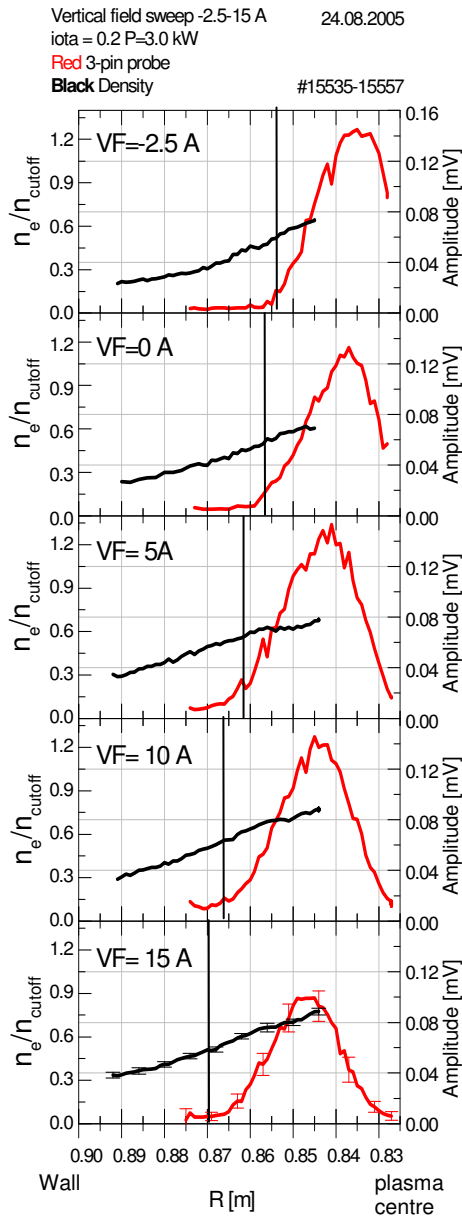


Fig.7.4. Amplitude measurements by 3-pin probe vertical field variation. Vertical marks show the UHR position.

the maximum of  $E$ -field is not at the UHR layer.

The maximum always occurs somewhere between the UHR and the cutoff, where the density  $n_{ref}$  is such that  $n_{UHR} < n_{ref} < n_{cutoff}$ . If the vertical magnetic field or heating power is changed during the measurements, it will affect the density profile and thus the position where  $n_e = n_{ref}$ .

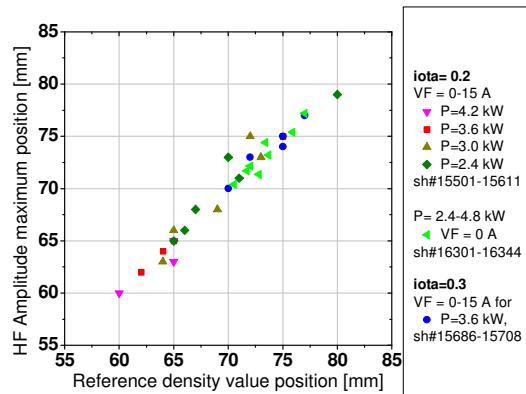


Fig.7.5. Amplitude maximum position measured by 3-pin probe versus the position of the reference density value (position shown from the outer chamber wall where  $R=910$  mm)

For the low heating power, the maximum of the HF amplitude is outside of the measurement region.

The maximum of the measured HF amplitude is not directly at the UHR layer. One reason for this is that the SX-mode starts converting to B-mode before reaching the UH resonant layer. Another and more likely explanation is that the 3-pin probe is not sensitive to wavelength smaller than the pin distance. Thus, when the wavelength of SX-mode drops below that value, a decrease of the signal is observed. Actually, SX-mode may propagate closer to the UHR layer than observed in the measurements. As it will be argued later, even in the numerical simulations

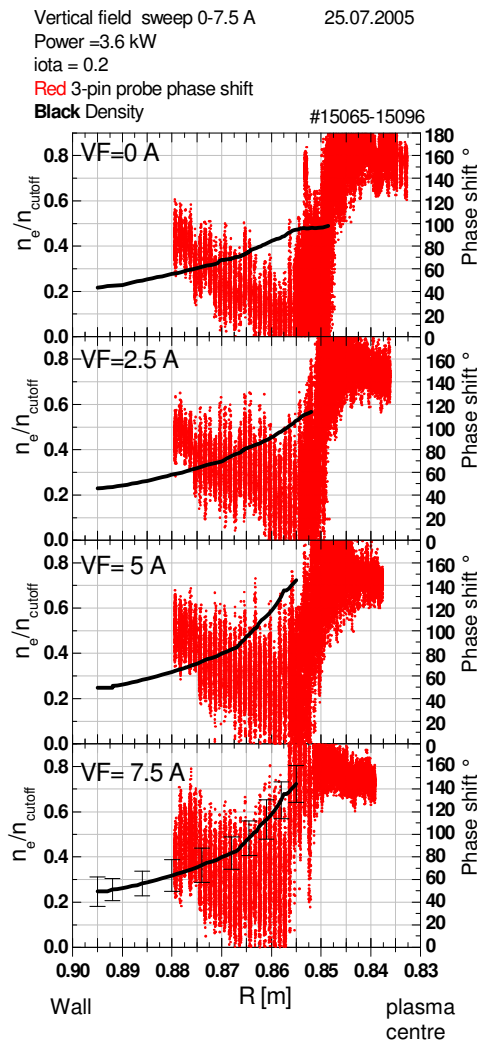


Fig.7.6. 3-pin probe phase signals.  
 Vertical field scan

from the uncertainty in localising the maximum gradient in the phase measurements of fig. 7.6. Nevertheless, a clear agreement with the UHR position is evident from fig. 7.7. This phase behaviour was confirmed by the full wave calculations (sec. 7.2).

Another important wave property is the different direction of propagation along the  $y$ -axis (or  $\nabla n_e$ ) as shown in fig. 7.8. The wave propagates in the direction of  $\nabla n_e$  in the antenna region, nearly parallel to the external magnetic field in the region of reflection from cutoff layer (or conversion to SX-mode), and outside of the plasma beyond the region of conversion. It happens due to the deflection of the wave by the

In fig. 7.5, the location of the maximum amplitude is plotted against the position where the density equals  $n_{ref}$ . A very good agreement between them is apparent. In all points of this plot  $n_{ref} \approx 0,73 \times n_{cutoff}$ . All results presented in this and the following sections are plotted together with measured density profiles to emphasize the described behaviour.

Fig. 7.6 shows the phase difference measured by the 3-pin probe and analysed using the method described in chapter 6.3. The radial phase profile has a high gradient in the region near the UHR layer. The position of this high gradient region also correlates with the density profile, but, compared to the amplitude, its position is closer to the position of UHR layer. The origin of this gradient is supposed to be the short wavelength of the SX-mode near the UHR resonance layer. The phase measurement is less dependent on the antenna sensitivity.

In fig. 7.7 the position of the maximal phase gradient is plotted over the position of UHR layer calculated from the measured density profile. Here the vertical magnetic field was varied for two cases of injected power 3.6 and 2.4 kW. The large horizontal error bars come

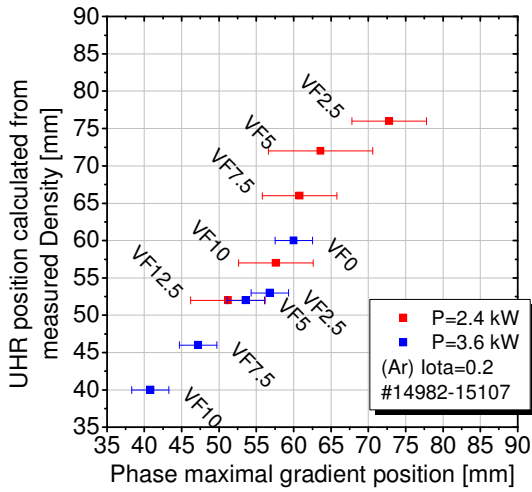


Fig.7.7. UHR-layer position over phase jump position measured in Vertical field sweep experiments, VF coils current shown by labels in [A] (position shown from the outer chamber wall where  $R=910$  mm)

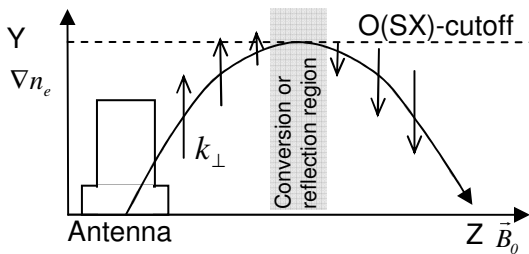


Fig.7.8 Radial propagation of the O-mode in calculation/measurement region

The other one is vertical and therefore sensitive to the magnetic field  $B_z$  of the wave, which is parallel to the direction of ambient magnetic field  $\vec{B}_0$ . In first approximation, it corresponds to the part of the X-mode component, projected on the  $\vec{B}_0$  direction.

The main goal of the loop probe measurements is to demonstrate that the behaviour of the electromagnetic waves agrees with the one predicted by full wave

cutoff layer and gives one more possibility to find such a structure in the plasma by HF probes phase measurements in various toroidal positions.

The only possibility to move toroidally the 3-pin probe was described in section 6.2.1. Unfortunately, this does not allow more than 8 cm toroidal shift of the probe, which is probably not enough to feel the difference in the phase behaviour. In fact, no significant changes were observed in phase behaviour for toroidal shifted position.

Two magnetic probes were also used. They consist of two loop antennas. As mentioned in chapter 6.1, the loop probes may be used with different orientation relative to the external magnetic field. One of them is nearly horizontal as shown in fig. 6.6. (although slightly tilted and slightly off midplane). Therefore it is sensitive to the vertical component of the wave magnetic field  $B_x$ , i.e., in the first approximation, to the O-

calculations. As it was mentioned in section 3.5 the SX-mode propagating towards the UHR layer tends to have an electrostatic nature. The  $B$ -field amplitude is very low for electrostatic modes, thus, loop probes should not be sensitive to SX-mode component close to the UHR layer.

The results of the amplitude measurements by horizontal and vertical loops are presented in fig. 7.9. The results are presented for varied input power.

The amplitude of the signal from the horizontal loop has a maximum in the region outside of UHR layer and decreases in the region between the UHR and cutoff layers. It corresponds to the decreasing of the O-mode amplitude due to its conversion into the SX-mode near the cutoff. On the contrary, the amplitude of the signal from vertical loop has a maximum after the UHR layer. This maximum corresponds to the SX-mode originating from the O-mode by means of mode conversion. Such behaviour of the signal from the vertical loop suggests that in addition to some X-mode injected by the heating antenna because of a lack of polarisation control (chapter 5.1.3) some X-mode is excited due to O-SX mode conversion process.

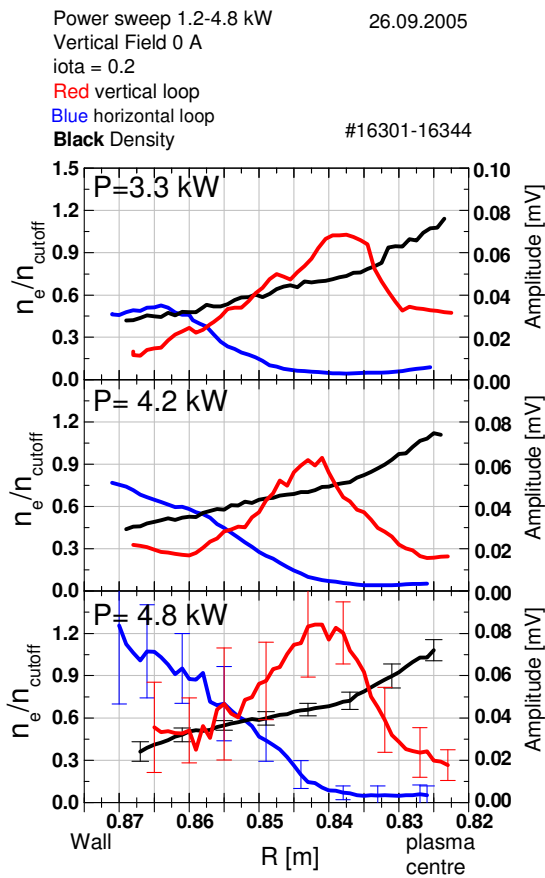


Fig.7.9. Loop probes amplitude signals

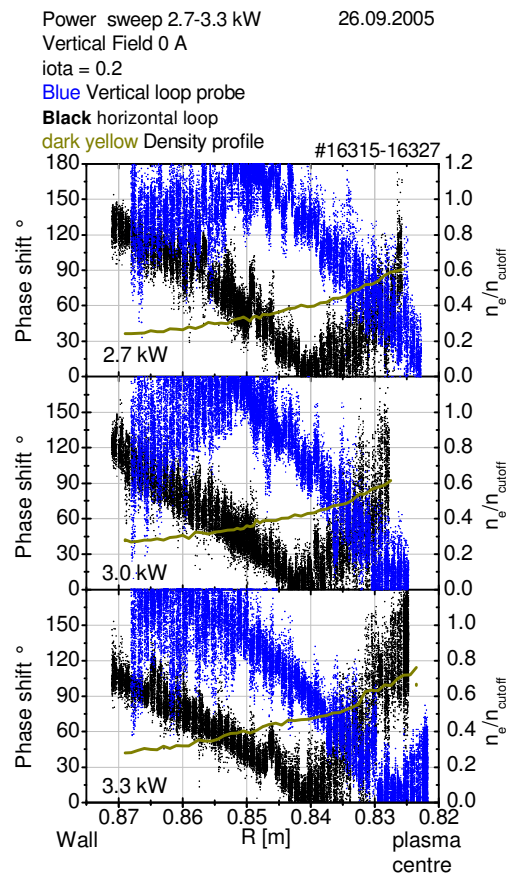


Fig.7.10. Loop probes phase shift.

The phase of the loop signals has no jumps and changes smoothly over the measurement region (fig. 7.10). The maxima and minima of the phase shift in this picture at the edges of the plot ( $0^\circ$  and  $180^\circ$ ) appear due to the calculation method described in 6.3. Thus, the phase of this mode rises (or decreases) monotonously with the coordinate.

## 7.2. Calculation and measurement comparison

### 7.2.1. Full wave calculation results

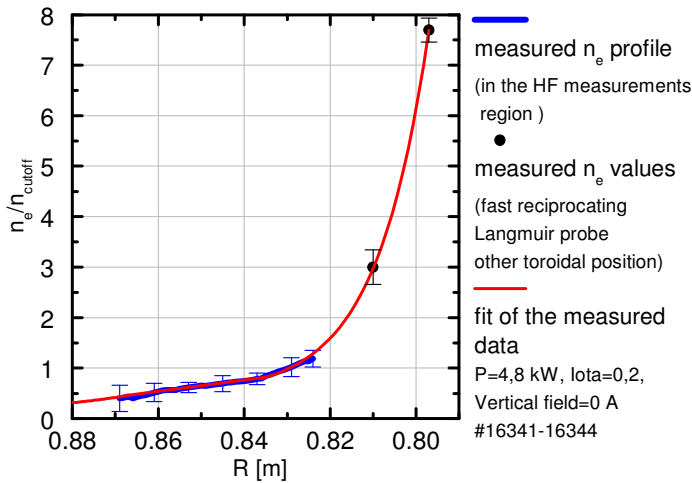


Fig.7.11. Density used in full wave calculations.

In fig. 7.11, the density profile measured from the discharge with the parameters optimal for HF measurements is shown (in blue), along with its fit (in red), two black points correspond to the density measured by fast reciprocating Langmuir probes in different toroidal position but on the same  $r_{eff}$ . The fitted curve was extended to the region inaccessible for Langmuir

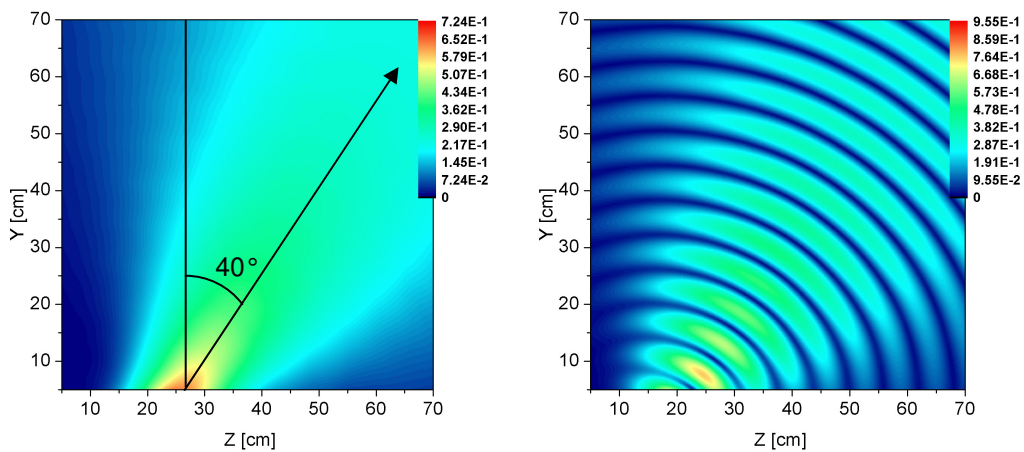


Fig.7.12. Time averaged E field(left) and snapshot(right) amplitude distribution calculated for  $\theta=40^\circ$  in vacuum



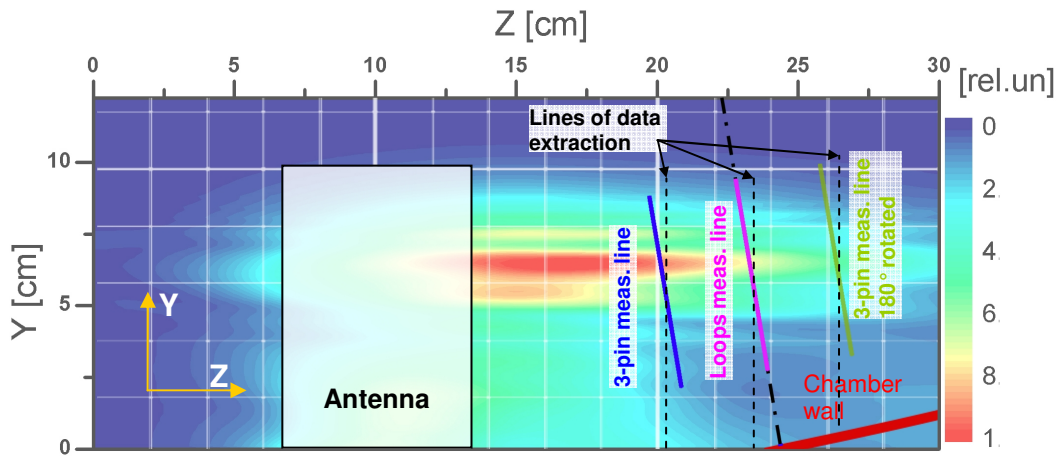


Fig.7.13. Solution region overlapped by the slot antenna geometry, top view

probes described in section 6.2.3, using the results of fast Langmuir probe measurement in other toroidal position (see sec. 2.2.2).

The source of HF in this calculation was on the bottom plane of the calculation region and it is a Gaussian beam with main lobe  $\theta_0 \sim 40^\circ$  as shown in fig. 7.12. The calculation grid was set to 300 points per vacuum heating wavelength. Solution mesh has 1300 points in Y direction and 3000 points in Z direction (see fig. 4.3).

Calculated distribution of electric field amplitude  $|E|$  and its components  $|E_x|$ ,  $|E_y|$ ,  $|E_z|$  are plotted in fig. 7.14. The calculation was performed for 11000 iterations, which correspond to 36.6 periods of HF oscillation or 15 ns of HF wave propagation. The absolute value of the  $E$ -field components is shown in these plots.

To compare the calculation results and the measured data the  $E$ -field values should be extracted from the calculations along the line, which corresponds to the measurement line in WEGA. This is a vertical line parallel to the Y-axis at Z position, which corresponds to the measurement position in the WEGA, as drawn in fig. 7.13. Field values calculated along this line are saved in an external file during one period of HF oscillation. This data is then used to calculate the amplitude and phase distribution of electromagnetic field components. Calculated profile examples are shown in fig. 7.15.

It was mentioned in 7.1.2 that the maximum of the HF amplitude measured with 3-pin probe is located between the cutoff layer and UHR layer because of the 3-pin probe wavelength sensitivity. In full wave calculations, this situation may be simulated using the numerical viscosity, which damps short wavelength waves.

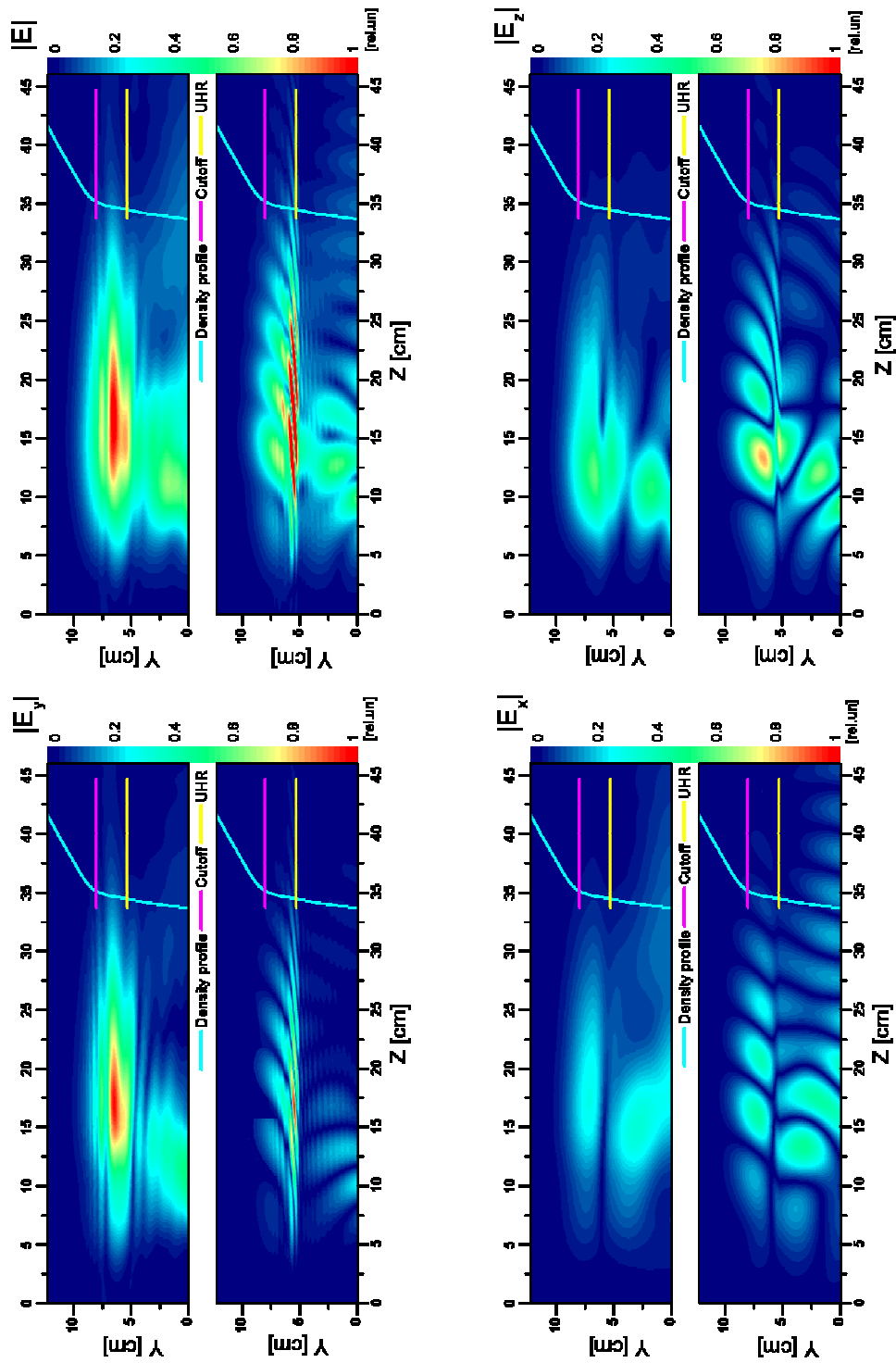


Fig.7.14. Full wave calculation results for a density profile like in fig.7.11. Top plot of each pair is a time averaged E-field pattern, while bottom plot is a snapshot.

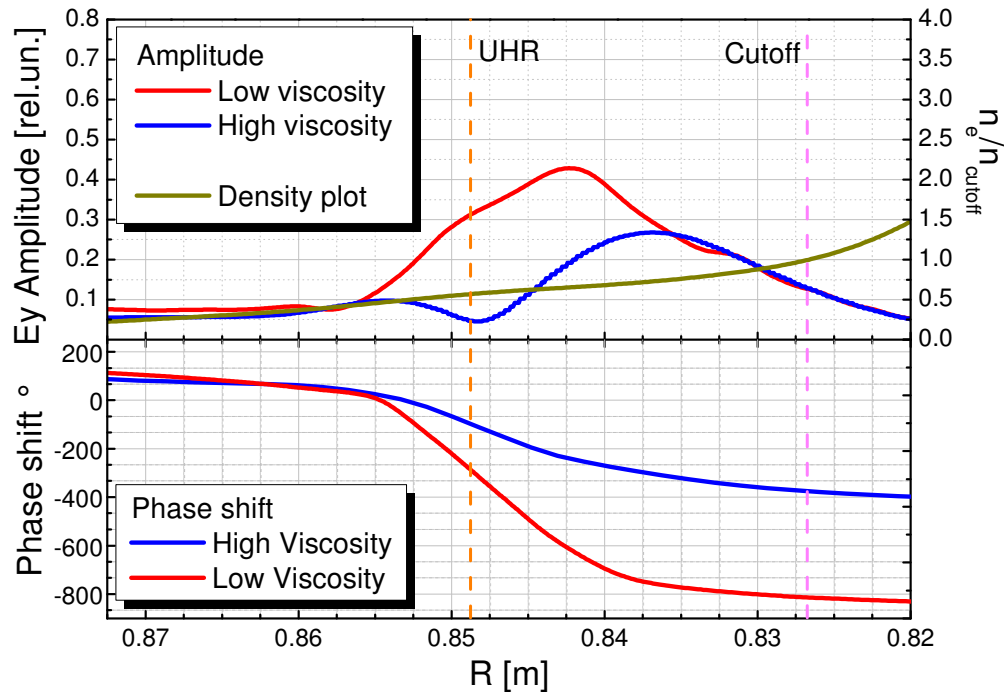


Fig.7.15. Examples of profiles extracted from full wave calculations. Numerical viscosity effect on calculated amplitude profile (top) on calculated phase (bottom)

The calculated  $E_y$  component amplitude and phase profiles for high and low numerical viscosity are demonstrated in fig. 7.15. All the other parameters in the calculations are identical. The position, width, and amplitude of the  $E$ -field maximum are changed, but it is always located between the cutoff and UHR layer.

In fig. 7.15(bottom) the phase calculated by full wave code with low viscosity is compared with one for high viscosity. The phase has a strong gradient near the UHR layer. This corresponds to a SX-mode wavelength shortening near the UHR layer.

In the high viscosity case, the wavelength calculated from phase gradient is  $\lambda \approx 2$  cm. For low viscosity, the phase gradient is even stronger because the short wavelength, which is responsible for this gradient, has much lower damping. The calculated wavelength near the UHR layer is below 1 cm.

It is clear that the wavelength is nearly the same before the UHR layer and after the cutoff, but between these two layers a significant phase shift occurs in the low viscosity case and smaller shift occurs for low viscosity.

---

### 7.2.2. Comparison of calculations and measurements

The data extracted along line as shown in fig. 7.13 is compared with the measured amplitude and the phase distribution. The similarity with calculated profiles is found in amplitude measured by 3-pin probe and loop probes.

The amplitude measured by 3-pin probe is compared with the  $E_y$  amplitude distribution obtained from the full wave calculations. The measured and calculated profiles are in good agreement (fig. 7.16.)

Moreover, shifting the UHR and cutoff positions in calculations also leads to shifting of the calculated amplitude maximum position, as it happens in the measurements (see fig. 7.5).

The electromagnetic waves behaviour investigated by loop probes may also be compared with the calculations. The loop probes are sensitive to the magnetic field component perpendicular to the loop plane. The signals from these probes were compared with the  $B$ -field components. These are presented in fig. 7.17. Here, the amplitude profile measured by the horizontal loop is compared with the  $B_x$  component, the amplitude from the vertical loop is compared with  $B_z$  component, showing good agreement.

A decrease of the  $B_x$  amplitude towards the cutoff layer and increase of the  $B_z$  component between the UHR and Cutoff layers corresponds to the conversion from O- to SX-mode near the cutoff.  $B_z$  component represent the electromagnetic part of X wave in the region of O-SX conversion before it comes close to UHR layer and becomes fully electrostatic.

Increasing of  $B_z$  amplitude in the region between the UHR layer and the chamber wall corresponds to the FX wave which is reflected by the R-cutoff. It can be minimized by adjusting the polarization as described in section 4.2.6.

An important common property of all the measured and calculated amplitude profiles is a reduction of the amplitude of the HF waves beyond the O-cutoff layer. This is supported by the theory described in previous chapters. Indeed, the only modes, which may propagate in the overdense plasma, are the Bernstein-mode and, to some extent, the SX-mode. The SX-mode has a cutoff on the L-cutoff layer, which in case of the WEGA is very close to the O-cutoff because of very steep density profile in this region. The B-mode may propagate into the dense plasma but our measurements system has low sensitivity to the waves with wavelength comparable with the Larmor radius of electrons. However, in 2D full wave calculations the temperature term was not included.

---

The comparison of the calculated and the measured phase behaviour is complicated due to the high fluctuation level and the phase extraction method used. Nevertheless, phase measured by 3-pin probe along with calculated phase of  $E_y$  component share common feature, they both have strong phase gradient near the

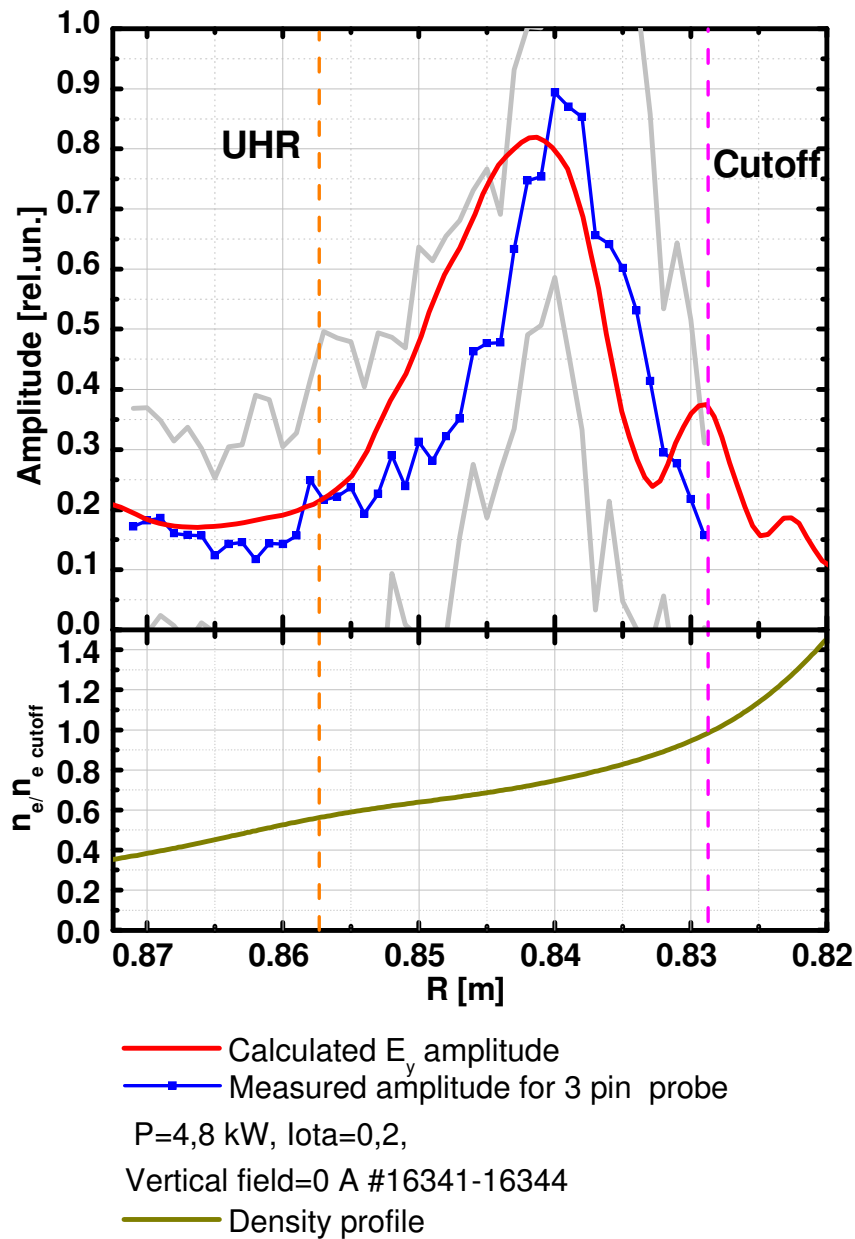


Fig.7.16. Comparison of the amplitude profile measured by 3-pin probe with the  $E_y$  distribution calculated by full wave code. Density profile used in the calculations is taken from the same measurements as amplitude profiles. Grey curves represent the measurement precision

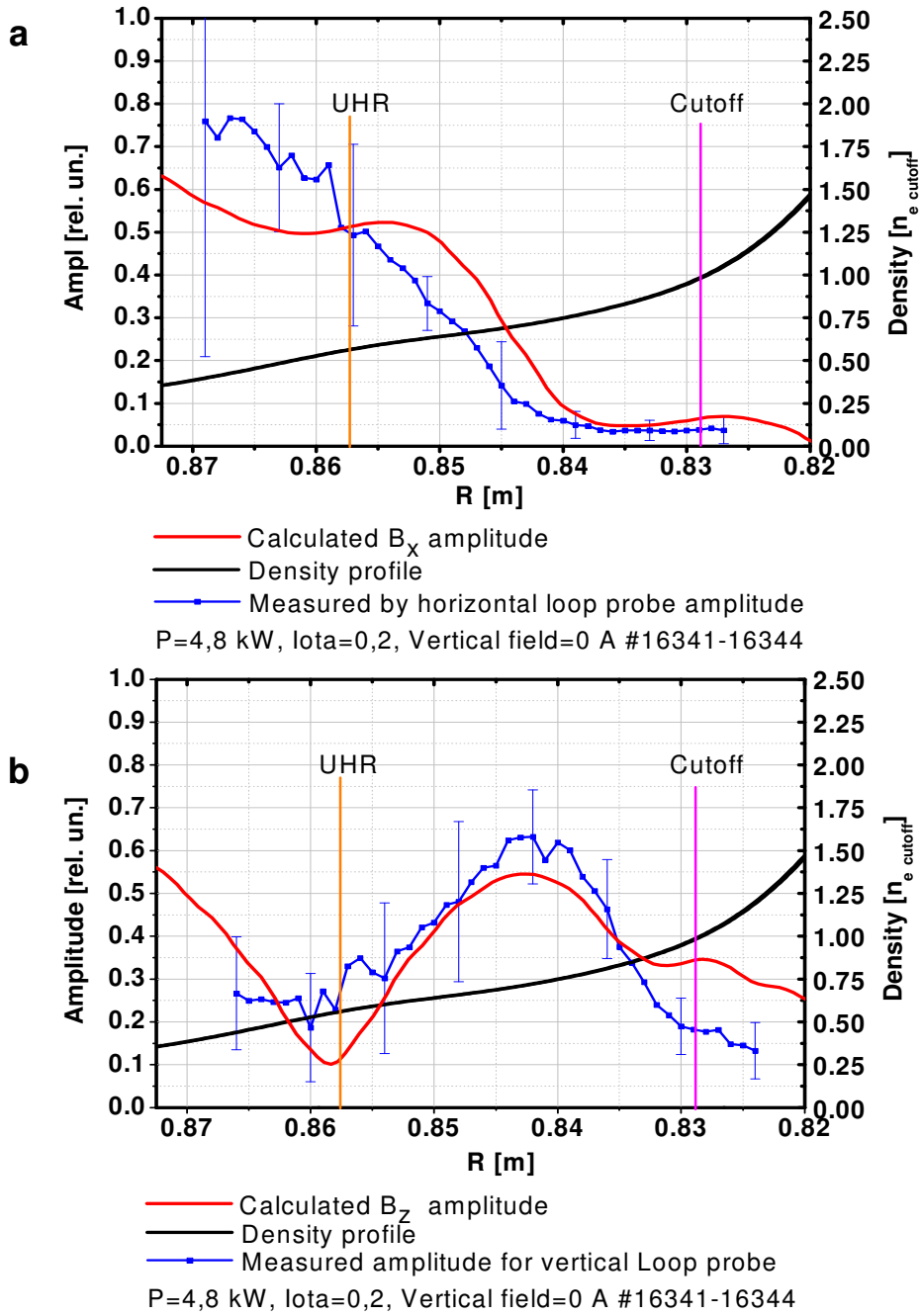


Fig.7.17. Comparison of the amplitude profile measured by horizontal loop(a) and vertical loop(b) with  $B_x$  and  $B_z$  magnetic field components distribution calculated by the full wave code. Like in fig. 7.16, the density used in calculations is taken from the same measurements as for the amplitude profiles (fig. 7.11).

Vertical field 0 A #15065-15070

Power =3.6 kW  $\iota = 0.2$

Red 3-pin probe phase shift

Yellow Density

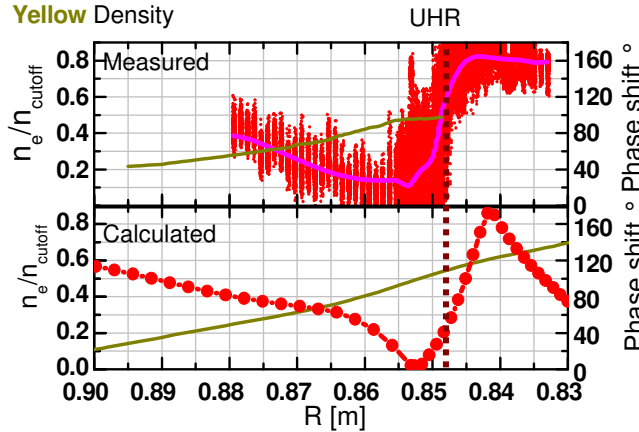


Fig.7.18. Measured and calculated phase behaviour comparison.

Phase measured by 3-pin probe (top)

Phase calculated using full wave code (bottom)

layer, as shown in fig. 7.18. This fact points to the shortening of the electrostatic wave wavelength in the resonance region.

The wavelength for the phase calculated by the full wave code near the UHR layer reach the value below 1 cm, which is more than ten times smaller than the vacuum wavelength.

The HF measurements give the minimal wavelength near UHR layer  $\lambda \approx 0.8$  cm. This result is consistent with the full wave calculations.

### 7.3. Conclusions from the measurements

Results of the comparison between the measurements and calculations point to existence of the resonance near the UHR layer in WEGA plasma. Unfortunately, the electrostatic Bernstein mode can not be observed because they have very short wavelength of the order of the electron Larmor radius. This is far too small for the sensitivity of our instruments.

However, good agreement of measured and calculated data for electrostatic and electromagnetic waves is found. The amplitude shows growth of the wave's field amplitude near the UHR, and decrease of the EM waves amplitude beyond the cutoff layer. The decrease of the wave amplitude measured by horizontal loop probe and its simultaneous increase for the vertical loop probe directly indicates the existence of O-SX conversion.

The measured phase behaviour also points to the existence of the UH resonance and of a short wavelength electric field near the resonant layer, which may couple to the EB-wave.





## **8. Conclusions**

The ECR heating in the WEGA stellarator was investigated in this work. The ECR heating efficiency could be strongly enhanced. There are clear evidences that the improvement of the plasma parameters is due to the optimisation of the ECR-antenna for the OXB-mode conversion process. This conjecture is supported by full wave calculations of wave distribution in the plasma and by results of wave investigation by HF probes in the heating antenna vicinity.

### ***8.1. Calculations***

The full wave calculation, performed in this work, shows the OXB mode conversion in the WEGA plasma. Moreover, it was shown that the efficiency of the of the mode conversion could be optimized by means of the angle  $\theta_0$  of the launched wave vector  $\vec{k}$  with respect to the external magnetic field vector  $\vec{B}_0$ . The optimal angle for the O-SX conversion process is found near  $40^\circ$ . This allows to improve the plasma heating efficiency on WEGA by heating the overdense plasma core with the EB-wave. However, the efficiency of mode conversion based on full wave calculations is below 25% of injected power. To increase the efficiency of the mode conversion the angular beam width and polarization of the inserted wave should be optimized. This task technically is not feasible due to the low heating frequency and space limitation on the WEGA. The wavelength of the heating wave is comparable with the plasma dimensions. Nevertheless, heating antenna modification has successfully been performed to launch the heating wave under optimal  $\vec{k}$  direction.

### ***8.2. Antenna design***

The new antenna design makes the OXB heating scheme in WEGA after the optimization of the injection angle. During the heating antenna improvement process three types of antennas have been designed and tested. Improvement of the heating efficiency was observed in each modification step.

---

---

The achieved plasma density increased from the density near the cutoff value with hollow profiles when the straight waveguide was used as an antenna, up to twelve times the cutoff density with peaked profiles when the optimized double slot antennas was used.

The electron temperature of the plasma also increased from 5 eV for the straight waveguide to 12 eV for the double slot antenna configuration. The temperature profile also became less hollow.

Other parameters measured with fast Langmuir probes and other diagnostics indicated the desired plasma heating improvement (see *table.1* in section 5.2.1). All diagnostic indications point toward the heating of overdense plasmas, which is possible with the Bernstein mode only. The existence of mode conversion has been proven by the full wave calculations and high frequency measurements.

Thus, the double slot antenna design was chosen for the ECR heating in the WEGA plasma. This type of antenna is used now for both the 6 kW and the 20 kW magnetron.

### **8.3. HF measurement system**

A high frequency probe system with additional Langmuir probes was developed and used for investigation of HF wave behaviour near the heating antenna.

With a 3-pin probe the features of the resonance on the UHR layer has been found. The increase of wave amplitude and decrease of wavelength of the wave has been demonstrated. The wavelength of the wave could be calculated from the phase, which is measured using a set of down sampling mixers.

Additionally, electromagnetic wave behaviour has been analyzed using loop type probes. They allow to measure the radial profiles of the amplitude and phase of the O- and X- polarized components of the wave. Decreasing of the O-mode and increasing of the SX-mode amplitude towards the O-cutoff layer indicate the predicted O-SX transformation in the region of O-mode cutoff.

The Langmuir probe set is used in parallel with the HF probes. It helps to localize the UHR and cutoff layers in the antenna vicinity region, and to compare its positions with the positions obtained from HF measurements.

The described wave behaviour has been found in the WEGA plasma, which supports the assumption of both the O-SX conversion and the resonance for the SX-mode at the UHR layer.

---

#### **8.4. OXB existence**

The agreement of measured and calculated data for electrostatic and electromagnetic waves is found. Decreasing of the wave amplitude measured by horizontal loop probe and the simultaneous increasing of it for the vertical loop probe toward the cutoff layer directly indicate the existence of O-SX conversion.

Additionally, comparison of measurements and calculations points to the existence of the resonance near the UHR layer in WEGA plasmas. Unfortunately, the electrostatic Bernstein mode can not be observed directly. Probably some improvements of the measurement system should be made to increase the sensitivity in order make accessible the waves with wavelengths comparable with the electron Larmor radius.

However, the 1D full wave calculations show that the EBW will develop at the UHR layer from the incoming SX-mode. Measurements and calculations show that conditions in the WEGA plasma are such that the SX-mode mode should be converted to the Bernstein mode near the UHR layer. This shows that conditions for obtaining EBW are satisfied.

In addition, the improvement of plasma parameters indirectly indicates that the centre of the plasma is heated by EB waves, since no other modes propagate into the overdense region.

---



## 9. Appendix

### **Appendix A** **DC brake**

The DC brake is nothing else than just a throttle waveguide connection with thin dielectric put in between the flanges. The flanges have resonant cavities (fig. 9.1), the length and distance of the cavities is such that the travel path of the wave from the point  $A_{1,2,3}$  to  $B_{1,2,3}$  and back (marked by blue lines) is equal to  $n\lambda$  where  $n$  is an integer. In this case reflection of HF in the point of waveguides connection ( $A_1$ ) is minimal and usually below 0.5%. In addition, the absorber is put in between the shield and WEGA side flange. It absorbs the residual emission of the HF (shown by orange line). A 2 mm Teflon plate is used as an isolator. The travel path of the wave is calculated taking into account the distance it travelled in Teflon medium.

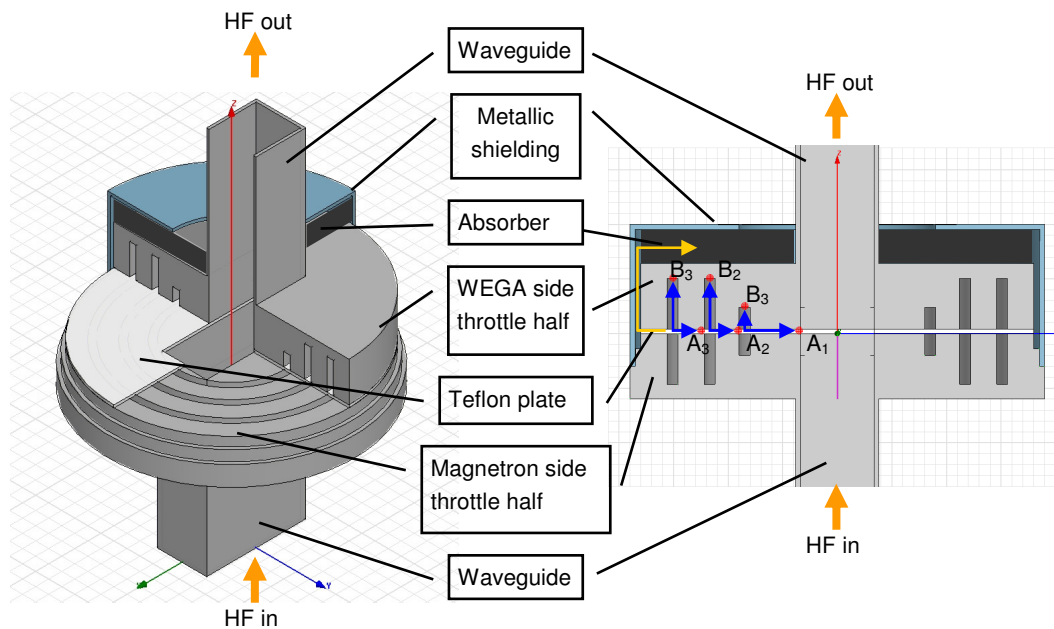


*Fig.9.1. 3D model used for design of the DC brake in HFSS code.*

## Appendix B

### Vacuum window

The new vacuum window is made of AlN ceramic. The main advantage of this material is very high thermal conductivity coefficient that is comparable with the one of cooper. It allows very effectively cooling down the window during high power operation.

To minimize the reflected power from the window its thickness should be equal to half the wavelength of the 2.45 GHz wave in the circular waveguide (Ø86.3 mm) filled with AlN.

To calculate this wavelength the permittivity  $\epsilon$  of this ceramic is needed for our heating frequency. A simple measurement system was assembled for this purpose. The principle of the measurement is based on that fact that the wavelength in the dielectric is a factor of  $\sqrt{\epsilon}$  less than in vacuum. The measurement method is described in Appendix B1.

The Measured permittivity value of the AlN is equal to 8.4 for 2.45 GHz frequency. The thickness of the half wavelength vacuum window in this case is 21.5 mm. The dependence of the HF reflected power on the vacuum window thickness

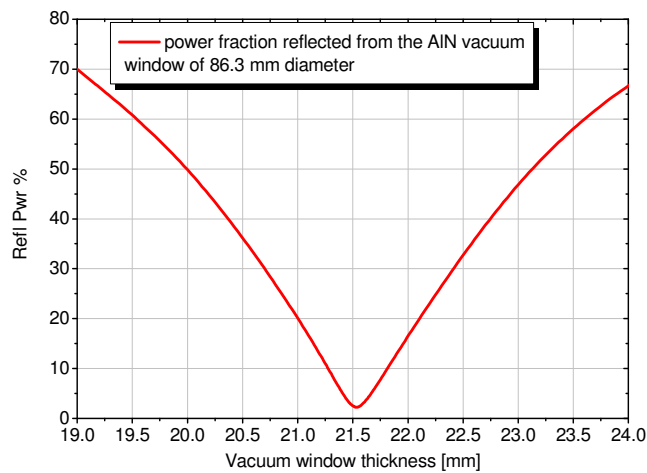


Fig.9.2. Dependence of the reflected power from AlN vacuum window on the window thickness  
Calculated with HFSS code for 2.45 GHz.

calculated with the HFSS code is presented in fig. 9.2. It is clear that the vacuum window thickness of 21.5 mm corresponds to the minimum of reflected power.

The vacuum window is mounted in a copper flange, which is actively cooled with water. Cooling of the flange is needed because the AlN ceramic and copper have a different factor of the thermal expansion. Due to this difference, the flange extends more than the ceramic inside, which results in a vacuum leakage during high power operation.

### Appendix B1

#### AIN Permittivity measurement

As mentioned before of the measurement based on wavelength dependence on the permittivity  $\varepsilon$  of the dielectric in which the wave is propagating. To measure the permittivity of AIN, a simple measurement system was assembled shown in fig. 9.3.

The waveguide is powered by the generator at the frequency of 2.45 GHz. The wave travels to the plunger position where partly develops further along the main waveguide and partly turns to the plunger part. In the plunger, it passes through the dielectric sample twice: once before it is reflected from the metallic surface of the plunger and once after reflection. If the travelling path of the wave in the plunger canal is equal to the integer number  $n$  of wavelengths then the waveguide line is matched and the signal read by a spectrum analyzer on the output of the system is maximal. In the opposite case if this path is equal to  $(2n+1)\cdot\lambda/2$  the situation is mismatched and the output signal is minimal. Knowing the distance shown at the picture as  $h$  and sample thickness  $d$  it is possible to calculate the permittivity  $\varepsilon$  of the sample material.

$$\varepsilon_1 = \left( \frac{c}{2df} - \left( \frac{h}{d} - 1 \right) \sqrt{1 - \left( \frac{c}{2af} \right)^2} \right)^2 + \left( \frac{c}{2af} \right)^2 \quad (38)$$

Here  $f$  – frequency of the wave,  $a$  – the waveguide larger wall length, (this length defines the critical wavelength for the waveguide  $\lambda_{cr} = 2a$ ),  $c$  – light velocity in vacuum.

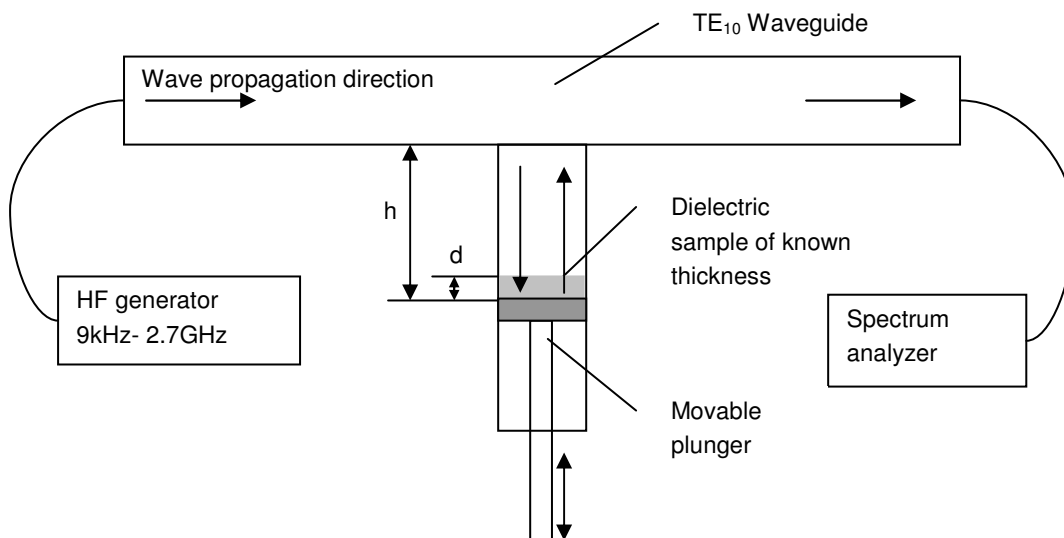


Fig.9.3. The scheme of the permittivity measurement arrangement

During the measurement, a frequency may be found for which the matching is the best for fixed plunger position. Alternatively, position of the plunger with the sample put on it may be found, where the matching is the best for 2.45 GHz. Both methods were used. Additionally, the HFSS code has been used to verify the measured value.

For the testing of this measurement system, the Teflon sample permittivity was measured which value is well known. The measured value corresponds to the reference with a precision below 1%.

### **Appendix C**

#### **Code description**

A solution of Maxwell's equations for the propagation of electromagnetic waves in cold plasma is needed. The first two equations of interest for this problem are,

$$\nabla \times \vec{E} = -\frac{1}{c} \frac{\partial \vec{B}}{\partial t}, \quad \nabla \times \vec{B} = \frac{1}{c} \frac{\partial \vec{E}}{\partial t} + \frac{4\pi}{c} \vec{j}, \quad (39)$$

where the plasma effects will be included in the response of the current density  $\vec{j}$  to the electric field  $\vec{E}$ .

Restricting to a two-dimensional slab model, with ordinary mode propagation in the Y-Z plane and no gradients allowed in the X direction. A simplified set of equations results for the waves magnetic field,

$$\frac{\partial B_x}{\partial t} = c \left( \frac{\partial E_z}{\partial y} - \frac{\partial E_y}{\partial z} \right), \quad \frac{\partial B_y}{\partial t} = -c \frac{\partial E_x}{\partial z}, \quad \frac{\partial B_z}{\partial t} = c \frac{\partial E_z}{\partial y}, \quad (40)$$

and for the electric fields,

$$\frac{1}{c} \frac{\partial E_x}{\partial t} = \frac{\partial B_z}{\partial y} - \frac{\partial B_y}{\partial z} - \frac{4\pi}{c} j_x, \quad \frac{1}{c} \frac{\partial E_y}{\partial t} = \frac{\partial B_x}{\partial z} - \frac{4\pi}{c} j_y, \quad \frac{1}{c} \frac{\partial E_z}{\partial t} = -\frac{\partial B_x}{\partial y} - \frac{4\pi}{c} j_z, \quad (41)$$

The plasma current  $\vec{j}$  depends on the density and magnetic field. The current for a cold magnetized plasma is taken from A.K.Ram and S.D.Shultz [44],

$$\vec{j} = -i\omega\epsilon_0\vec{\chi}E, \quad (42)$$

where the  $\epsilon_0$  is the dielectric constant of free space and  $\vec{\chi}$  is the susceptibility tensor:

$$\vec{\chi} = \frac{-\alpha^2}{1-\beta^2} \begin{pmatrix} 1 & -i\beta_c & i\beta_s \\ i\beta_c & 1-\beta_s^2 & -\beta_s\beta_c \\ -i\beta_s & -\beta_s\beta_c & 1-\beta_c^2 \end{pmatrix}, \quad (43)$$



where:

$$\alpha^2 = \frac{\omega_{pe}^2}{\omega^2}, \quad \beta = \frac{\omega_{ce}}{\omega}, \quad \beta_c = \beta \cos \Psi, \quad \beta_s = \beta \sin \Psi, \quad (44)$$

where  $\Psi$  is the angle between  $\vec{B}_0$  and the Z axis. In our case this angle is equal to  $0^\circ$  and the simplified tensor is,

$$\vec{\chi} = \frac{-\omega_{pe}^2}{\omega^2 - \omega_{ce}^2} \begin{pmatrix} 1 & -i \frac{\omega_{ce}}{\omega} & 0 \\ i \frac{\omega_{ce}}{\omega} & 1 & 0 \\ 0 & 0 & 1 - \frac{\omega_{ce}^2}{\omega^2} \end{pmatrix}, \quad (45)$$

Using (42) and (45) the components of  $\frac{\partial j}{\partial t}$  may be written as,

$$\frac{\partial j_x}{\partial t} = -n_e \frac{e^2}{m_e} E_x + j_y \omega_{ce}, \quad \frac{\partial j_y}{\partial t} = -n_e \frac{e^2}{m_e} E_y - j_x \omega_{ce}, \quad \frac{\partial j_z}{\partial t} = -n_e \frac{e^2}{m_e} E_z, \quad (46)$$

The code solves the system of equations (41), (40) and (46) using a Finite-Difference, Time-Domain method (FDTD).

From Maxwell's equations it can be seen that the time derivative of the  $E$ -field is dependent on the curl of the  $B$ -field. The new value of the  $E$ -field is depending on the old value of the  $E$ -field (time derivative), and dependent on the difference in the  $E$ -field on either side of the  $B$ -field point (space derivative). In FDTD technique the derivatives are replaced by the finite differences of  $E$  and  $B$  in time and in space [50],

$$\frac{\partial E}{\partial t} \rightarrow \frac{\mathbf{E}_{t+dt} - \mathbf{E}_t}{dt}, \quad \frac{\partial E}{\partial i} \rightarrow \frac{\mathbf{E}_i - \mathbf{E}_{i+di}}{di}, \quad i = x, y, z, \quad (47)$$

where  $dt$  and  $dx$  define the time and space resolution of calculations and  $E_{t,i}$  is the value of electric field in discrete points of the calculation. The same is true for the  $B$ -field. This technique may be used in 1-dimensional (1D) calculations as well as in the 2D and 3D case.

In case of the WEGA, the 2D technique was used and the system is solved in two-dimensional YZ slab system bounded with absorbers. There is no variation along the X coordinate.

The magnetic and electric fields have three components along X,Y and Z axis. The X-component is perpendicular to the plane of propagation. In the particular case of

vacuum propagation with the source  $E$ -field polarized in the  $YZ$  plane, the magnetic field has only a  $B_x$  component and the electric field only  $E_y$  and  $E_z$  components.

The code is divided into three main parts; the first and third are the interface parts. In the first part, the variables and their initial values are defined and initial data such as electron density profile, magnetic field profile, and source amplitude and phase distribution are read from external files. In the third (last) part after the last iteration, the calculated data are stored in files for further processing.

The most important second part of the code contains the solving of the system of the above equations. It consists of a few modules. The first module defines the antenna source term along a certain “source line” in the solution region. Usually this is the border between the absorber region and solution space (fig. 4.3). The source is defined by the amplitude and phase distribution of  $E$ (or  $B$ )-field components along this line, which corresponds to the antenna aperture. The amplitude of the source is rising in time from zero to its maximum value during several periods of oscillation to provide a quasi-monochromatic excitation. Otherwise, transients occur at the beginning of the calculation, which distort the real wave propagation picture since different frequency components propagate with different velocity in magnetized plasmas.

The  $E$ -field -  $\mathbf{e}[\mathbf{y}][\mathbf{z}]$ ,  $B$ -field -  $\mathbf{b}[\mathbf{y}][\mathbf{z}]$  and  $j$  -  $\mathbf{j}[\mathbf{y}][\mathbf{z}]$  matrixes are initially filled with zeroes. The components of the fields and currents are stored in the matrixes using the odd and even indices of the grid points. For example the  $E_x$  component is stored as  $\mathbf{e}[2\mathbf{y}][2\mathbf{z}]$  in the matrix where  $\mathbf{y}$  and  $\mathbf{z}$  are the coordinates.  $E_y$  is stored as  $\mathbf{e}[2\mathbf{y}+1][2\mathbf{z}]$  and  $E_z$  as  $\mathbf{e}[2\mathbf{y}][2\mathbf{z}+1]$  so one matrix is used for all three components of the electric field. The same scheme is used for magnetic field and current.

The spatial resolution of the solution is defined by the number of grid points for one wavelength  $\lambda$  of the HF wave in vacuum -  $\mathbf{n\_period}$ . In this way the distance between the grid points in the numerical solution  $\mathbf{dy}$ ,  $\mathbf{dz} = \lambda/\mathbf{n\_period}$  defines the dimensions of the experimental geometry<sup>25</sup>.

In the calculations, dimensionless units are used. The time step is set to  $\mathbf{dt} = \mathbf{dy} = 1/\mathbf{n\_period}$ . Consequently the velocity of propagation in the numerical grid is  $\mathbf{v}_{prop} = \mathbf{dy}/\mathbf{dt} = 1$ . In a vacuum, the wavelength  $\lambda$  is  $\mathbf{n\_period}$  grid points. The external

---

<sup>25</sup> The  $\mathbf{dy}$  and  $\mathbf{dz}$  values are needed to import the experimental density profile, magnetic field profile and antenna into the calculations. In the particular case of WEGA the 2.45 GHz frequency corresponds to 12.245 cm wavelength. Usually the  $\mathbf{n\_period}$  from 300 to 700 points is used which means from 25 to 57 point per 1 cm of real space.

---

magnetic field dependence is included in the cyclotron frequency  $\omega_{ce}$  and is normalized to the wave frequency  $\omega$ . The density  $n_e$  is normalized to the cutoff density.

Finally, the following system is solved in dimensionless units in the second part of the code.

Plasma currents:

$$\begin{aligned}\partial j_x &= -4\pi^2 \cdot n_e E_x \partial t + 2\pi \cdot j_y \omega_{ce} \partial t, \quad \partial j_y = -4\pi^2 \cdot n_e E_y \partial t - 2\pi \cdot j_x \omega_{ce} \partial t, \\ \partial j_z &= -4\pi^2 \cdot n_e E_z \partial t.\end{aligned}\quad (48)$$

Magnetic fields:

$$\partial B_x = \partial E_z - \partial E_y, \quad \partial B_y = -\partial E_x, \quad \partial B_z = \partial E_x. \quad (49)$$

Electric fields:

$$\partial E_x = \partial B_z - \partial B_y - 4\pi \cdot j_x, \quad \partial E_y = \partial B_x - 4\pi \cdot j_y, \quad \partial E_z = -\partial B_x - 4\pi \cdot j_z. \quad (50)$$

Absorbers are applied to the boundaries of the computational field (see fig. 4.3). The electric field values calculated in the absorber region are multiplied with a damping factor see. Hagness and Tavlove [51]. This factor depends on the spatial attenuation of the wave in the absorber. The quality of the absorber defines the reflected power from the wall. In our calculation, this type of absorber operates satisfactorily and the amount of reflected power can be neglected.

In the next step plasma current components  $j$  have been calculated using equation (48) and are stored in the **j**-matrix. The magnetic field components have been calculated from equation (49) and are stored in the **b**-matrix. The electric field components have been calculated from equation (50) using the data from **b** and **j**. The electric field are saved as new electric field components in **e**-matrix.

After the solving module, a numerical viscosity was applied to the **e** values to avoid infinite values, and simulate absorption in the resonant region. It contains the spatial second derivative and is proportional to  $k^2$ . When the wave reaches the resonant region  $k \rightarrow \infty$  its wavelength is decreasing and when it becomes comparable with the grid distance it is damped.

In fig. 9.4 two cases of long and short wavelength are plotted with three adjoining grid points used to calculate the damping coefficient these points illustrated by the small circles on the Y axis. The coefficient which defines the damping is calculated according to the following formula:

$$\text{Damp} \sim e[y+1][z]+e[y-1][z]-2*e[z][y]. \quad (51)$$

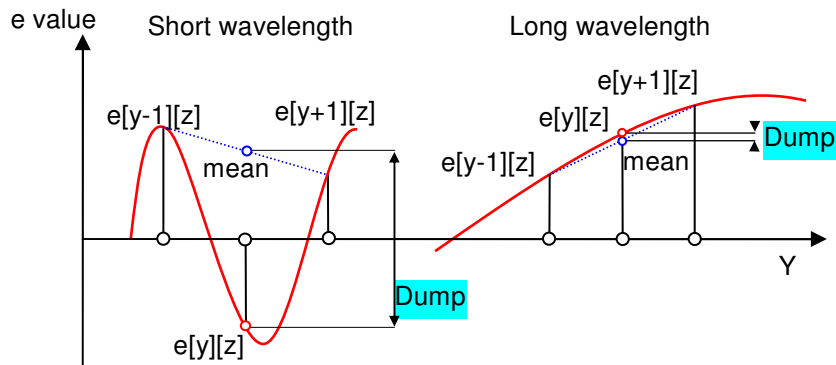


Fig.9.4. The numerical viscosity damping coefficient calculation

In the case of long wavelength  $e[z][y]$  is close to the mean value of  $e[y+1][z]$  and  $e[y-1][z]$  and the **Damp** coefficient is close to zero, but in the case of short wavelength the **Damp** coefficient rises significantly. The numerical viscosity simulates the damping by resonant conversion to the B-mode or collisional damping which is not included in the 2D code.

After application of the viscosity module the values in the matrixes contain the field patterns for the moment of time which is defined by the number of iterations  $dt \cdot \text{iteration\_steps}$ . These data can be plotted on the computer screen as a colour plot and saved in a file as an intermediate result. Then the code goes to the next iteration starting again from the source etc.

As it was mentioned in section 4.2.2, the efficiency of the O-SX conversion may be estimated in full wave calculations. It should be added that in this technique for the efficiency calculations fields from the same source should be calculated twice: once in the vacuum and once in the plasma presence. In the first case, no losses are assumed in the region bounded with absorbers. Thus, the power,  $P_{vac}$ , emitted from the calculation region to absorbers should be equal to the source power. In the second case due to the numerical viscosity the short wavelength waves are damped near UHR layer and the power emitted to the from calculation region  $P_{plasma}$  is less than in vacuum case. To calculate the power emitted into the absorbers region the pointing vector amplitude along the vacuum-absorber border has been integrated. Comparing  $P_{vac}$  and  $P_{plasma}$ , the efficiency of the coupling may be estimated  $P_{accepted} = P_{vac} - P_{plasma}$ . This value should be calculated after the  $P_{vac}$  and  $P_{plasma}$  reach the stable values. Usually it takes some 10-20 periods of source wave oscillation.

The B-mode can not be observed in the 2D code until the thermal term is not included in the Maxwell's equations. We are not including this term in 2D calculations. The reason is that for the conversion of the B-mode from XS mode a very large amount of wave oscillations is needed. This will increase the calculation duration many times. Instead of this, a one-dimensional calculation performed to show the possibility.

The 1D calculation is made along one line instead of 2D slab. The line is parallel to the density gradient and perpendicular to the external magnetic field. This is corresponding to a line parallel to the Y-axis in 2D calculations. The source is just one point positioned on one end of the line and the SX-mode is excited in this point. The excited wave propagates into the region of the UHR where it is converted into the Bernstein electrostatic mode (fig. 4.7). The calculation time for each iteration in this case is much smaller than in 2D case and the rising of the B-mode may be shown in this case in real time.

To compare the calculated data to the measured results for values of the electric and magnetic field along the line corresponding to the line of measurements in WEGA should be extracted as shown in fig. 7.13. The values of  $\mathbf{e}[\mathbf{y}][\mathbf{z}]$  and  $\mathbf{b}[\mathbf{y}][\mathbf{z}]$  matrixes (where  $\mathbf{z} = \mathbf{constant}$  and define the position of the "virtual measurement") was saved in the separate file during the one period of oscillation. This data was then used to calculate the EM - field amplitude and phase. Position of the data extraction may be varied. The data was extracted after the field distribution reaches stable state.

The values of the average field amplitude in time, as well as the snap shoots of field distributions may be extracted from the code. For comparing the measurements to calculations, the time-averaged values of the electric and magnetic fields have been used.

### ***Appendix D*** ***HFSS code***

The High Frequency Structure Simulation (HFSS) code based on the finite element method (FEM) has been used for antenna characteristics investigation and other calculations in this work.

In general, the finite element method divides the full problem space into thousands individually simple units and represents the field in each sub-unit with a local function. The final solution is the integration of the solutions over the units.

---

In HFSS code, the 3D model is automatically divided into a large number of tetrahedra. Size and quantity of elements is defined by the available memory and disk space for storage and solution of the problem matrix. This collection of tetrahedra is referred to as finite element mesh.

The code has certain limitations for example a structure under evaluation should not be too large to be solved with available resources. The structure aspect ratio should not be too large (long wire case or planar structures) in this case other methods are reasonable to use for solution. If the structure's behaviour can more easily be approximated with ray tracing techniques, for example parabolic dish antenna many 10's of wavelengths in diameter, than using of this code is not reasonable. In case of heating antenna in WEGA all these conditions are satisfied as well as in other calculations that have been performed during this work.

For the calculations of the antenna emission pattern the code uses the 3D model of the antenna in vacuum. The perfect conductive infinitely thin sheet simulates the metallic wall of the antenna as shown in fig. 9.5(left). In the picture, the blue lines show the division of the model surface into triangle surfaces. The antenna is surrounded by the bounding sphere as shown in the fig. 9.5(right) It defines the borders of the solution region. The surface of this sphere has the "radiation boundary" property it means that all EM fields coming to this boundary are irradiated to outer space. The field values on this boundary than may be used for calculation of the far field emission pattern of the antenna. The bottom magenta coloured plane has an infinite conductivity and simulates the metallic vacuum chamber wall near the antenna.

Antenna is "powered" from the circular port in the bottom in  $H_{11}$  mode.

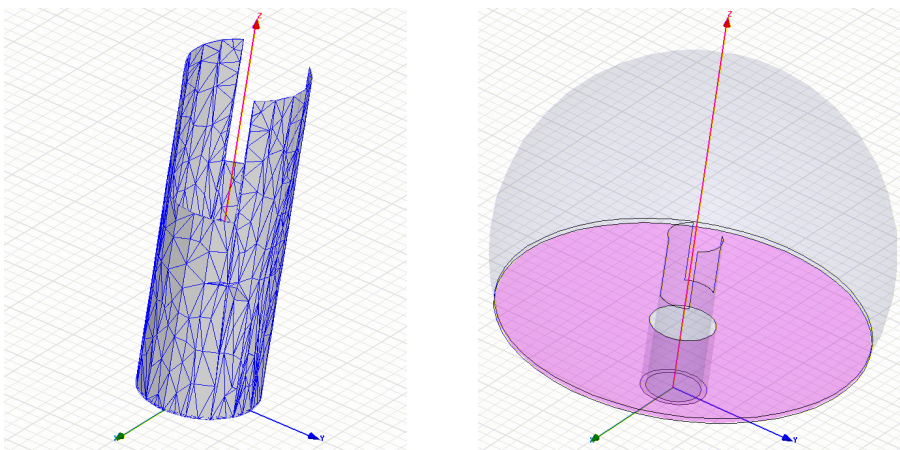


*Fig.9.5. 3D antenna model (slot antenna) with mesh plotted on it (left) and with the bounding sphere (right)*

## **Bibliography**

- [1] K.Horvath, T.Bindemann, U.Fantz, R.König, M.Otte, Y.Y.Podoba, F.Wagner  
"Characterisation of the WEGA plasma" P.Mo25
  - [2] B.Jones, et al, "Controlled Optimization of Mode conversion from Electron  
Bernstein Waves to Extraordinary Mode in Magnetized Plasma" Phys. Rev. Letters  
V.90 Nr.16, 2003
  - [3] P.C.Efthimion et al. "Application of Electron Bernstein Wave Heating and Current  
Drive to High  $\beta$  Plasmas" EX/P2-12.
  - [4] G.Taylor, et.al. "Enchased conversion of thermal electron Bernstein waves to  
extraordinary electromagnetic mode on National Spherical Torus Experiment"  
Physics of Plasmas, Vol.10, Nr.5 May 2003.
  - [5] R.A.Cairns, C.N.Lashmore-Davies "The prospects for electron Bernstein wave  
heating of spherical tokamaks" Phys. Plasmas Vol.7, Nr.10 October 2000
  - [6] I.Ryosuke et al, "Production of Over-Dense Plasmas by Launching of 2.45 GHz  
Electron Cyclotron Waves on the Compact Helical System" Plasma Fusion Res.  
Vol.81 No.7 (2005) 478-479
  - [7] F.Leuterer "Experiment with Bernstein Waves" IPP 3/102 November 1969
  - [8] F.Leuterer "CYCLOTRON HARMONIC WAVES IN AN INHOMOGENEOUS  
PLASMA-II EXPERIMENT" Plasma Phys., Vol. 14, pp 499-521, 1972
  - [9] T.Bindemann. "Line density measurements in stellarator plasmas". Wendelstein  
Seminar at the Max-Planck Institut für Plasmaphysik, March 2003
  - [10] K.Horvath "Characterisation and Optimisation of WEGA Plasmas" PhD work.
  - [11] Craig B. Markwardt, NASA/GSFC Code 662, Greenbelt, MD 20770
  - [12] P.C.Stangeby, Plasma Phys. Control. Fusion 37, 1995, p.1031.
  - [13] K.F.Mast et al, Rev. Sci. Instrum. 62, 744 (1991)
  - [14] H.P.Laqua et al. "Resonant and Nonresonant Electron Cyclotron Heating at  
densities above the Plasma Cutoff by O-X-B Mode Conversion at the W7-As  
Stellarator" Phys. Rev. Lett. 78 Nr.18, p3467 (1997)
  - [15] H.P.Laqua et al."Electron Bernstein Wave Emission from an Overdense Plasma at  
the W7-AS Stellarator", Phys. Rev. Lett. 81, Nr18, p2060 (1998)
-

- 
- [16] H.P.Laqua et.al “Electron Bernstein wave heating and emission via OXB process at W7-AS” *Plasma Phys. Control. Fusion* 41 (1999) A273-A284.
- [17] Ira B.Bernstein ”Bernstein modes” *Phys. Rev.* 109, 10 (1958).
- [18] Ira B.Bernstein “Waves in plasma in a Magnetic Field” *Phys. Review* Vol. 109, Nr 1 (1958)
- [19] Preinhaelter J. and Kopecký V. 1973 *J. Plasma Phys.* 10 1
- [20] F.Volpe, H.P.Laqua, et al. “BXO mode-converted electron Bernstein emission diagnostic” *Review of Scientific Instruments* vol. 74, No. 3 March 2003
- [21] F.Volpe “Electron Bernstein emission diagnostic of electron temperature profile” IPP-Report IPP 13/1 March 2003
- [22] L.Spitzer. The Stellarator Concept. *Physics of Fluids*, 1(4):253-264, 1958
- [23] D.Zhang, M.Otte, L.Giannone “Bolometer Results in the Long-Microwave-Heated WEGA Stellarator” Conference PLASMA2005 on Research and Applications of Plasmas combined with 3rd GPPD and 5th PFSTP, 5-9 Sep. 2005, P-2.03
- [24] Gregory S. Nusinovich “Introduction to the Physics of Gyrotrons” The Johns Hopkins University press 2004
- [25] M.K.Thumm, W.Kasperek “Passive High-Power Microwave Components” *IEEE TRANSACTIONS ON PLASMA SCIENCE*, Vol.30, Nr3 (June 2002)
- [26] S.N.Vlasov, and K.M. Likin.”Geometrical optics theory of wave transformers in oversized waveguides” book collected papers Gyrotrons, ed V.A. Flyagin 125-38. Gorky, USSR: Inst. Appl. Phys. Acad. Sci. USSR.
- [27] M.D.Foegelle “Antenna Pattern Measurement” *Compliance Engineering* 768CE.qxd jp.1
- [28] D.E.Post et al., *Atomic Data and Nuclear Data Tables* 20, 397-439 (1977).
- [29] P.C.Stangeby, *The Plasma Boundary of Magnetic Fusion Devices*, Bristol: Institute of Physics Publ.(IoP), 2000, pp. 130-145.
- [30] S.Ferrando i Margalet, W.A.Cooper, F.Volpe, F.Castejón “Electron Cyclotron Current Drive Compensation of the Bootstrap” 15th International Stellarator Workshop 2005 October 3 - 7, 2005
- [31] H.P.Laqua, H.J.Hartfuss “Electron Bernstein Wave Emission from an Overdense Plasma at the W7-AS Stellarator” *Phys.Rev.Letters*, Vol.81, Nr.10, (1998)
- [32] H.P.Laqua, V.Erckmann, F.Volpe, H.Maassberg, ”Electron Bernstein wave heating and current drive in overdense plasmas at the Wendelstein7-AS-Stellarator”. 29th EPS Conference on Plasma Phys. and Contr. Fusion Montreux, 17-21 June 2002 ECA Vol. 26B, D-5.010 (2002).
-



- [33] K.Nagasaki et al. "Electron Bernstein wave heating in Heliotron Systems". Proceedings of the EC12. Aix-en-Provence. France (2002)
- [34] K.Nagasaki et al. "Measurement of Absorption and Scattering of High Power EC waves in Heliotron J" Institute of Advanced Energy, Kyoto University, Japan.
- [35] H.Sugai et.al "Electron Heating by Oblique Injection of Ordinary Mode into Overdense Plasma". Journal of the Physical Society of Japan Vol. 56, No. 11, pp.779-3782 (November, 1987).
- [36] H.Sugai "Mode Conversion and Local Heating below the Second Electron Cyclotron Harmonic" Phys. Rev. Lett. 47, 1899–1902 (1981)
- [37] A.Fernández et.al."Electron Bernstein Wave heating for the TJ-II stellarator" 3th Workshop on Electron Cyclotron Resonance Heating and Electron Cyclotron Emission. Nizhny Novgorod. Russia. 17 – 20 May. 2004
- [38] T.H.Stix, "Waves in Plasmas" (Springer Verlag, New York 1992)
- [39] D.Gary Swanson "Plasma Waves" (Academic Press, Boston, 1989)
- [40] E.Mjøhus, J. Plasma Phys. 31, 7 (1984).
- [41] R.B.White, F.F.Chen "Amplification and Absorption of Electromagnetic Waves in Overdense Plasmas" Plasma Physics, Vol.16, pp.565-587. Pergamon Press 1974.
- [42] F.Chen: Introduction to Plasma Physics and Controlled Fusion, Vol. 1, Plasma Physics. Plenum Press 1984.
- [43] H.Igami, M.Uchida, H.Tanaka, T.Maekawa "Polarization adjustment of incident electromagnetic waves for optimal mode-conversion to electron Bernstein waves" Plasma Phys. controlled fusion 46 (2004) 261-275
- [44] A.K.Ram and S.D.Schultz, "Excitation, propagation, and damping of electron Bernstein waves in tokamaks" Phys.Plasmas Vol.7 Nr.10, p4084 (2000)
- [45] S.Nakajima and H. Abe „Particle Simulation Of The O-X-B Mode Conversion And Overdense Plasma Heating In The Electron Cyclotron Range Of Frequencies" Physics Letters A V.124 #4,5 1987
- [46] T.Maekawa, S.Tanaka, Y.Terumichi, Y.Hamada "Wave trajectory and Cyclotron Heating in Toroidal Plasmas" Phys. Review Letters. Vol.40, Nr.21, May 1978
- [47] M.Tereshchenko et al. "Development of 3D Gaussian Shaped Beam Tracing code for Plasma Heating by Bernstein Waves in TJ-II". Proceedings of the 30th EPS conference. St. Petersburg, Russia. June 2003.
- [48] F.Castejón et al. "Electron Bernstein Wave heating calculations for TJ-II plasmas". Proceedings of the 14<sup>th</sup> International Stellarator Workshop. Greifswald, Germany. September 2003.
-

- 
- [49] "High frequency plasma heating" Gorky 1983
- [50] Karl S.Kunz and Raymond J.Luebbers, The Finite Difference Time Domain Method for Electromagnetics, CRC Press, Boca Raton, FL, 1993.
- [51] A.Taflove and S. C. Hagness, Computational Electrodynamics: The Finite-Difference Time-Domain Method, 2nd ed., Artech House, Norwood, MA, 2000.
- [52] J.H.Irby, S.Horne I.H.Hutchinson and P.C. Stek "2D fullwave simulation of ordinary mode reflectometry" Plasma Phys. Control. Fusion 35 (1993) 601-618.
- [53] R.Veerasingam, R.B.Campbell,E.H. Klevans, R.T. McGrath "Ray tracing calculations of ECR absorption in plasma etching devices" Plasma Sourcess Sci. Technol. 3 (1994) 142-153
- [54] M.Sugawa "Electron Heating by Self-Interaction of Bernstein Waves" Journal of the Physical Society of Japan, Vol.61, Nr.6 pp.1848-1851 (June, 1992,)
- [55]. K.Rypdal et.al. "Microwave-plasma ina simple magnetized torus" Phys. Plasmas 4(5),1468 May1997.
- [56] Hirotaka Nakatsuka, et.al."Three-Dimensional Analysis of a Vacuum Window Connected to Waveguide" IEEE Transactions on Plasma Science, Vol.16, Nr.4 (August 1988)
- [57] C.A.Balanis "Antenna Theory Analysis and Design" 2<sup>nd</sup> edition Arizona State university 1997.
-

# Acknowledgments

I want to express my gratitude to my scientific supervisor Prof. Friedrich Wagner. I am much obliged for the opportunity to carry out my PhD studies in the Max-Planck Institute for Plasmas Physics in Greifswald, also for very helpful discussions and essential contributions to my work.

I also want to express a separate acknowledgement to Dr. Heinrich. P. Laqua who guided my work and made valuable contribution for its success.

I am thankful to the WEGA group with Dr. Matthias Otte as its head for help in performing the measurements and for fruitful discussions. I would like to thank Dr. Johann Lingertat who was the head of the WEGA group when I start my PhD in Greifswald. I also want to thank to Dr. Kinga Horvath whose PhD results were a good basis to start my work. Also, the technical support of Dieter Aßmus and Norbert Paschkowski is gratefully acknowledged. I enjoyed the friendly atmosphere in the WEGA group.

I also want to express my gratitude to Dr. Eberhard Holzhauer (University Stuttgart) for providing the full wave code to me, and for his pleasant and fruitful discussions.

I would also like to thank Prof. Friedrich Wagner, Dr. Heinrich. P. Laqua, Dr. Matthias Otte, Dr. George Warr, Dr. Francesco Volpe, Dr. Denis Eremin, Oliver Lischtschenko for proof-reading some of the chapters of this thesis.

I'd like to thank Prof. Tomas Klinger and other organizers of International Max Planck Research School for the unforgettable time I spent with other members of IMPRS.

I want to express profound gratitude to Prof. Eugene D. Volkov, Dr. Vladimir S. Voitsenja, Dr. Anatoly I. Skibenko, and other employees of NSC KIPT Institute of Plasma Physics (Ukraine, Kharkov) and Kharkov National University for the knowledge they gave me, and the support of my wish to carry out a PhD thesis work in the Max-Planck institute in Greifswald.

Finally, my thanks and gratitude goes to Anja Lochau, Anne Eggeling, Claudia Schoenian, and all members of administrative staff of IPP Greifswald for great support and the very friendly atmosphere.

---

Hiermit erkläre ich, daß diese Arbeit bisher von mir weder an der Mathematisch-Naturwissenschaftlichen Fakultät der Ernst-Moritz-Arndt-Universität Greifswald noch einer anderen wissenschaftlichen Einrichtung zum Zwecke der Promotion eingereicht wurde.

Ferner erkläre ich, daß ich diese Arbeit selbständig verfaßt und keine anderen als die darin angegebenen Hilfsmittel benutzt habe.

Greifswald, im Januar 2006

---

Yuriy Podoba

---